

AD-A166 317

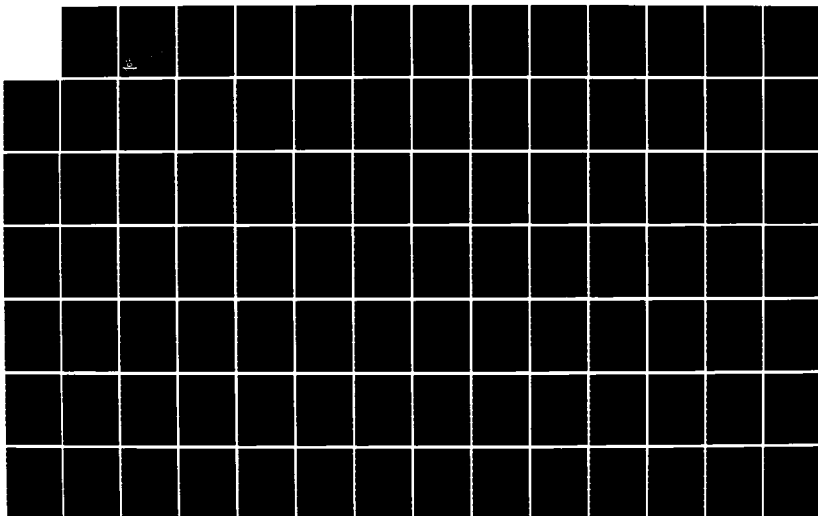
INHIBITING CORROSION CRACKING: CRACK TIP CHEMISTRY AND
PHYSICS(U) MICHIGAN STATE UNIV EAST LANSING DEPT OF
METALLURGY MECHANICS AND MATERIALS SCIENCE R SUMMITT
14 MAR 86 N00014-84-K-0419

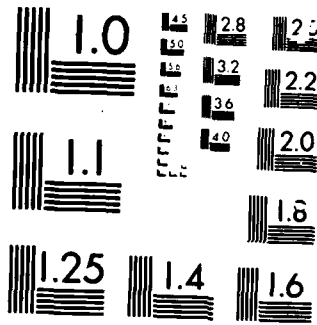
1/2

UNCLASSIFIED

F/G 11/6

NL





MICROCOPY RESOLUTION TEST CHART

AD-A166 317

INHIBITING CORROSION CRACKING:
CRACK TIP CHEMISTRY AND PHYSICS

Submitted to

OFFICE OF NAVAL RESEARCH

FINAL REPORT

Contract No. N 00014-K-0419

14 March 1986

Robert Summitt

Department of Metallurgy, Mechanics, and Materials Science

and

Division of Engineering Research

DTIC FILE COPY

DTIC
ELECTE
APR 04 1986
S D E



COLLEGE OF ENGINEERING

MICHIGAN STATE UNIVERSITY

EAST LANSING, MICHIGAN 48824

MSU IS AN AFFIRMATIVE ACTION/EQUAL OPPORTUNITY INSTITUTION

This document has been approved
for public release and sale its
distribution is unlimited.

REPORT DOCUMENTATION PAGE

1a. REPORT SECURITY CLASSIFICATION Unclassified			1b. RESTRICTIVE MARKINGS			
2a. SECURITY CLASSIFICATION AUTHORITY			3. DISTRIBUTION/AVAILABILITY OF REPORT Unlimited			
2b. DECLASSIFICATION/DOWNGRADING SCHEDULE						
4. PERFORMING ORGANIZATION REPORT NUMBER(S) None			5. MONITORING ORGANIZATION REPORT NUMBER(S)			
6a. NAME OF PERFORMING ORGANIZATION Metallurgy, Mechanics and Materials Science and Division of Engineering Research		6b. OFFICE SYMBOL (if applicable) 4B834	7a. NAME OF MONITORING ORGANIZATION Office of Naval Research Department of the Navy			
6c. ADDRESS (City, State, and ZIP Code) Michigan State Univeristy East Lansing, MI 48824			7b. ADDRESS (City, State, and ZIP Code) 800 North Quincy Street Arlington, VA 22217			
8a. NAME OF FUNDING/SPONSORING ORGANIZATION Office of Naval Research Department of the Navy		8b. OFFICE SYMBOL (if applicable) N00014	9. PROCUREMENT INSTRUMENT IDENTIFICATION NUMBER NR 036-173/04-20-84 (430)			
8c. ADDRESS (City, State, and ZIP Code) 800 North Quincy Street Arlington, VA 22217			10. SOURCE OF FUNDING NUMBERS			
			PROGRAM ELEMENT NO.	PROJECT NO.	TASK NO.	WORK UNIT ACCESSION NO.
11. TITLE (Include Security Classification) Inhibiting Corrosion Cracking: Crack Tip Chemistry and Physics						
12. PERSONAL AUTHOR(S) Robert Summitt						
13a. TYPE OF REPORT FINAL		13b. TIME COVERED FROM 84/4/1 TO 86/3/14		14. DATE OF REPORT (Year, Month, Day) 86 March 14		15. PAGE COUNT 125 + 10
16. SUPPLEMENTARY NOTATION						
17. COSATI CODES			18. SUBJECT TERMS (Continue on reverse if necessary and identify by block number)			
FIELD	GROUP	SUB-GROUP				
19. ABSTRACT (Continue on reverse if necessary and identify by block number) Experimental microtechniques are used to determine physical and chemical conditions at a corrosion crack tip while the bulk exterior environment is modified by the presence of corrosion accelerants or inhibitors. The chemistry of the nitrogen-system inhibitors is being explored systematically to identify accelerant/inhibitor characteristics which are effective in determining corrosion crack growth rates, thereby leading to practical inhibitor formulations.						
20. DISTRIBUTION/AVAILABILITY OF ABSTRACT <input checked="" type="checkbox"/> UNCLASSIFIED/UNLIMITED <input type="checkbox"/> SAME AS RPT <input type="checkbox"/> DTIC USERS				21. ABSTRACT SECURITY CLASSIFICATION		
22a. NAME OF RESPONSIBLE INDIVIDUAL			22b. TELEPHONE (Include Area Code)		22c. OFFICE SYMBOL	

Acknowledgments

This Final Report summarizes the research of several graduate and undergraduate students at Michigan State University:

- H. Omura, Ph.D., 1984
- F. Castellanos, M.S., 1985
- K. B. Lenz, M.S., 1985
- J. Meiner, B.S., 1984
- D. Schoener, B.S., 1985
- H. Kim, doctoral candidate (1986)
- J. Yeh, M.S. candidate (1986)
- E. Schaper, M.S. candidate (1986)
- V. Rao, M.S. candidate (1986)

The Office of Naval Research has funded this research through Dr. C. T. Lynch and Dr. A. J. Sedriks. Their support and interest in this program are gratefully acknowledged.

The patient and persistent efforts of Mrs. C. Gustavison, who prepared this manuscript, also are very much appreciated.

Accession For	
NTIS GRA&I	<input checked="" type="checkbox"/>
DTIC TAB	<input type="checkbox"/>
Unannounced	<input type="checkbox"/>
Justification	
By _____	
Distribution/	
Availability Codes	
Dist	Avail and/or Special
A-1	

Table of Contents

	<u>Page</u>
1. Introduction	1
2. Background	2
2.1. Inhibitors	4
2.2. The Oxyanions of Nitrogen	13
2.2.1. Hyponitrite	15
2.2.2. Nitroxylate and Nitrohydroxylate	17
2.2.3. Hydronitrite	18
2.2.4. Nitrite	19
2.2.5. Nitrate	20
2.2.6. Peroxynitrate	20
2.3. Inhibitors/Accelerants Used in this Program	22
2.3.1. Sodium hyponitrite preparation	23
2.3.2. Determining Aqueous Concentrations of Nitrogen Oxyanions	24
2.4. Microelectrodes in Stress Corrosion Cracking and Corrosion Fatigue	25
2.4.1. Review	25
2.4.2. Experimental	27
2.4.2.1. Microelectrode Puller	
2.4.2.2. Glass Capillaries	30

2.4.2.3. Results	30
2.5 Models of SCC, CF, Crevice Corrosion and Pitting	30
3. Experimental Results	33
3.1. Electrokinetics	33
3.1.1. Electrokinetic Appartus	33
3.1.2. Electrokinetic Results	33
3.1.2.1. Chloride Ion Concentration Effects	34
3.1.3.2. Inhibitor Effects	34
3.1.3.3. Stress Effects	54
3.1.3.4. Crack Electrochemistry	57
3.2. Stress/Strain Relations at a Corrosion Crack Tip	75
3.3. Alternate Immersion Testing	77
3.4. Corrosion Fatigue Inhibition	78
4. Discussion	93
4.1 Bare Surface Corrosion	93
4.2 Crack Electrochemistry	95
4.3 Extending Mathematical Models	100
5. Summary	113

References

List of Figures

	<u>Page</u>
1. Micropipette pulling machine.	29
2. Anodic polarization of 7075-T6 Al alloy in dilute sodium chloride solution.	35
3. Cathodic polarization of 7075-T6 Al alloy in 1 wt% NaCl solution.	36
4. Cathodic polarization of 7075-T6 Al alloy in 3 wt% NaCl solution.	37
5. Anodic polarization of 7075-T6 Al alloy in 1 wt% NaCl and nitrite/borax inhibitor.	38
6. Anodic polarization of 7075-T6 Al alloy in 1 wt% NaCl and NaSCN.	39
7. Anodic polarization of 7075-T6 Al alloy in 1 wt% NaCl and sodium acetate.	41
8. Anodic polarization of 7075-T6 Al alloy in 1 wt% NaCl and sodium oxalate.	42
9. Anodic polarization of 7075-T6 Al alloy in 1 wt% NaCl, nitrite/borax inhibitor, and surfactant.	45

10. Cathodic polarization of 7075-T6 Al alloy in sodium chloride and sodium nitrite. 46
11. Anodic polarization of 7075-T6 Al alloy in aqueous solutions of sodium nitrite. 48
12. Anodic polarization of 7075-T6 Al Alloy in aqueous sodium nitrite with sodium chloride. 49
13. Anodic polarization of 7075-T6 Al alloy in aqueous sodium nitrite with borax. 50
14. Anodic polarization of 7075-T6 Al alloy in aqueous sodium nitrite, borax, and sodium chloride. 51
15. Anodic polarization of 7075-T6 aluminum alloy in aqueous solutions of sodium nitrite, borax, and sodium chloride. 52
16. Anodic polarization of 7075-T6 aluminum alloy in aqueous multifunctional inhibitor and sodium chloride. 53
17. Linear polarization of 7075-T6 Al alloy in 1 wt% NaCl with sodium nitrite and surfactant. 55
18. Linear polarization of 7075-T6 Al alloy in 1 wt% NaCl and sodium nitrite. 56
19. Anodic polarization of 7075-T6 Al alloy in 1 wt% NaCl under stress. 58

20. Anodic polarization of 7075-T6 Al alloy in dilute NaCl solution. 59
21. Cathodic polarization of 7075-T6 Al alloy crevice in 1 wt% NaCl solution. 61
22. Cathodic polarization of 7075-T6 Al alloy crevice in 3 wt% NaCl solution. 62
23. Steady-state open-circuit potentials for bare and crevice 7075-T6 Al alloy in dilute NaCl with and without inhibitors. 63
24. Steady-state open-circuit potentials for bare and crevice 7075-T6 Al alloy in dilute NaCl solution. 65
25. Anodic polarization for bare and crevice 7075-T6 Al alloy in 1 wt% NaCl solution. 66
26. Anodic polarization of 7075-T6 Al alloy crevice in various configurations. 67
27. Steady-state open-circuit potential for bare and coupled crevice 7075-T6 Al alloy in 1 wt% NaCl solution. 70
28. Potential difference for bare and crevice 7075-T6 Al alloy under active state in 1 wt% NaCl solution. 71
29. Steady-state open-circuit potential of 7075-T6 Al alloy under stress in 1 wt% NaCl solution. 72

30. Steady-state open-circuit potential for bare and coupled crevice 7075-T6 Al alloy in 1 wt% NaCl. 74
31. Crack growth rate dependence of 7075-T6 Al alloy on stress intensity factor in NaCl solutions. 76
32. Electrohydraulic apparatus for corrosion fatigue. 88
33. Method for introducing accelerant/inhibitor solutions to crack tip. 90
34. Effect on crack growth rate of inhibitor introduced to a propagating fatigue crack. 91
35. Schematic crack representation. 92
36. Schematic polarization diagram. 103
37. Schematic polarization diagram. 104

List of Tables

	<u>Page</u>
1. The Oxyanions of Nitrogen	14
2. Oxidation Potential Data for Reduction of Nitrate Ion	21
3. Multifunctional Inhibitor Formulation	23
4. Inhibitors used in Alternate Immersion Tests	79
5. Alternate Immersion Test Results	80-87

1. Introduction

Aqueous metallic corrosion is a complex process involving a variety of individual steps in the overall mechanism for a given alloy. The problems of pitting corrosion, crevice corrosion, stress corrosion cracking (SCC), and corrosion fatigue (CF) are, to say the least, significantly more complex. If the discussion is extended further to include the action of substances which either accelerate or inhibit these processes, the complexity of the problems is increased further by orders of magnitude. The subject of the research program discussed in this Report is an experimental exploration of the relations between accelerant/inhibitor properties and the electrochemistry and electrokinetics of corrosion, SCC, and CF in aluminum alloys.

The Report is divided into the following sections:

(1) Background, a review of relevant theoretical and experimental research which sets the stage for the approach of this program. This background is concerned especially with the nature of environmental chemistry and mechanisms whereby the bulk environment can control corrosion processes at an active surface, particularly within a pit, crevice, or crack. Although the focus of this program is on aluminum alloys, it is necessary to include substantial material related to ferrous alloys so that the questions are delineated clearly.

(2) Experimental, a discussion of work performed in the course of this program. Subjects that have been explored include:

a) Electrokinetic studies of corrosion in various inhibitive and accelerant environments;

b) Systematic evaluation of inhibitor/accelerant substances and surfactants, via electrokinetic studies and alternate immersion screening tests.

c) Fatigue tests in the presence of accelerants and inhibitors, intended to develop capability for measuring stress/strain relations in the vicinity of a CF/SCC crack tip.

d) Fabrication and use of microelectrodes for measuring electrochemistry within an SCC crack, while external electrochemistry is controlled by a variety of accelerant/inhibitor chemistry and electropotential environments.

e) Systematic exploration of the chemistry of known inhibitive systems, specifically, the oxyanions of nitrogen, and the resultant effects on corrosion and SCC/CF.

(3) Discussion of partial results obtained to date.

2. Background

Stress corrosion cracking and corrosion fatigue have been the subject of numerous theoretical and experimental investigations. (1-3) The various results have suggested a number of models for the processes (4) as well as practical methods for preventing or controlling SCC and CF damage (3).

The actual mechanisms of corrosion cracking are related to the chemistry and physics prevailing at the crack tip, and it is well established that these conditions are different from those of the bulk environment. It also is well established that a variety of chemical substances (e.g., chloride ion) accelerate the crack propagation rate, whereas other substances (e.g., nitrite and borate ions) inhibit. Thus,

accelerants and inhibitors are effective via modification of the crack-tip chemistry. Electrochemical processes at the crack tip will generate or consume various chemical species, thereby establishing concentration and electrode-potential gradients between the crack tip and the external environment. These gradients in turn are the driving forces for mass transport between the crack tip and the bulk environment.

A variety of theoretical models have been proposed which relate the bulk-solution properties to conditions at the crack tip based upon potential and concentration gradients, thus are adaptable to micro-experimental measurements. There remain major questions, however, concerning the relations between the external environment (described by chemistry, applied load, and electrical potentials with respect to other electrodes) and electrochemical conditions within the crack, particularly at the crack tip. Although a variety of clever experiments have been devised in efforts to determine these relations experimentally, few definitive results have been obtained. A significant barrier to progress has been the obvious difficulties of performing measurements within the confines of a crack.

In this research program, the problem is attacked along two paths in an effort to perform "critical" experiments which can differentiate between various theoretical models and lead to more practical advances in the prediction and control of corrosion cracking:

a. Chemistry and physics near a crack tip. Advances in experimental microchemistry and microphysics have made it possible to measure solution chemistry (pH, ionic concentrations), corrosion kinetics (via potentiostatic and galvanostatic methods), as well as stress-strain relations in the metal over a range of a few micrometers at the crack tip. A variety of experiments have been performed with good results in this area.

b. Systematic variation of the external environmental chemistry via variation of the physico-chemical characteristics of corrosion accelerants and inhibitors. Several molecular and ionic properties of such substances are of interest with respect to their actions in SCC and CF, e.g., molecular/ionic size and geometry, mobility, ionic charge, conductivity, and oxidation state.

This program empirically compares the electrochemical environment within a stressed crack and the crack propagation rate with external physicochemical conditions controlled by accelerants/inhibitors. These accelerants/inhibitors are selected so as to explore systematically their physical chemistry. Currently, we are studying the nitrogen oxyanion system in conjunction with accelerants and surfactants, while repeating a variety of earlier results reported in the literature in order to clarify certain questions.

2.1 Inhibitors

The accelerating/inhibiting effects of various substances on bulk corrosion rates as well as the rates of SCC and CF have been widely studied. This Report is concerned specifically with the effects of such substances, specifically compounds of nitrogen and boron used together with surfactants, in the corrosion processes of aluminum alloys. The following discussion reviews the effects of such substances on corrosion processes in general and, specifically, aluminum alloys.

Accelerant/inhibitive actions of various substances have been summarized by Schrier (6). Of specific concern to this study are the oxyanions of nitrogen, related nitrogen compounds (amines, ammonia), and

oxyanions from nearby elements in the periodic table, especially boron.

Specific oxyanions of nitrogen include the nitrite ion, NO_2^- , and the nitrate ion, NO_3^- , both of which have been studied extensively. There are several other oxyanions in the system which are of considerable interest, but their study in corrosion requires more chemical sophistication than has been used with NO_2^- and NO_3^- . These oxyanions will be discussed in a later section.

Cohen (7) notes that inorganic anodic inhibitors usually are either oxidizing anions (e.g., nitrite or chromate) or buffering agents (e.g., borate or phosphate). Oxidizing anions are effective in the absence of oxygen, but the effective concentration is lower in the presence of oxygen. Nitrite reacts at a metal surface to form a protective oxide film, and reduction products extend as far as ammonia. Buffering agents require the presence of oxygen and must be used at higher (ca two orders of magnitude) concentration than nitrite. Cohen (8) earlier had found that weight loss decreased as both concentration of nitrite and oxygen increased. At intermediate concentrations, pitting was observed. During the reaction/exposure of nitrite solution to the specimen, the nitrite ion concentration was found to decrease.

Cohen suggests that a surface film is formed by adsorption of nitrite on the metal surface, followed by a reaction to form oxide and ammonia. The same adsorption-reaction mechanism was proposed for other oxidizing inhibitors, e.g., chromate and molybdate. Although nonoxidizing inhibitors, require the presence of oxygen, in the presence of oxygen, a much higher concentration of nonoxidizing oxyanion is required to inhibit corrosion.

Rozenfeld (9, 10) has reviewed the effects of nitrite, nitrate, and other simple nitrogen-containing compounds, in both neutral aqueous solutions and in the presence of accelerants, specifically chloride and sulfate ions. The inhibiting properties of sodium nitrite depend on the concentration of accelerant ions in the electrolyte. In solutions containing sodium chloride and sodium sulfate, sodium nitrite accelerates corrosion up to ca. 0.08 g/l concentration, but, at higher concentrations, it exerts a strongly inhibitive effect, having maximum effect at 0.2 g/l concentration, (2 wt%). Rozenfeld suggests that sodium nitrite diverts a larger part of the surface from the anodic reaction and hence shifts the potential more strongly toward positive values than other inhibitors. The corrosion-intensifying mechanism involving low concentrations of sodium nitrite is the same as observed for other anodic inhibitors. In the absence of accelerant ions (distilled water), the protective concentration of sodium nitrite is between 10^{-5} and 10^{-4} mol/l⁻⁴ or ca 6.9×10^{-4} wt %.

When accelerant ions are present, the logarithm of the protective concentrations of sodium nitrite is linear with respect to the concentration of accelerant ions. The protective properties of nitrite are suppressed most strongly by sulfate ions and less strongly by nitrate ions. Therefore, for the same concentration of the accelerant ion, a higher sodium-nitrite concentration is needed in the presence of sulfate than in the presence of nitrate. To suppress corrosion in the presence of chloride, a lower sodium nitrite concentration is needed than in the presence of sulfate. As the concentration of accelerant ions increases, the difference between the effects of sulfate and chloride decreases, while the difference between chloride and nitrate remains. If high concentrations of the ions are excluded, then, in terms of aggressiveness, accelerants are ranked sulfate > chloride > nitrate.

In the presence of both accelerant and inhibitive ions, the passivating ion is adsorbed preferentially. Thus, it is harder for the nitrite ion to dislodge already adsorbed chloride ions from the electrode surface than not to allow it to be adsorbed. When various aggressive ions, e.g. chlorides and sulfates, are in the electrolyte, protection is achieved at a sodium nitrite concentration that is generally higher than the total concentration of accelerant ions. Corrosion occurs when the ratio of inhibitor concentration to total accelerant-ion concentration is less than one.

Sodium nitrite also is more effective in suppressing the accelerant properties of chlorides than are benzoate and chromate. In the presence of sulfates, nitrite is about as effective as chromate. With respect to nitrate ions the effectiveness of the different inhibitors decreases in the following order: chromate > benzoate > nitrite. Other compounds containing the NO_2 group and used as corrosion inhibitors include dicyclohexylamine nitrite (DAN) and salts of nitrobenzoic acids (nitrobenzoates). Also according to Rozenfeld and Marshakov (11), that concentration of inhibitors required to inhibit crevice corrosion is much higher than for general corrosion.

Oxyanions of various elements (e.g., chromium, molybdenum) are corrosion inhibitors for ferrous alloys in neutral aqueous solutions; acidified, they become cathodic depolarizers as well as influence the anodic ionization of iron, as discussed by Mikhailovskii, Popova, and Sokolova (12). Inhibiting properties are attributed either to a capacity to "repair" the oxide film formed on the metal in an electrolyte, or to adsorption of the oxyanion, resulting in a change in structure of the metal-electrolyte boundary. The influence of oxidizing agents usually is attributed to their

enhanced adsorption capacity which favors formation of surface complexes which retard the anodic ionization of the metal.

Marshall (13) found that a combination of nitrite with N, N-di-(phosphonomethyl) methylamine was an effective inhibitor system for ferrous alloys, comparable with nitrite alone, but it formed a passive film less susceptible to pitting. Ledovskikh (14) also has reported that combinations of NaNO_2 with various organic amines inhibit the corrosion of steel in 0.1 wt% NaCl, and finds further that this protective effect correlates well with physicochemical parameters of the amines (e.g., electron density at the nitrogen atom, ionization constant, and the Hammett and Taft constants of the organic radical).

McCafferty (15) classes inhibitors as (a) adsorption (chemisorption), (b) film-forming/passivating, and (c) precipitation. Crevice corrosion of iron accelerated by chloride and inhibited by chromate has been discussed further by McCafferty (16), finding that the process can be inhibited successfully at chloride concentrations up to 0.6 m/l (3.5 wt.%). The logarithms of each ion's activities are linearly related at the minimum chromate activity necessary to inhibit crevice corrosion. McCafferty explained this on the basis of competitive adsorption between the aggressive and inhibitive ions, each of which adsorbs according to a Temkin isotherm. Steady-state electrode potentials of crevice-corroding iron were found to be -620 to -660 mV vs. Ag/AgCl reference electrode, and independent of bulk solution composition.

The steps by which aggressive ions act on Al have been suggested by Samuels, Sotoudeh, and Foley (17) to be:

- 1) Adsorption of Cl^- on Al_2O_3 surface;
- 2) complexing of Al^{+3} in the oxide lattice with the halide ion to form soluble AlCl_4^- ;
- 3) diffusion in solution of AlCl_4^- , thus thinning the oxide layer; and
- 4) when Al_2O_3 has been removed, the Al reacts directly with the electrolyte.

Inhibitors may be active in either of the first two steps:

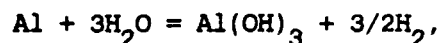
- competing for adsorption sites, hence retarding formation of soluble species;
- competing the reaction in $\text{Al}^{+3} + 4\text{Cl}^- = \text{AlCl}_4^-$ to prevent its

formation; hence the competing ion must form an insoluble complex.

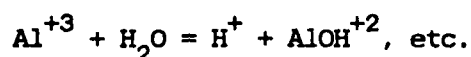
Samuels, Sotoudeh, and Foley also tested a variety of inhibitors, including chromate, and nitrate, and found that nitrate was effective in high concentrations. Certain concentrations, however, as well as certain $\text{Cl}^-/\text{NO}_3^-$ ratios, accelerate corrosion. Sulfate inhibits aluminum corrosion, but not as effectively as chromate.

Aqueous corrosion studies of mild steel by Robitaille (18) show that the inhibitive effects of sodium molybdate and sodium nitrite (ratio 30/20), are significantly larger than for either inhibitor alone. Surfactant additions (1-hydroxyethylidene-1, 1-diphosphonic acid, or 2-mercaptobenzothiazole) resulted in only minor effects.

From SCC studies Le, Brown, and Foley (19) showed that the nitrate ion is reduced by AA 7075 to ammonia. Foley and Nguyen (20) have written the overall reaction of Al with H_2O as



and the process involves:



The formation of an uncharged, stable, basic salt in a deep energy valley will prevent the reaction from progressing along the reaction coordinate. In the case of Cl^- as well as $SO_4^{=}$ (and possibly chromates and other oxyanions), initial formation of the complex species is rapid. Sulfates (and other inhibitive oxyanions) produced lie at a low energy level resisting forward movement along the reaction coordinate. Thus, in all corrosion reactions such as pitting and stress corrosion, chloride is aggressive, but $SO_4^{=}$ is not. They have analyzed these reactions with respect to free energy and probable reaction coordinates, as well as reactions involving sulfate ion.

Berdzenishvili, Strekalov, and Mikhailovskii (21) have studied the initial stages of aluminum corrosion in acidified sulfate solutions containing the oxyanions of tungsten, chromium, molybdenum, vanadium, and manganese. Corrosion inhibition was explained by the formation on the aluminum surface of a film of oxides of the foreign metals, as well as by the inhibiting role of hydroxyl ions in the near-surface layer of the electrolyte formed during cathodic reduction of the oxyanion. Thus, the

processes clearly implicated in the mechanism are: oxidation state of the central atom in the oxyanion; physical chemistry of the reduction reaction in the surface layer; and adsorption of the reductant on the surface.

Stolz and Pelloux (22) have performed aqueous fatigue tests of 7075 aluminum with sodium chloride as accelerant and sodium nitrate as inhibitor, as well as in dry air and dry argon. Highest crack growth rates vs. stress-intensity-factor-range curves were observed for aqueous sodium chloride (0.2 molal), and lowest for dry argon. Sodium nitrite solutions (1.7 molal) reduced crack growth curves to values comparable with those in dry air. SEM studies show that environment has a strong effect on microplastic behavior at the tip of a fatigue crack. Stolz and Pelloux suggest that nitrate ion competes with chloride for surface sites; it does not cause metal dissolution itself, nitrate thus acts to protect a freshly exposed surface from attack.

Lynch and co-workers (23, 24-27) have conducted a number of studies aimed at developing practical inhibitor formulations; others have been motivated (28, 29) to follow similar lines of investigation. Parrish Chen, and Verink (28) demonstrated that oxidizing inhibitors (hydrazine, sodium dichromate) are effective in increasing $K_{I_{SCC}}$. Seeking more effective inhibitors, Verink and Das (29) evaluated more than 200 potential formulations for inhibiting corrosion fatigue. Experiments included immersion, linear polarization, and corrosion crack growth-rate tests, and their results showed that piperidine, piperazine, and a proprietary polyfunctional formulation (Nalco 39L) significantly reduced corrosion cracking. Using similar methods, Lynch, Vahldiek, Bhansali, and Summitt (26) showed that non-toxic formulations including sodium nitrite and borax also are effective.

Extending the search for practical but nontoxic inhibitive substances, Khobaib, Quackenbush, and Lynch (24, 25) evaluated a variety of formulations with surfactant additions. Similar experiments (i.e., immersion, polarization, crack-growth kinetics) were performed, some in specially constructed environmental chambers. The results showed that combinations of borax, sodium nitrite and surfactants inhibit both general corrosion and corrosion fatigue in high-strength aluminum alloys. Although piperazine was found to inhibit corrosion fatigue, it did not affect general corrosion rates. In a further study, Khobaib (27) evaluated more than 200 formulations of organic and inorganic compounds for their inhibiting efficacy in the presence of urine for use as airplane bilge inhibitors. The most effective combinations again involved borax, sodium nitrite and a variety of surfactants. These effective inhibitor formulations were developed by systematic exploration of the compositions suggested by Green and Boies (30).

In summary, the very extensive accelerant/inhibitor suggests that a variety (perhaps a "spectrum") of physicochemical properties of such substances may be involved in corrosion processes. Many published studies contains hints as to which properties may be critical, e.g., ionic charge, size, mobility, ionization state, adsorption, etc., but none point to this conclusion clearly, i.e., systematic exploration of accelerant/inhibitor chemistry offers the best opportunity for elucidating the crucial properties in corrosion. The oxyanions of nitrogen, amines, organic nitro compounds, and other substances, in short the chemistry of nitrogen, comprise an excellent system for this study. Since the nitrogen oxyanions with ammonia span the entire nitrogen oxidation state (+5 to -3), we have begun our research here.

2.2 The Oxyanions of Nitrogen (31)

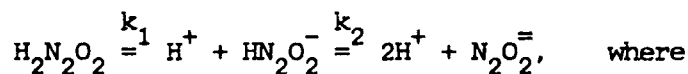
The oxyanions of nitrogen are listed in Table 1 together with the apparent oxidation state of nitrogen and the most likely electronic structure. Although all of them can form free acids, only nitric acid can be considered stable in aqueous solution or as the pure acid; all the rest decompose with varying degrees of violence. All can be prepared as relatively stable salts, particularly the sodium salt, although the preparations or the salts themselves are somewhat hazardous. The oxidation reduction and inhibitive properties of these ions are related their instability characteristics.

Table 1. The Oxyanions of Nitrogen (31)

<u>Formula</u>	<u>Name</u>	Apparent <u>Oxidation</u> <u>State of N</u>	Probable <u>Structure</u>
$N_2O_2^{-2}$	hyponitrite	+1	$\begin{array}{c} \ddot{O} \quad \ddot{N} \quad \ddot{N} \quad \ddot{O} \\ \vdots \quad \vdots \quad \vdots \quad \vdots \end{array}$
$N_2O_3^{-2}$	nitrohydroxylamate	+2	$\begin{array}{c} \ddot{O} \quad \ddot{N} \quad \ddot{N} \quad \ddot{O} \\ \vdots \quad \vdots \quad \vdots \quad \vdots \\ \quad \quad \quad \ddot{O} \\ \quad \quad \quad \vdots \end{array}$
NO_2^{-2}	hydronitrite	+2	$\begin{array}{c} \ddot{O} \quad \ddot{N} \quad \ddot{O} \\ \vdots \quad \vdots \quad \vdots \end{array}$
NO_1^{-1}	nitrite	+3	$\begin{array}{c} \ddot{O} \quad \ddot{N} \quad \ddot{O} \\ \vdots \quad \vdots \quad \vdots \end{array}$
NO_3^{-1}	nitrate	+5	$\begin{array}{c} \ddot{O} \quad \ddot{N} \quad \ddot{O} \\ \vdots \quad \vdots \quad \vdots \\ \quad \quad \quad \ddot{O} \\ \quad \quad \quad \vdots \end{array}$
NO_4^{-1}	peroxynitrate	+5	$\begin{array}{c} \ddot{O} \quad \ddot{O} \quad \ddot{N} \quad \ddot{O} \\ \vdots \quad \vdots \quad \vdots \quad \vdots \\ \quad \quad \quad \ddot{O} \\ \quad \quad \quad \vdots \end{array}$

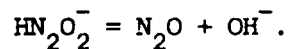
2.2.1. Hyponitrite

Free hyponitrous acid, $H_2N_2O_4$, can be prepared as white deliquescent plates; however, it is explosively unstable. Aqueous solutions of the acid are relatively stable: At pH 1-3 and $25^\circ C$, the acid has a half-life of ca 16 days, but at pH 4-14, it is quite stable. The acid ionizes as a weak dibasic acid,



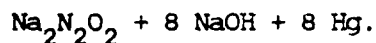
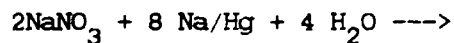
$$k_1 = 9 \times 10^{-8} \text{ and } K_2 = 1 \times 10^{-11}.$$

In higher pH solution, the hydrogen hyponitrite ion is unstable,

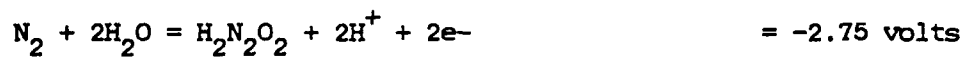
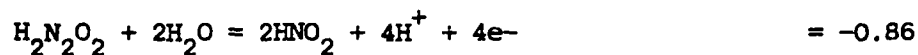


Thus, the characteristics of the hyponitrite ion related to corrosion can be examined readily, particularly in mild acid to alkaline solutions.

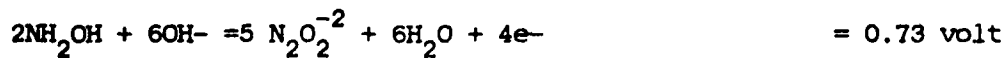
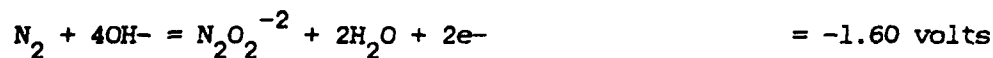
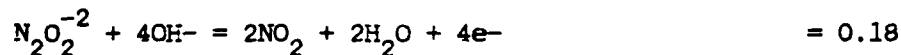
The metal salt are prepared generally by reduction of the nitrate ion, commonly by sodium amalgam,



Hyponitrites possess both reducing and oxidizing properties as indicated by the couples



in acidic solution, and the couples



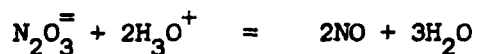
in alkaline solution. However, the reducing properties predominate. Strong oxidizing agents will convert hyponitrites to nitrates.

2.2.2. Nitroxylate and Nitrohydroxylate

Salts of two acids having compositions expressed by the formula $\text{NO}_n\text{H}_2\text{O}$ have been prepared. The first of these, nitrosylic acid, H_2NO_2 , also called hydronitrous acid, is known only in the form of its sodium salt, Na_2NO_2 . This salt is obtained either by the electrolytic reduction of solutions of sodium nitrite in liquid ammonia, or by the addition of sodium nitrate to solutions of sodium in liquid ammonia until the blue color disappears; yellowish sodium nitroxylate then precipitates from the liquid ammonia solution. On contact with water or moist air, sodium nitroxylate reacts explosively with the evolution of hydrogen. This ion, then can not be studied with respect to aqueous corrosion.

Nitrohydroxylamic acid, $\text{H}_2\text{N}_2\text{O}_3$, also is not known as the free acid, although a number of metal nitrohydroxylamates have been prepared. If a concentrated absolute ethanol solution of sodium ethylate is mixed with a saturated alcohol solution of hydroxylammonium chloride in alcohol, sodium chloride precipitates and can be filtered off, ethyl nitrate then is added to the filtrate, and a solution of sodium nitrohydroxylamate is obtained. When this solution is cooled, solid $\text{Na}_2\text{N}_2\text{O}_3$ separates as a fine powder. The salt dissolves in water to give alkaline solutions, presumably because HN_2O_3^- and $\text{H}_2\text{N}_2\text{O}_3$ are weak acids and the $\text{N}_2\text{O}_3^=$ ion undergoes hydrolysis. If

solutions containing N_2O_3^- ions are acidified immediate decomposition takes place:



When heated, aqueous sodium nitrohydroxylamate decomposes to yield nitrogen (I) oxide and the nitrite ion. Solutions of nitrohydroxylamates are readily oxidized even by atmospheric oxygen. Thus, the nitrohydroxylamate ion can be studied in alkaline solutions, but with considerable difficulty.

A compound apparently identical to the nitrosohydroxylamate is sodium alpha-oxyhyponitrite, $\text{Na}_2\text{N}_2\text{O}_3$, which has been prepared by the action of hydroxylamine and sodium ethoxide in alcoholic solution of ethylnitrate. An allotropic beta form of the same compound results from the oxidation of sodium hyponitrite by liquid N_2O_4 . The hyponitrite and alpha-oxyhyponitrite may be distinguished by the differences in their ultraviolet absorption spectrum.

2.2.3. Hydronitrite (32)

The sodium salt of this acid is prepared in a manner similar to that for sodium hydronitrate, except sodium nitrite is used instead of sodium nitrate. A solution of sodium nitrite in liquid ammonia is added to a liquid ammonia solution of sodium until the blue color disappears. An intense yellow flocculant precipitate forms, having the formula Na_2NO_2 . The alkaline-hydronitrite is extraordinarily reactive; air, moisture, and carbon

dioxide react violently with it, and even a small mass often produces a powerful explosion. Clearly the hydronitrite can not be studied.

Nitric amide, NO_2NH_2 , has the same formula as hydronitrous acid, but a different structure. It also is unstable (33), however, and would not be of immediate interest.

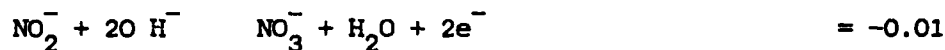
2.2.4. Nitrite

Sodium nitrite is a readily available laboratory reagent. Nitrous acid and the nitrites are most commonly employed as oxidizing agents, although strong oxidants (e.g., electric current, MnO_2 , and Cl_2) convert nitrous acid to nitric acid, and even weak oxidants (e.g., O_2) convert nitrous to nitric acid in alkaline solution. Important couples describing these behaviors are



in acidic solutions, and





in alkaline solutions. The greater oxidizing strength in acidic solutions is apparent. The complete behavior of nitrous acid in the presence of reducing agents is not clear in terms of these couples alone, since other reduction products may result, depending upon the reducing agent employed, pH, and temperature.

2.2.5. Nitrate

Sodium nitrate is readily available, and its properties are well known (31). The data in Table 2 show the wide variety of reduction reactions available and their relations to other nitrogen oxyanions and compounds. Also shown are stepwise reduction processes of nitrogen (V) to nitrogen (III). The effect of acid media on the oxidizing power of nitrate is clearly evident.

2.2.6. Peroxynitrate

Peroxynitric acid is formed from the reaction of hydrogen peroxide with dinitrogen pentoxide,

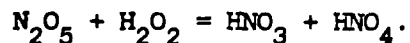


Table 2. OXIDATION POTENTIAL DATA FOR REDUCTION OF NITRATE ION (31)

Acidic Solutions		Alkaline Solutions	
$N_2O_4 + 2H_2O$	$\rightleftharpoons 2NO_3^- + 4H^+ + 2e^-$	$N_2O_4 + 4OH^-$	$\rightleftharpoons 2NO_3^- + 2H_2O + 2e^-$
$HNO_3 + H_2O$	$\rightleftharpoons NO_3^- + 3H^+ + 2e^-$	$NO_3^- + 2OH^-$	$\rightleftharpoons NO_3^- + H_2O + 2e^-$
$NO + 2H_2O$	$\rightleftharpoons NO_3^- + 4H^+ + 3e^-$	$NO + 4OH^-$	$\rightleftharpoons NO_3^- + 2H_2O + 3e^-$
$N_2O + 5H_2O$	$\rightleftharpoons 2NO_3^- + 10H^+ + 8e^-$	$N_2O + 10OH^-$	$\rightleftharpoons 2NO_3^- + 5H_2O + 8e^-$
$H_2N_2O_2 + 4H_2O$	$\rightleftharpoons 2NO_3^- + 10H^+ + 8e^-$	$N_2O_4^{2-} + 8OH^-$	$\rightleftharpoons 2NO_3^- + 4H_2O + 8e^-$
$\frac{1}{2}N_2 + 3H_2O$	$\rightleftharpoons NO_3^- + 6H^+ + 5e^-$	$\frac{1}{2}N_2 + 6OH^-$	$\rightleftharpoons NO_3^- + 3H_2O + 5e^-$
$NH_3OH^+ + 2H_2O$	$\rightleftharpoons NO_3^- + 8H^+ + 6e^-$	$NH_3OH + 7OH^-$	$\rightleftharpoons NO_3^- + 5H_2O + 6e^-$
$N_2H_5^+ + 6H_2O$	$\rightleftharpoons 2NO_3^- + 17H^+ + 14e^-$	$N_2H_5 + 16OH^-$	$\rightleftharpoons 2NO_3^- + 10H_2O + 14e^-$
$NH_4^+ + 3H_2O$	$\rightleftharpoons NO_3^- + 10H^+ + 8e^-$	$NH_3 + 9OH^-$	$\rightleftharpoons NO_3^- + 6H_2O + 8e^-$
$NH_4^+ \rightleftharpoons N_2H_4^+ \rightleftharpoons NH_3OH^+ \rightleftharpoons N_2$	$E_{1,11}^{\circ} = -0.81 \text{ volt}$	$NH_3 \rightleftharpoons N_2H_4 \rightleftharpoons NH_3OH \rightleftharpoons N_2$	$E_{1,11}^{\circ} = 0.85 \text{ volt}$
	-1.24		-0.10
	-1.46		-0.74
	1.87		3.04
	-1.77		-0.94
	-1.59		-0.76
	-2.75		-1.60
	-0.60		-0.10
$NO_3^- \rightleftharpoons N_2O_4 \rightleftharpoons HNO_2 \rightleftharpoons NO$	-0.81	$NO_3^- \rightleftharpoons N_2O_4 \rightleftharpoons HNO_2 \rightleftharpoons NO$	0.85
	-1.07		-0.88
	-0.99		0.46

The sodium salt can be prepared. The oxidation state of nitrogen in the peroxy nitrate ion is +5, the same as in the nitrate ion, and the ion configuration differs only in the presence of an extra oxygen atom (Table 1). Preparation of sodium peroxy nitrate is considerably more hazardous than for any other salts, although two of the other salts themselves are more hazardous to handle.

As a result of these considerations, the first nitrogen oxyanion that is under study in this program is hyponitrite. Simultaneously, the characteristics of nitrite, nitrate, and ammonia, alone and in combination with other inhibitors (e.g., chloride), and surfactants are being examined.

2.3. Inhibitors/Accelerants used in this Program.

As noted, a variety of inhibitor/accelerant and surfactant substances are under study. These include (a) ordinary reagent-grade chemicals, e.g., NaCl, NaNO_2 , NaNO_3 , and NH_4OH , (b) commercial and reagent-grade surfactants, (c) the Lynch formulation mentioned in Section 2.1, and (d) other compounds of nitrogen, specifically sodium hyponitrite. The Lynch formulation [item (c)] is listed in Table 3. Preparation of sodium hyponitrite is described briefly in Section 2.3.1. Procedures for determining aqueous concentrations of the most significant ions, before and after corrosion tests, are described in Section 2.3.2. Section 2.3.3. discusses briefly our initial evaluations of various surfactants.

Table 3. Multifunctional Inhibitor Formulation (27)

		<u>Formula Weight</u>	<u>Recommended aqueous wt %</u>
Borax	$\text{Na}_2\text{B}_4\text{O}_7 \cdot 10\text{H}_2\text{O}$	381.37	0.35
Sodium Nitrate	NaNO_3	84.80	0.1
Sodium Nitrite	NaNO_2	69.00	0.05
Sodium Metasilicate Pentahydrate	$\text{Na}_2\text{SiO}_3 \cdot 5\text{H}_2\text{O}$	212.74	0.01
Sodium Hexameta Phosphate	$(\text{NaPO}_3)_x \cdot \text{Na}_2\text{O}$		0.002
MBT, Mercapto- benzothiazole		167.25	0.001
		Total	0.513 wt%

2.3.1. Sodium Hyponitrite Preparation.

Sodium hyponitrite was prepared by aqueous reduction of sodium nitrate with sodium amalgam. Sodium amalgam (ca. 2 wt%) was prepared by adding liquid mercury to warmed sodium metal under a nitrogen atmosphere (34), then stored in a nitrogen-filled desiccator. Reduction of ice-chilled 4-molar

aqueous sodium nitrate to produce sodium hyponitrite was achieved by adding sodium amalgam to the solution under nitrogen (33). Crystalline $\text{Na}_2\text{N}_2\text{O}_2 \cdot 9\text{H}_2\text{O}$ precipitates when the filtrate is placed in a vacuum desiccator over sulfuric acid. The filtered precipitate is washed with ethanol to remove NaOH, then stored in a desiccator.

2.3.2 Determining Aqueous Concentrations of Nitrogen Oxyanions.

The accelerant/inhibitive effects of the various nitrogen oxyanions as well as anticipated decomposition of some ions will result in mixed solutions of various anions. It is essential that these solutions be analyzed before, during, and after corrosion tests. Colorimetric analytical methods are readily available (35), and spectrophotometric methods can be used to determine hyponitrite and alpha-oxyhyponitrite in the presence of nitrite and nitrate (36), and nitrite and nitrate (37, 38).

The MSU corrosion laboratory now is fully equipped for chemical, colorimetric and spectrophotometric analysis of these solutions. A Bausch and Lomb Spectronic 20 is used for colorimetric determinations. For spectrophotometric measurements, the laboratory includes a Beckman Model DB-GT Ultraviolet-visible-near infrared spectrophotometer. This is a single-beam/double-beam, ratio-indicating or recording instrument which can make rapid transmittance and absorbance measurements in the 190 to 700 nm wavelength region. Quantitative and qualitative analyses of oxyanions of nitrogen and other components of the electrochemical system under study are obtainable with high resolution. This spectrophotometer also is equipped with a Beckman Reflectance Accessory, which can convert the instrument to a spectroreflectometer for surface studies.

2.4 Microelectrodes in Stress Corrosion Cracking and Corrosion Fatigue

2.4.1. Review

Because of the obvious experimental difficulties, measurements of electrode potentials, pH, and ion concentrations within a real crack have been quite limited. Smith, Peterson, and Brown (39) used antimony/antimonous oxide ($\text{Sb/Sb}_2\text{O}_3$) and silver/silver chloride (Ag/AgCl) electrodes, each of 1/16 inch diameter, and a similar size commercial glass electrode to measure electrode potential and pH at the tip of an advancing crack. The $\text{Sb/Sb}_2\text{O}_3$ and Ag/AgCl electrodes, combined as a single probe, were too large to insert into the crack. Instead, a small scrap of absorbent lens tissue was placed against the outside surface of the crack tip, and against this were placed the electrochemical probes. Electrolyte was supplied by a reservoir on the opposite face of the specimen, and leak-through was prevented by a cemented Mylar film on the probe side. Their results showed that the electrochemistry at the crack tip is favorable for hydrogen reduction.

Ratyck, Dmytrakh, Pusyak, and Kurov (40) determined pH and electrode potential at a crack tip in steel by boring capillary holes in specimens in the path of the crack's growth and perpendicular to its front. In this hole was inserted the electrolytic capillary through which properties of the electrolyte at the crack tip could be sampled. A flow-through system was used. Again, microelectrodes were not inserted into the crack, but electrolyte flowing from it was analyzed.

Most experimental efforts to determine crack tip (or crevice tip) conditions have centered on the artificial cell, or the occluded cell. A

wide variety of such studies have been published, and a detailed review here would be superfluous; reviews already are in print, two of which summarize the situations in 1963 (41) and 1981 (42).

Artificial cracks and crevices may yield interesting results, but such results at best can be only a guide for developing experiments for measuring the actual electrochemical conditions at the crack tip, or for devising experiments of a different nature.

True microelectrodes, i.e., of microscopic dimensions, offer the possibility of actual insertion of probes into a growing crack. Frank and Fuortes (43) describe the fabrication and use of such microelectrodes from pipettes of redrawn Corning Code 7740 glass tubing. The tips of their micropipettes were less than 0.5 μ m diameter and ca seven mm in length. Dynamic electrical activity (potential) was measured within spinal neural cells with such electrodes. Rector, et. al (44) used similar, but slightly larger electrodes made of Corning 015 pH-sensitive capillary glass tubing to measure the pH in rat renal tubules. In addition Vieira and Malnic (45) have used antimony microelectrodes to measure in situ pH in rat renal tubules. These microelectrodes were fabricated using the same general techniques and equipment as are used for making glass microelectrodes, but are somewhat more rugged. Carter (46) provides detailed procedures for preparing glass microelectrodes which incorporate a reference electrode in the same structure. Pucacco and Carter (47) describe more difficult methods for fabricating both single and double electrodes from non-sensitive glass micropipettes with a membrane of sensitive glass covering the tips. Such electrodes have the advantage of having smaller surface-active area. Thomas (48) discusses in extensive detail materials, equipment, and procedures for producing, testing, and using not only pH and ion-sensitive glass

microelectrodes, but also a variety of others for chloride, etc. such as the Ag/AgCl microelectrodes.

Somewhat larger, more rugged pH and ion-sensitive "micro" electrodes are commercially available (W-P Instruments, Inc., P. O. Box 3110, New Haven, Conn., 06515, and Microelectrodes, Inc., Londonderry, NH 03053). A full line of materials and handling apparatus is offered (WPI) for laboratory-fabricated electrodes.

An interesting and novel development in this field has been the solid-state device fabrication methods to prepare chemically-sensitive membranes by I. Lauks of the University of Pennsylvania and co-workers (49-51). The most interesting of these has been pH sensitive sputtered iridium oxide film. These pH electrodes have been used in a wide variety of environments hostile to glass electrodes, and have been used to measure pH within the human mouth with better performance than glass electrodes (52). In principle, this electrode can be of near vanishing size, limited only by microcircuit fabrication technology and the necessary provision for external electrical connections. Although experienced faculty, trained personnel, and facilities are available at MSU for fabricating such devices, our efforts to date have centered on the fabrication and use of more traditional glass and metal/metal oxide microelectrodes.

2.4.2. Experimental

A pilot program has been developed to construct equipment for fabricating electrodes having tip diameters less than 100 μ m, and then use them in initial experiments to determine the conditions within a crack. Experimental measurement of conditions inside a crevice is difficult because

of the obvious problem of geometry. Although it is generally conceded that chemistry within a corrosion crack differs from that of the bulk solution, convincing experimental evidence is not available, despite numerous efforts to obtain such data. We describe here our results with the silver-silver chloride microelectrode and its method of production.

2.4.2.1. Microelectrode Puller

A vertical micropipette puller similar to Figure 1 was constructed. The vertical back plate is 33 cm high, 9 cm, wide and 0.6 cm thick. The upper clamp for holding the glass capillary is mounted at the top and, the lower clamp is on the upper cross piece of the slide. The total free movement of the slide is 6.5 cm. The holes for the tubing clamps are 8 mm in diameter. A glass tubing about 1 mm in diameter is held by nylon screws fixed in the 8 mm holes. Kanthal-A steel wire heater coils are mounted on a block of insulating material which plugs into sockets in the back plate. Power for the heater is supplied by a Variac auto transformer.

Three major factors affect the shape of the micropipettes. These are, in the order of importance:

1. Temperature, shape and size of the heater element;
2. The kind, diameter and wall thickness of glass tubing used;
3. The strength and variation of pull.

Temperature is the most important factor affecting the shape of glass pipette. The hotter and longer the heater coil, the longer are the micropipettes produced.

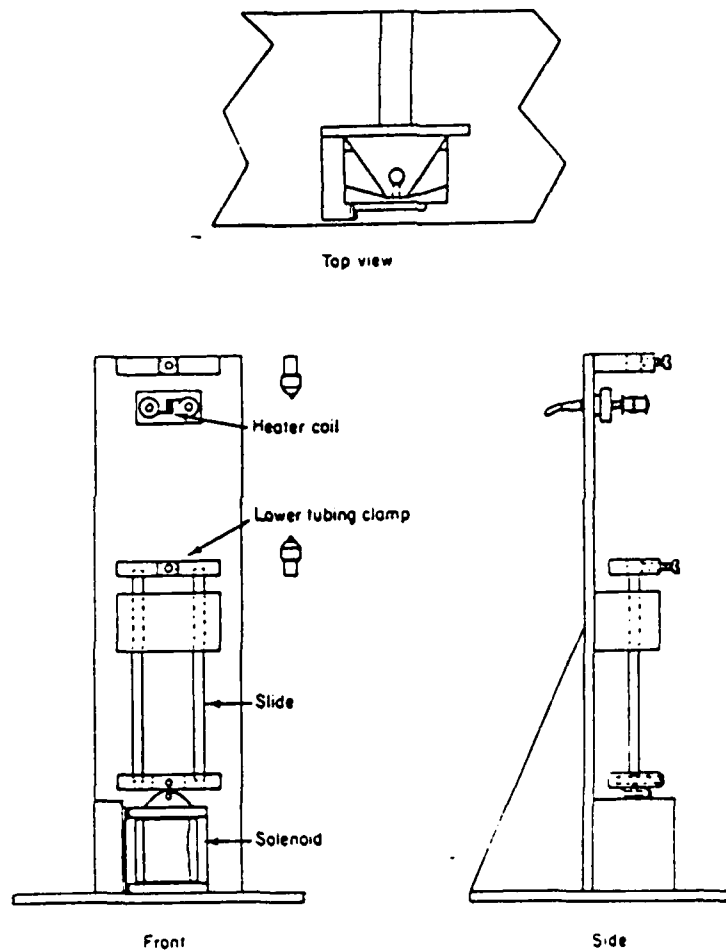


FIGURE 1. VERTICAL MICROPIPETTE PULLER.

2.4.2.2. Glass Capillaries

The micropipettes were filled by a gently boiling for 30 minutes in methanol and kept for 30 minutes at room temperature. They were then placed in distilled water for 7 hours at room temperature. The distilled water in the capillaries then was replaced by 3 M KCl by immersing them in 3 M KCl solution for 10 days at room temperature.

Fine silver-silver chloride wires then were introduced into the micropipettes. The method of making fine silver-silver chloride wires is as follows:

- 1) 10 cm of clean 0.127 mm 99.9% silver wire is used.
- 2) Immerse 20 mm of the wire for 8-10 minutes in a solution of 10% NaCN - 5% NaOH in water etches it to a fine point under a potential of 5V, with the wire positive. The etched wire has the correct shape when the current has fallen to 50% of its initial value.
- 3) It is then chlorided electrolytically in dilute HCl with a current of about 5 microamperes for 1 minute. This wire was then carefully positioned inside the borosilicate glass micropipette and temporarily secured with a drop of fast setting epoxy adhesive.

2.4.2.3. Results

Progress to date has reached only the point where microelectrodes can be fabricated and calibrated. No experimental results are available concerning crack electrochemistry.

2.5 Models of SCC, CF, Crevice Corrosion, and Pitting.

Stress corrosion cracking, corrosion fatigue, crevice corrosion, and pitting processes all depend upon electrochemical and mass transport processes which have been well-described mathematically (53-55). Because of thoughtful concern for the reader, the details are not reproduced here; however, mathematical manipulation is practiced widely upon the differential equations for ion transport, metal dissolution and hydrogen reduction kinetics, electrode potentials, size/shape of the crack, and external chemistry (essentially chloride ion concentration and pH) (56-62). For the most part, the results are not easily adapted to experimental evaluation.

Beck and Grens (63) developed one of the earliest quantitative models based on simultaneous differential equations, taking account of halide ion diffusion to the crack tip, hydrogen reduction on crack walls, production of soluble metal ions, and oxide formation on crack walls. Parkins (64) reviewed the various models and experimental evidence for them and, lacking the wisdom of Solomon, restated his earlier view (65) that each mechanism may be operative under various combinations of alloy, chemistry, and physics, i.e., no single mechanism can account for all instances of stress corrosion. Subsequently, a variety of interesting studies of the problem have appeared.

From potential measurements of electrolyte within pits and other observations, Pickering and Frankenthal (66) developed a modified model of pit growth which involves active dissolution and a high resistance path caused by hydrogen bubble occlusion. Simons, Rao and Wei (67) identified a slow step in the surface reaction of water vapor with steel (AISI 4340), correlated with the nucleation and growth of oxide film. Hydrogen, presumably produced in this reaction, was responsible for embrittlement. Comparing activation energies and other data, this step was determined to be

the rate controlling process for steel in water or water vapor. Oldfield and Sutton (68) developed a mathematical model of the initiation stage of crevice corrosion based on oxygen depletion within the crevice, followed by a lowered pH, permanent breakdown of the passive film, and rapid corrosion. Lees, Ford and Hoar (69) have reviewed (primarily their own) experimental work and theoretical views concerning practical methods for control of SCC and CF.

The model of Alkire and Siitari (70) of a long, narrow occluded cell with anode localized in the tip region predicted hydrogen reduction on side walls and external surface from metal-ion hydrolysis, diffusion of hydrogen ions, Ohm's law, Tafel kinetics, and construction of current lines. Alkire and Siitari (71) extended this model to the more complex three-dimensional case and solved the differential equations by computer to yield data for comparison with experimental results (72). Hebert and Alkire (73) used the model to describe experimental conditions of crevice corrosion initiation (74). Their model predicts rapid depletion of oxygen and acidification within the crevice, followed by increasing concentration of dissolved metal, but only negligible accumulation of chloride ion.

Turnbull (75) details a mathematical analysis of the time-dependent distribution of oxygen concentration along the length and across the width of a parallel-sided crack, and Turnbull and Thomas (76) offer a model of electrochemical conditions in a static crack in steel. Their model is based on the steady-state mass transport of species by diffusion and ion migration, anodic dissolution, hydrolysis of ferrous ions, and cathodic reduction of hydrogen ions, assuming that electrode reactions take place at both the tip and walls of the crack. Both pH and potential drop in the

crack were evaluated as functions of external potential, crack dimensions, and external chemistry in a 3.5% NaCl solution for a low alloy steel.

3. Experimental Results

3.1. Electrokinetics

3.1.1. Electrokinetic Apparatus.

Potentiostatic and galvanostatic measurements were performed using commercial equipment, including

(a) Princeton Applied Research (PAR) model 173

Potentiostat/Galvanostat,

(b) PAR Model 376 Logarithmic Current Converter,

(c) Wavetek Model 175 Arbitrary Waveform Generator, and

(d) Soltec VP-6414 S X-Y recorder

The waveform generator can be used to produce any desired potential/current function with respect to time, as well as built-in sine, square, triangle, and ramp waveform; the latter (ramp) was used in most experiments.

Experiments were performed in a PAR Model K47 Corrosion Cell System, with a square-shaped working electrode of one cm^2 area, and a saturated calomel electrode (SCE) as reference. The counter electrode consisted of twin high-density graphite rods. In potentiostatic operation, a PAR Model 178 Electrometer Probe was used to monitor the reference electrode.

3.1.2. Electrokinetics

3.1.2.1. Chloride Ion Concentration Effects

Anodic polarization profiles at the bare surface for concentrations between 0.1 wt.% and 3 wt.% NaCl at room temperature are shown in Figure 2. The corrosion potential of 7075-T6 Al alloy varies widely with the chloride concentration; as Cl^- concentration increases, corrosion potential decreases and corrosion current density increases. The profiles in Figure 2 were continuous, but were not adaptable to Tafel analysis because the linear region was too short. A very thin, dark gray adherent film formed on the surface of the specimen.

Cathodic profiles at the bare surface are shown in Figures 3 and 4 for 1% and 3% NaCl at room temperature; the current density is independent of the solution concentration. These profiles show the limiting current density resulting from oxygen reduction or oxide passivation. As potential is decreased, no deposit accumulated on the surface, nor was gas evolution or bubble formation observed.

3.1.3.2. Inhibitor Effects

Anodic polarization of 7075-T6 is shown in Figures 5 and 6 for NaNO_2 + $\text{Na}_2\text{B}_4\text{O}_7$ (0.1 wt.%) and 0.1 wt.% NaSCN solutions, respectively, with 1 wt.% NaCl. There are no discontinuities, which normally are associated with film formation, and no passivation. The corrosion potential was independent of the inhibitor concentration.

It is known that these inhibitors, NaNO_2 , NaNO_2 + $\text{Na}_2\text{B}_4\text{O}_7$ combined, and NaSCN increase passivation against chloride attack. The nitrite ion affects

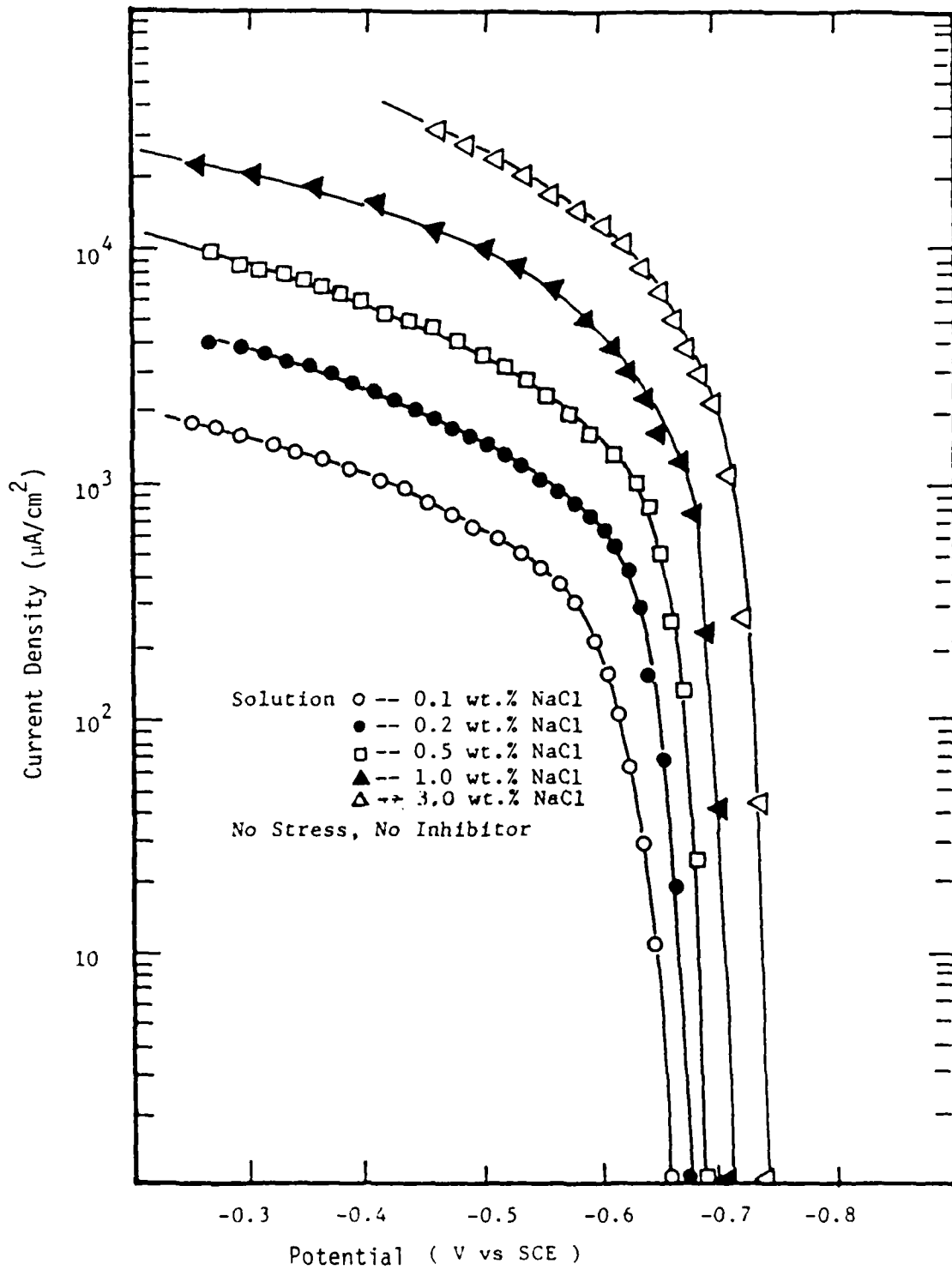


FIGURE 2. ANODIC POLARIZATION OF 7075 T6 AL ALLOY IN DILUTE SODIUM CHLORIDE SOLUTION WITHOUT STIRRING AT $20^{\circ}\text{C} \pm 2^{\circ}\text{C}$

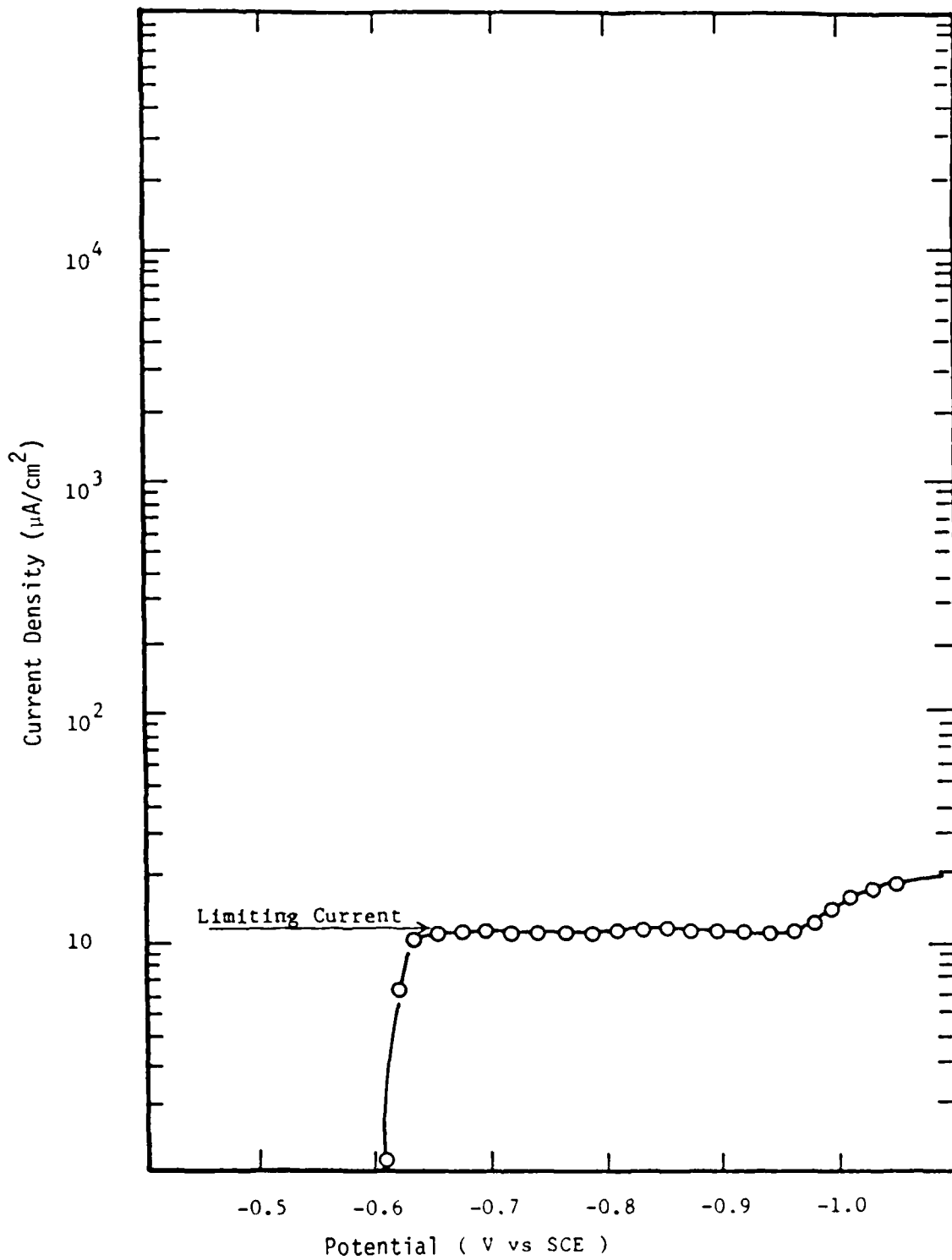
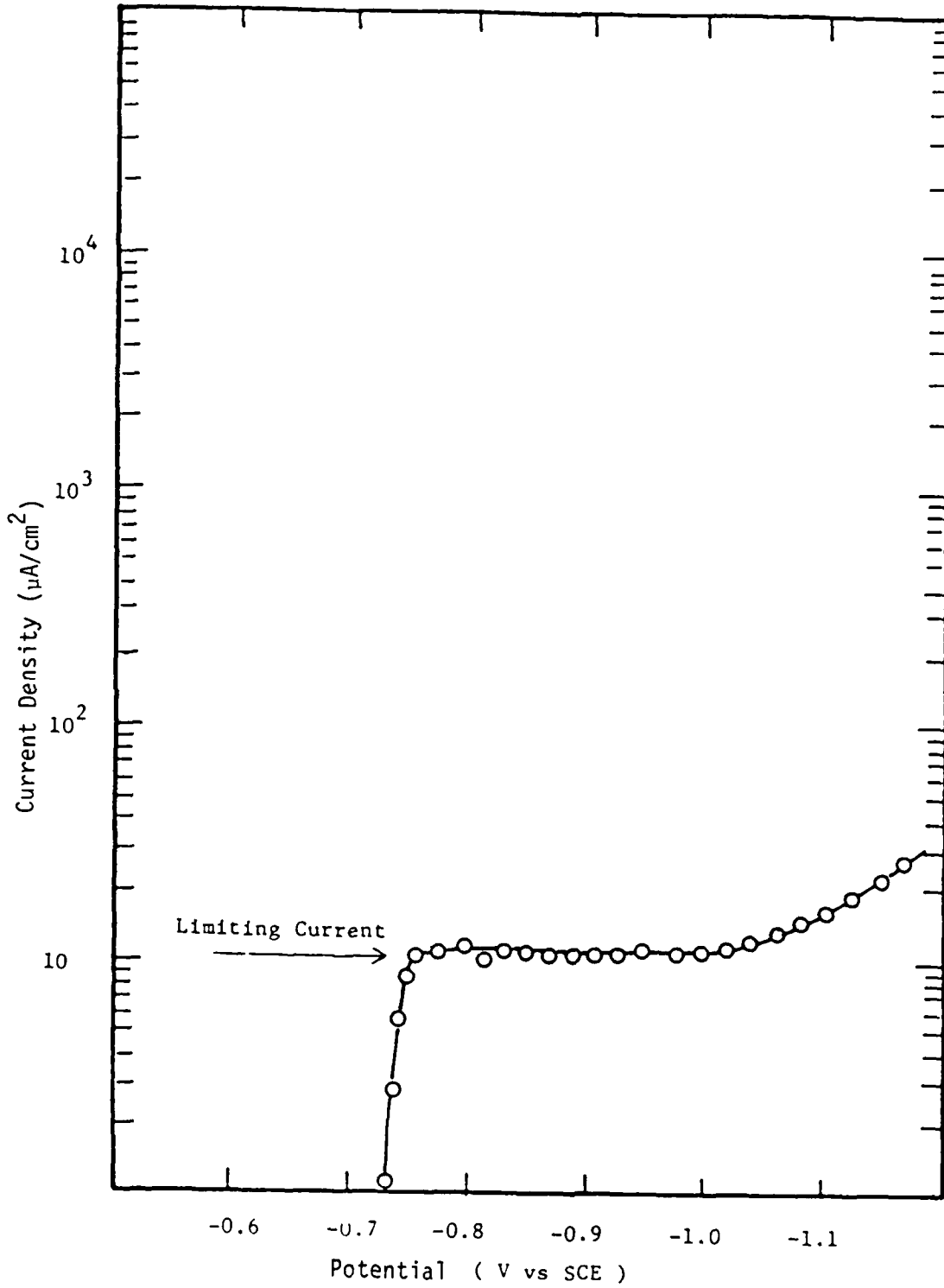


FIGURE 3. CATHODIC POLARIZATION OF 7075 T6 AL ALLOY IN 1 wt.% NaCl SOLUTION WITHOUT STIRRING AT $20^{\circ}\text{C} \pm 2^{\circ}\text{C}$



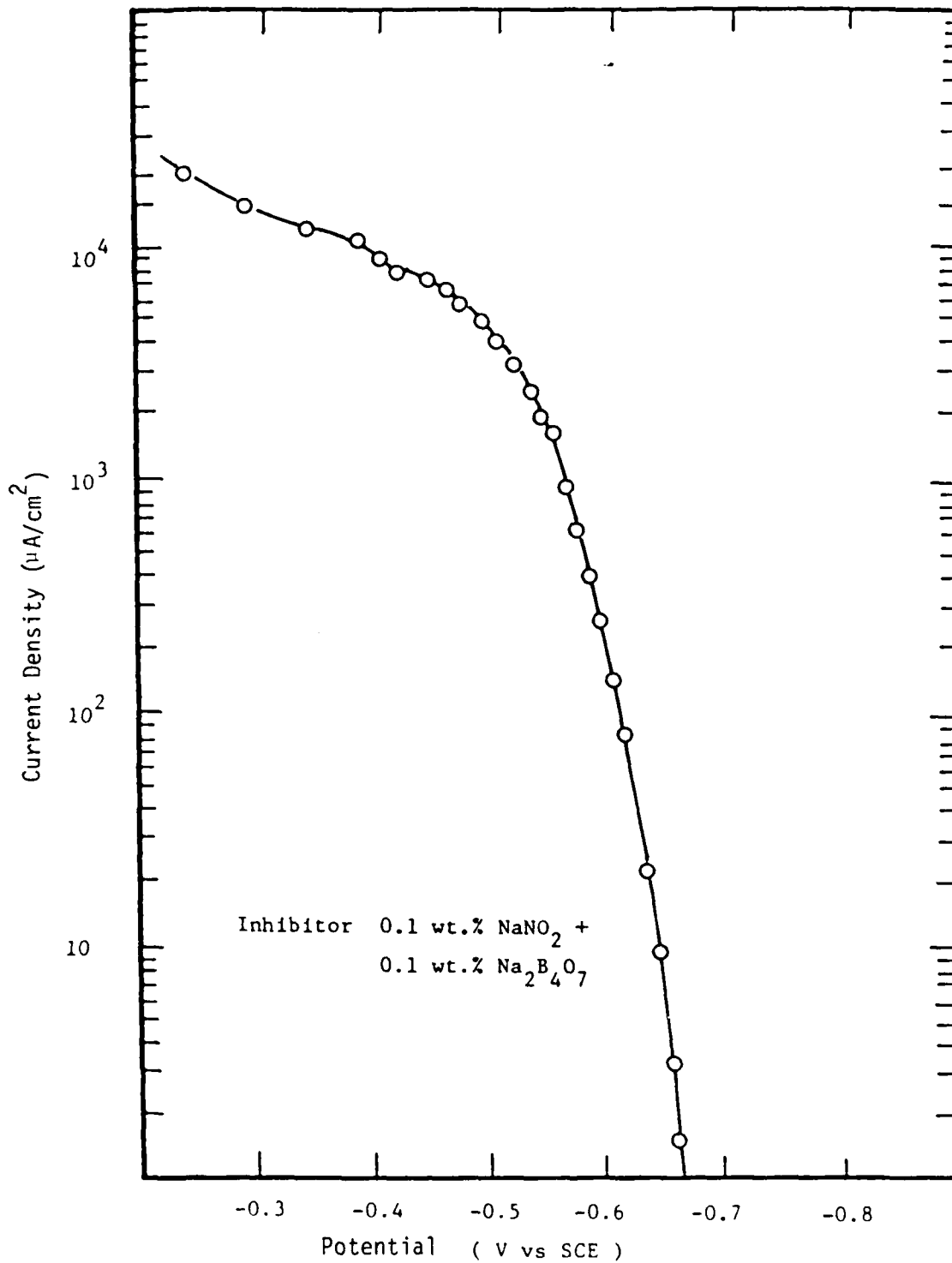


FIGURE 5. ANODIC POLARIZATION OF 7075 T6 AL ALLOY IN 1 wt.% NaCl AND INHIBITOR WITHOUT STIRRING AT 20°C ± 2°C

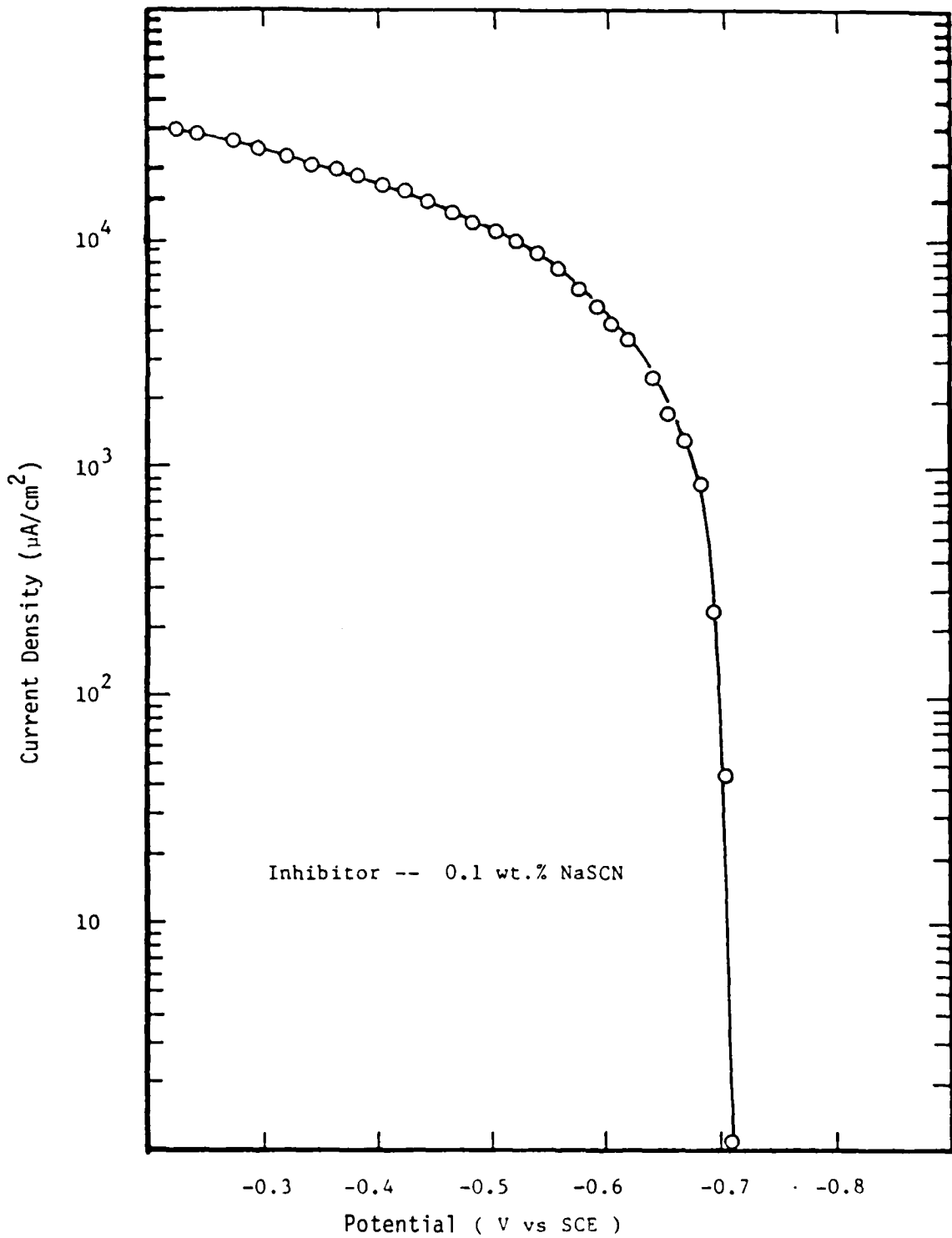
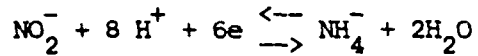


FIGURE 6. ANODIC POLARIZATION OF 7075 T6 AL ALLOY IN 1 wt.% NaCl AND INHIBITOR WITHOUT STIRRING AT $20^{\circ}\text{C} \pm 2^{\circ}\text{C}$

the potential, that is, those salts whose anions have high redox potentials, e.g.,



$$E = + 0.90 \text{ V, SHE.}$$

The anodic profile, Figure 5, shows a small effect of NaNO_2 and $\text{Na}_2\text{B}_4\text{O}_7$ upon polarization behavior, but no effect is seen in Figure 6.

The passive film formed by NaNO_2 in this inhibitor concentration range is ineffective against chloride even when the inhibitor concentration also is high. Oxidizing inhibitors, by providing an additional cathodic reactant, effectively reduce cathodic polarization, thus increasing the corrosion current. If added in insufficient quantity, oxidizing inhibitors can have disastrous consequences. If no passivation results, as in these experimental results, anodic dissolution increases or the passive film is weak.

Figures 7 and 8 show the anodic polarization behavior of 7075-T6 Al alloy in the inhibitor solutions. CH_3COONa and $(\text{COONa})_2$, respectively, with 1 wt.% NaCl. Acetate and oxalate ions are chelating agents, i.e., ions or molecular species with two or more atoms having unshared pairs of electrons. The chelating agent can donate the unshared electron pair to a metal atom to form a stable 5- or 6-member ring resembling a "claw," with the result that the metal atom is held in a stable configuration and the chelate produced usually does not exhibit the properties of the metal atom or the chelating agent. In the case of aluminum alloys, the chelating agent can react with

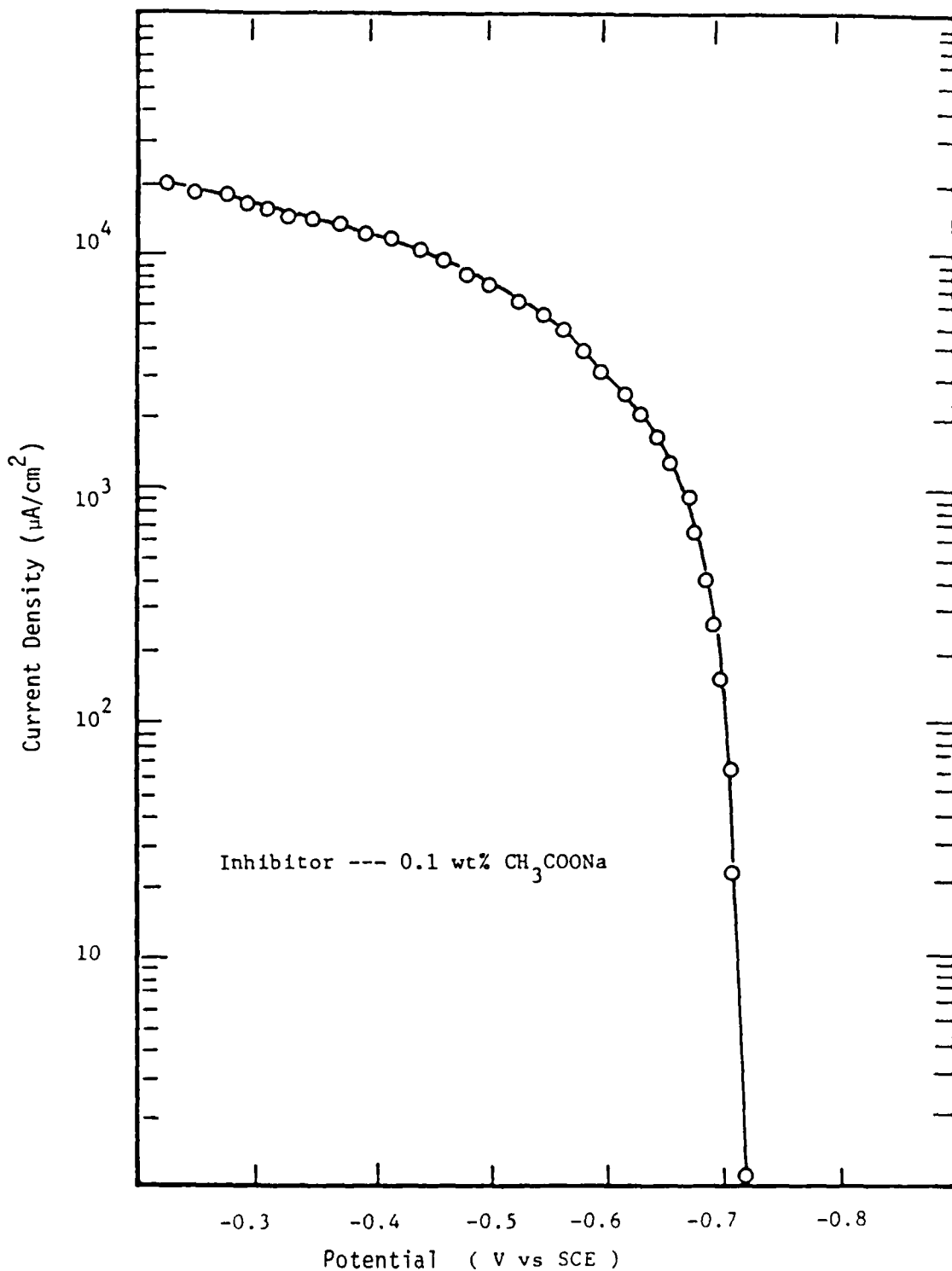


FIGURE 7. ANODIC POLARIZATION OF 7075 T7 AL ALLOY IN 1 wt.% NaCl AND INHIBITOR WITHOUT STIRRING AT 20°C ± 2°C

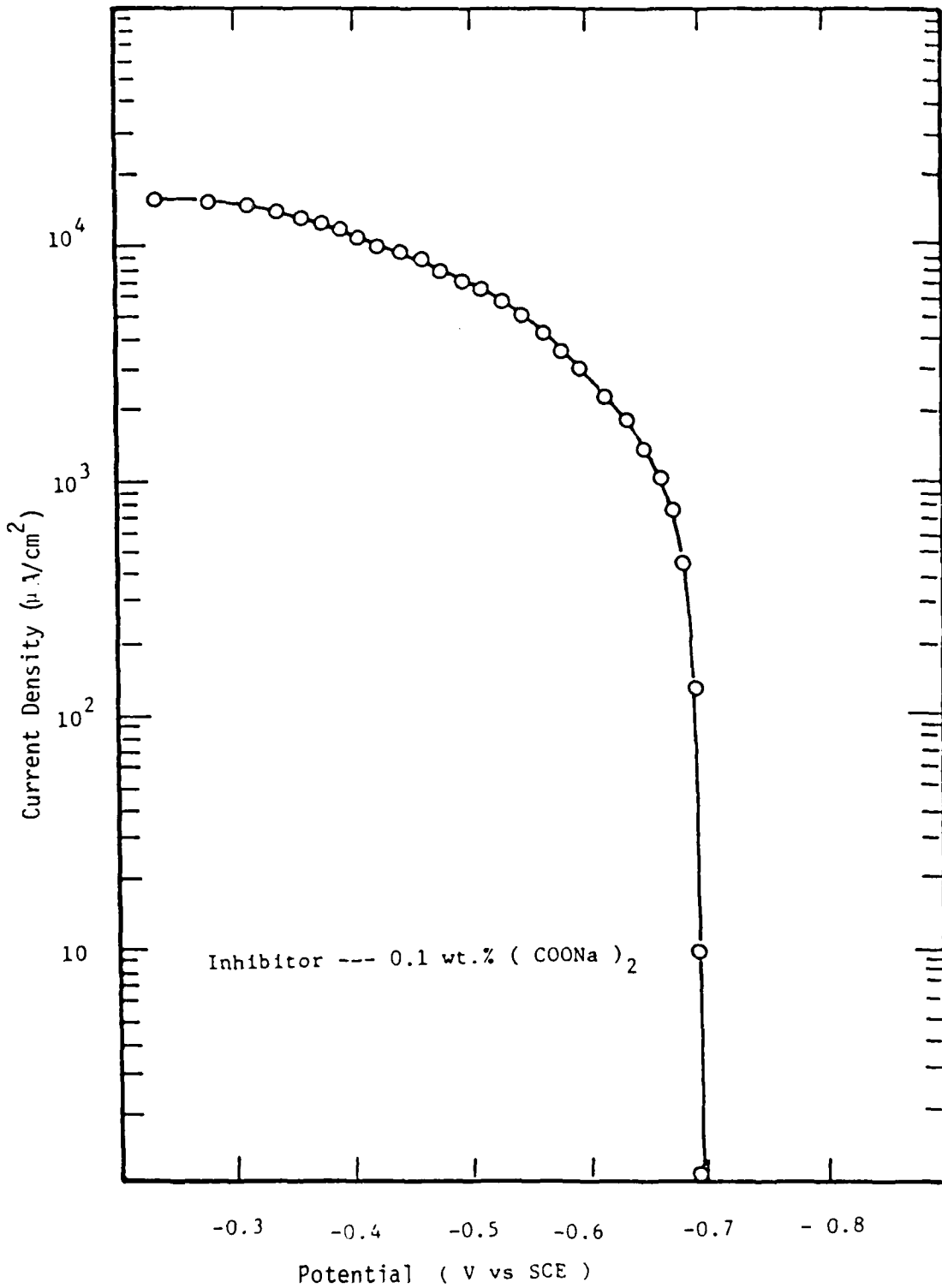
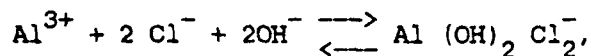


FIGURE 8. ANODIC POLARIZATION OF 7075 T6 AL ALLOY IN 1 wt.% NaCl AND INHIBITOR WITHOUT STIRRING AT 20°C ± 2°C

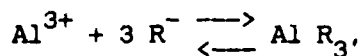
the aluminum cation in the oxide film. Depending on the chelating agent, the resulting compound may be stable and insoluble, or it may be a stable, soluble, complex ion with a solubilizing function on the oxide.

No change was observed in corrosion potential or anodic polarization curves when sodium acetate and sodium oxalate were added to 1% NaCl. Metallographic examination of specimens showed general corrosion on the surface. As an inhibitor, a chelating agent reacts with aluminum to form insoluble aluminum oxalate or acetate, preventing aluminum corrosion by a precipitation effect.

In chloride solutions, inhibition may be viewed as interference with the reaction



by which the oxide film is thinned. A species may form a complex ion which may be stable and soluble,



wherein the species Al R_3 is stable, uncharged and very slightly ionized and resides at or near the aluminum surface. Although precipitation inhibitors are known to prevent aluminum corrosion in the presence of chloride, our results showed no effect on the polarization of 7075-T6 Al alloy.

Figure 9 shows the anodic polarization behavior of 7075-T6 Al alloy in the presence of borate-nitrite ($0.1\% \text{NaNO}_2 + \text{Na}_2\text{B}_4\text{O}_7$) inhibitor, with small

additions of surfactant, such as 2-amino-2-methyl-1-propanol, to the 1% NaCl solutions. Small additions of surfactants have been reported to improve inhibition by borate-nitrite and to provide good protection to aluminum in high chloride-containing solutions (66, 72, 92). Figure 8 shows that the corrosion potential moved in the active direction by the addition of surfactant, from -0.710 V (vs SCE) to -1.049 V. The corrosion potential was greatly altered by 2-amino-2-methyl-1-propanol. During the equilibration, a thick black oxide film formed. With the potential increasing to -0.630 V, the current density remains constant because of oxide formation on the specimen surface. At a potential of -0.550 volt (vs SCE), the oxide slightly breaks down and the anodic current density increases because of the occurrence of surface gas formation. As the potential is increased, the oxide film continues to form.

According to Figure 9, small additions of 2-amino-2-methyl-1-propanol affects the anodic polarization curve, and provides protection in the presence of chloride ion. Surface active compounds interfere with the dissolution reaction by interacting with the passive film provided by the inhibitors, resulting in the development of a stronger adsorbed protective film.

Potentiodynamic cathodic polarization curves at room temperature and at 2 wt.% NaCl, Figure 4, and 1 wt.% NaCl + 0.1 wt.% NaNO₂ are shown in Figure 10, respectively. The cathodic polarization curve shows a limiting current density (ca. 11.5 $\mu\text{A}/\text{cm}^2$), caused by hydrogen evolution from -1.08 V to -0.715 (vs SCE); gas evolution on the surface was observed. As the potential is decreased, the gas evolution rate increased. The anodic polarization curve also shows a limiting current density (ca. 15.5 $\mu\text{A}/\text{cm}^2$) resulting

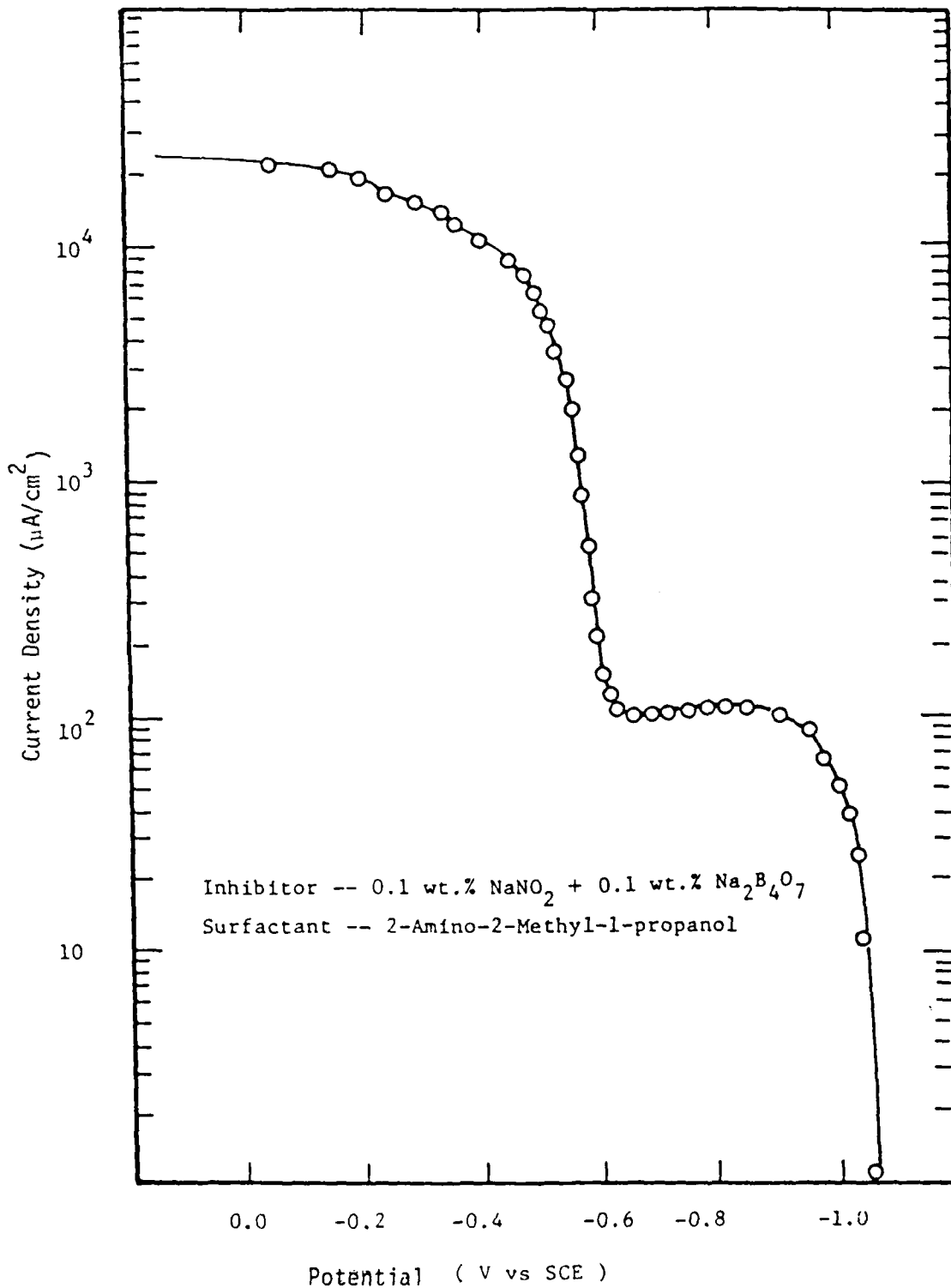


FIGURE 9. ANODIC POLARIZATION OF 7075 T6 AL ALLOY IN 1 wt.% NaCl, INHIBITOR AND SURFACTANT WITHOUT STIRRING AT 20°C ± 2°C

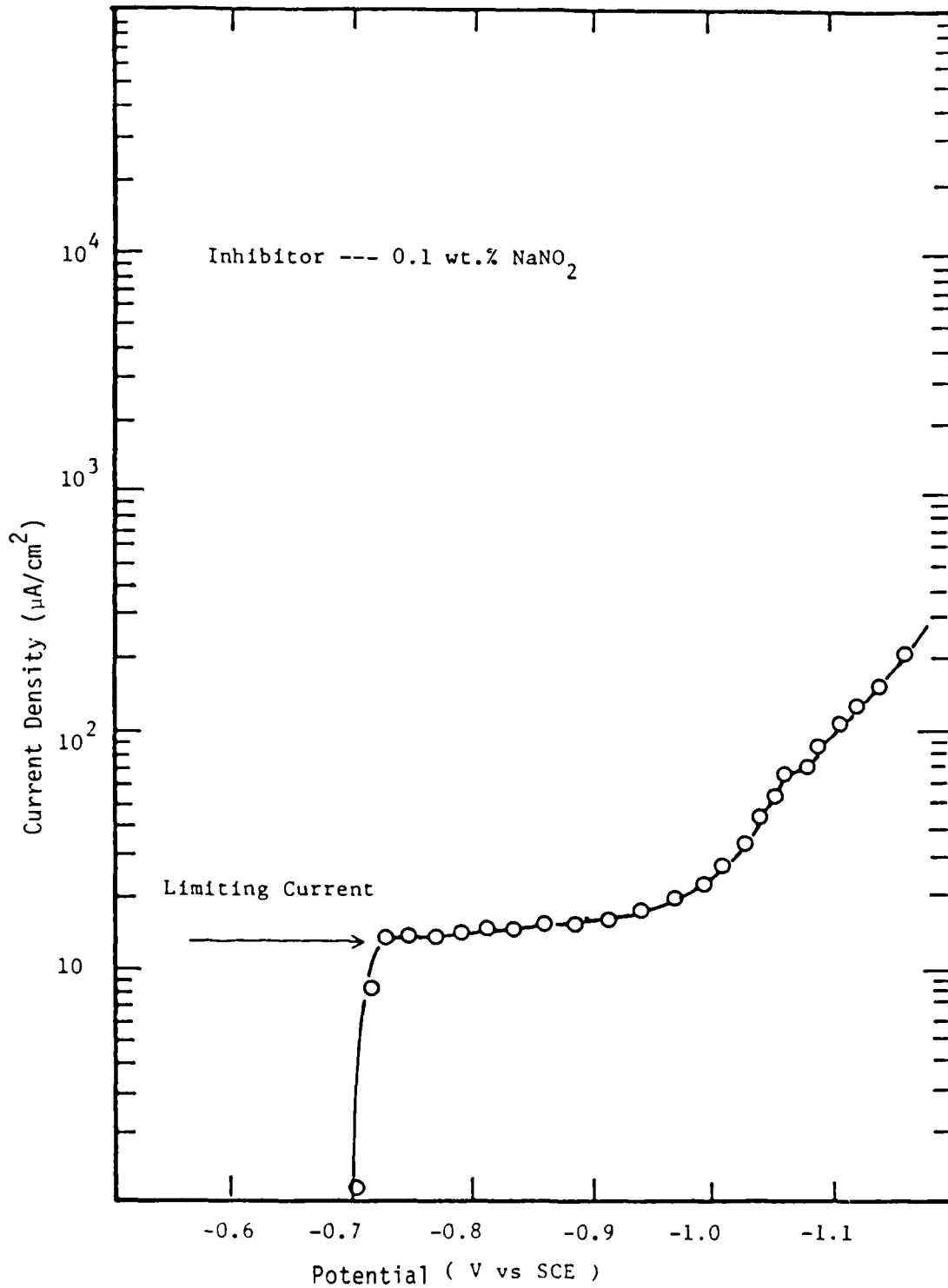


FIGURE 10. CATHODIC POLARIZATION OF 7075 T6 AL ALLOY IN 1 wt.% NaCl AND INHIBITOR WITHOUT STIRRING AT $20^{\circ}\text{C} \pm 2^{\circ}\text{C}$

from oxygen reduction of hydrogen evolution reaction between -0.910 (vs SCE) and -0.715 (vs SCE). The inhibitor, NaNO_2 , effects a raising of the potential.

These results propted a more thorough study of the inhibitive properties of NaNO_2 , $\text{Na}_2\text{B}_4\text{O}_7$, and surfactants, either alone or in combinations, and particularly in the presence of chloride ion. The results of electrokinetic studies are shown in Figures 11-16. Sodium nitrite alone, Figure 10, is an effective inhibitor, but clearly exhibits a reverse effect at concentrations above 0.1 wt.%, where corrosion currents increase. In the presence of sodium chloride, sodium nitrite has no useful inhibitive properties (Figure 12). When coupled with borax, Figure 13, the passivating effect of 0.1 wt.% NaNO_2 is slightly diminished, but still effective. Addition of 0.1 wt.% NaCl , Figure 14, however, essentially cancels the inhibitive effects. Higher concentrations, Figure 15, result in no significant changes. The inhibitor formulation (IF) of Lynch and coworkers (27), Table 3, also were evaluated, Figure 16, with similar results.

Although nitrite is thought to prevent aluminum corrosion in the presence of chloride, in fact it either reduces cathodic polarization or induces the limiting current density. Thus, while nitrite is a passivator, it is ineffective against chloride attack because of the reduced cathodic polarization.

Preliminary experiments have been performed with sodium hyponitrite alone and in combination with sodium chloride. Anodic polarization results to date suggest that the hyponitrite has a strong passivating effect of 7075-T6 aluminum alloy, but is less effective than sodium nitrite. This

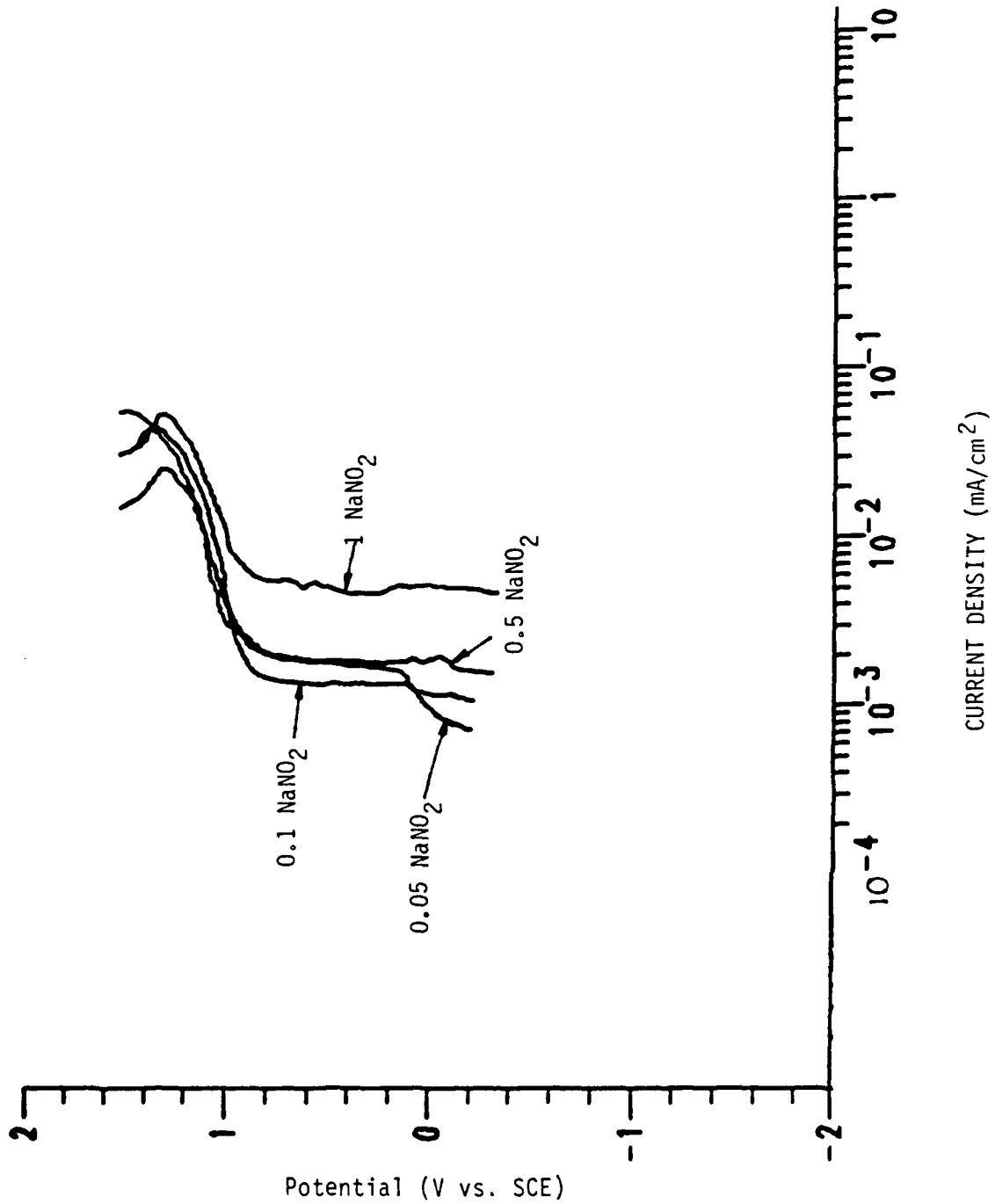


Figure 11. Anodic polarization of 7075-T6 aluminum alloy in aqueous solutions of NaNO₂, 20°C, concentrations are wt.%.

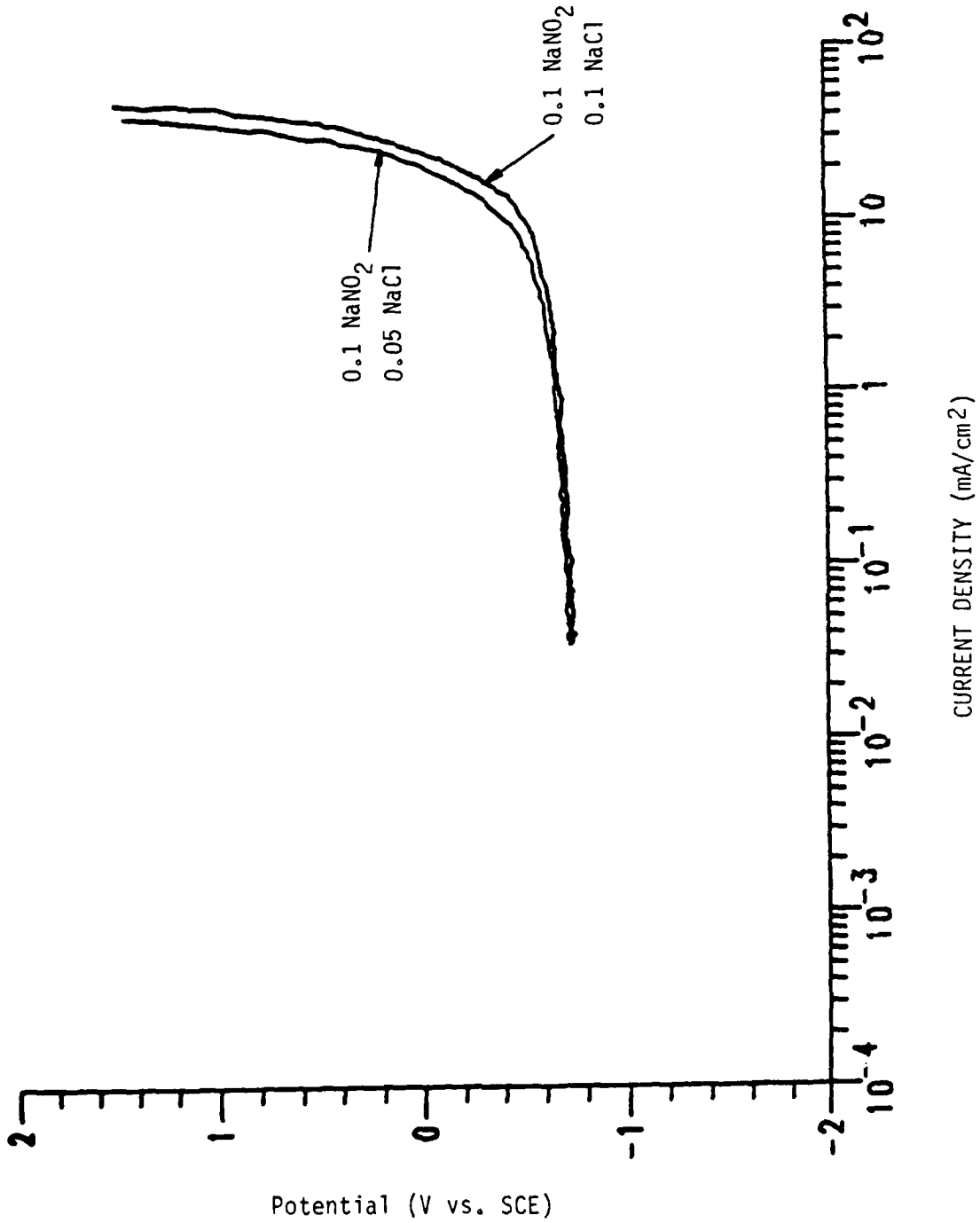


Figure 12. Anodic polarization of 7075-T6 aluminum alloy in aqueous 0.1 wt.% NaNO₂, with 0.05 and 0.1 wt.% NaCl, 20°C.

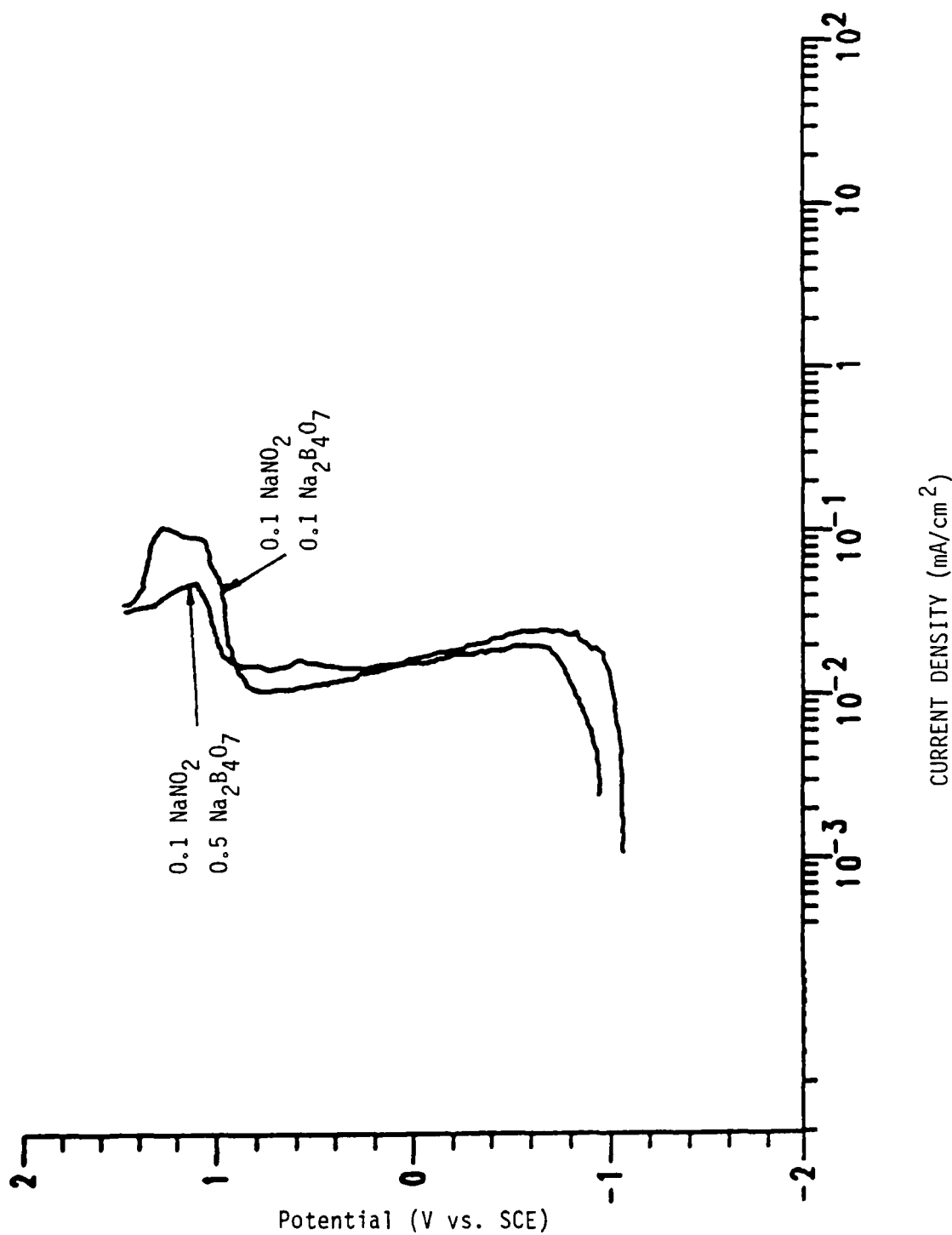


Figure 13. Anodic polarization of 7075-T6 aluminum alloy in aqueous 0.1 wt.% NaNO₂ with 0.1 and 0.5 wt.% Na₂B₄O₇, 20°C.

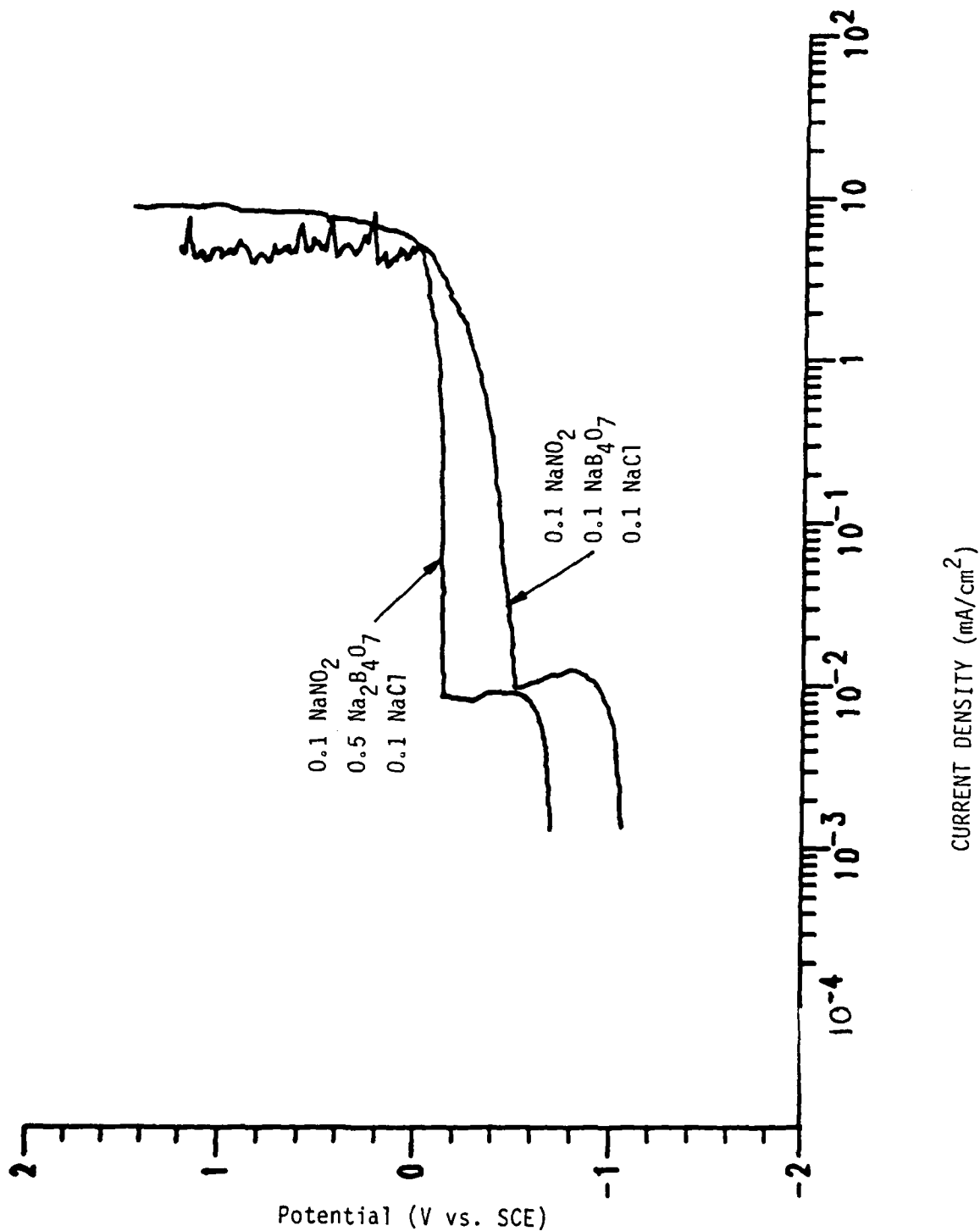


Figure 14. Anodic polarization of 7075-T6 aluminum alloy in aqueous solutions of NaNO₂, Na₂B₄O₇, and NaCl, 20 C. Concentrations are wt.%.
2
1
0
-1
-2
Potential (V vs. SCE)
10⁻⁴ 10⁻³ 10⁻² 10⁻¹ 1 10 10²
CURRENT DENSITY (mA/cm²)
0.1 NaNO₂
0.5 Na₂B₄O₇
0.1 NaCl
0.1 NaNO₂
0.1 NaB₄O₇
0.1 NaCl

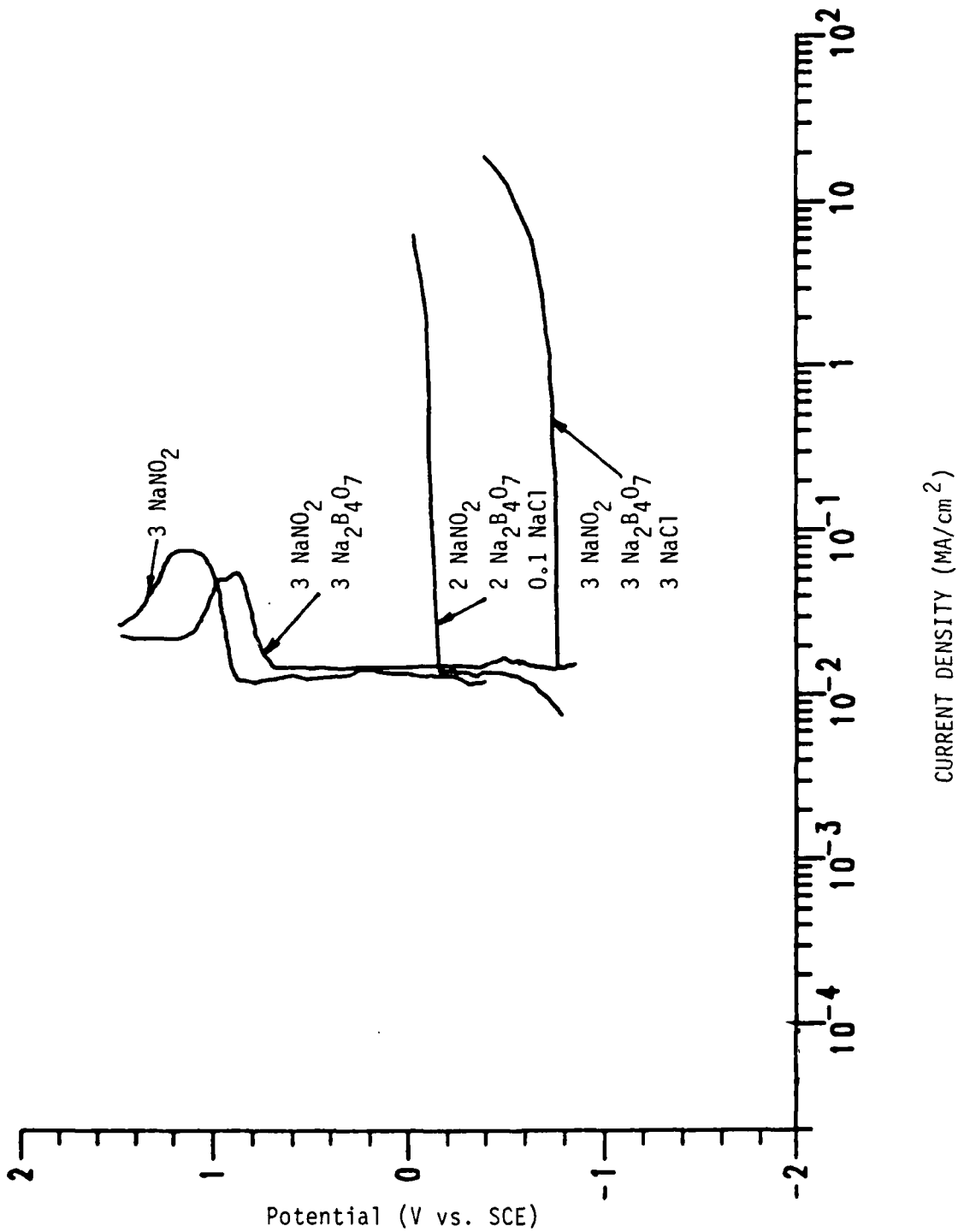


Figure 15. Anodic polarization of 7075-T6 aluminum alloy in aqueous solutions of NaNO₂, Na₂B₄O₇, and NaCl, 20°C. Concentrations are wt.%.

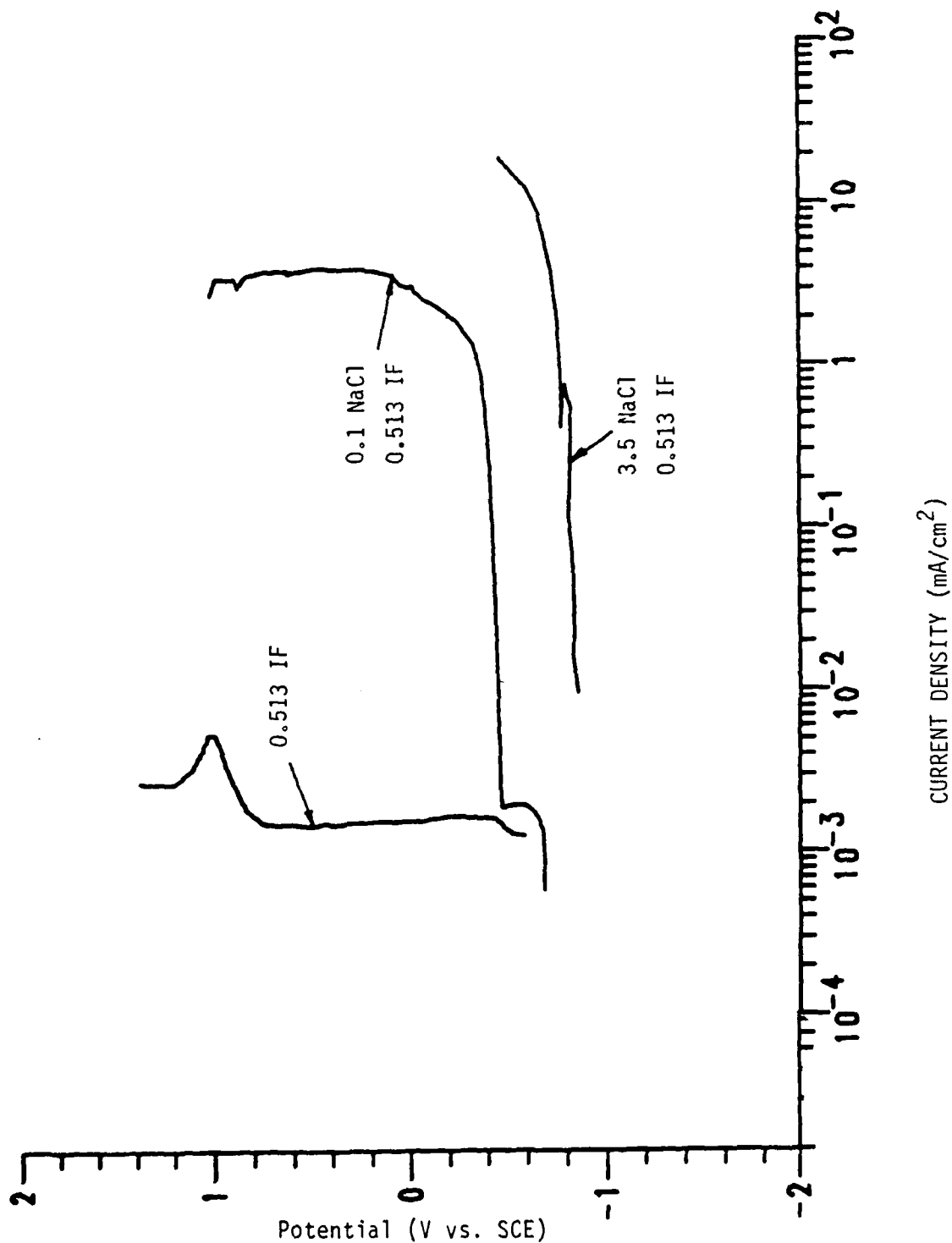


Figure 16. Anodic polarization of 7075-T6 aluminum alloy in aqueous multifunctional inhibitor (27) and NaCl, 20°C, concentrations are wt.%.

would be consistent with the lower oxidation state of nitrogen in hyponitrite. When sodium chloride is present, the passivation is effectively destroyed as is the case with nitrite. Passivation is lost at a significantly higher potential, however, perhaps reflecting different redox potentials noted in Section 2.2. It is premature to draw conclusions at this time.

The linear polarization technique is suitable for determination of corrosion rates. Instead of imposing a large voltage change, typical of the Tafel method, linear polarization involves only 10-30 mV swings positive or negative from the corrosion potential, in increments of about 1 mV. A plot of current vs. potential is a straight line according to the Stern-Geary equation,

$$\left(\frac{\Delta E}{\Delta I} \right)_{E-O} = R_p = B / i_{\text{corr}}$$

where R_p is polarization resistance, and i_{corr} is the corrosion current density.

In Figure 17, polarization measurements of 7075-T6 (a) without inhibitor and surfactant, (b) with only surfactant, and (c) with surfactant and inhibitor are shown. Values of R_p are taken from the initial slopes of the curves. In Figure 18, polarization measurements on 7075-T6 Al with inhibitor and 1 wt.% NaCl are shown. Thus, the inhibitor may be effective on a bare surface specimen in the presence of chloride. If, however, a surfactant is added, chloride is prevented from attacking Al alloy.

3.1.3.3. Stress Effects

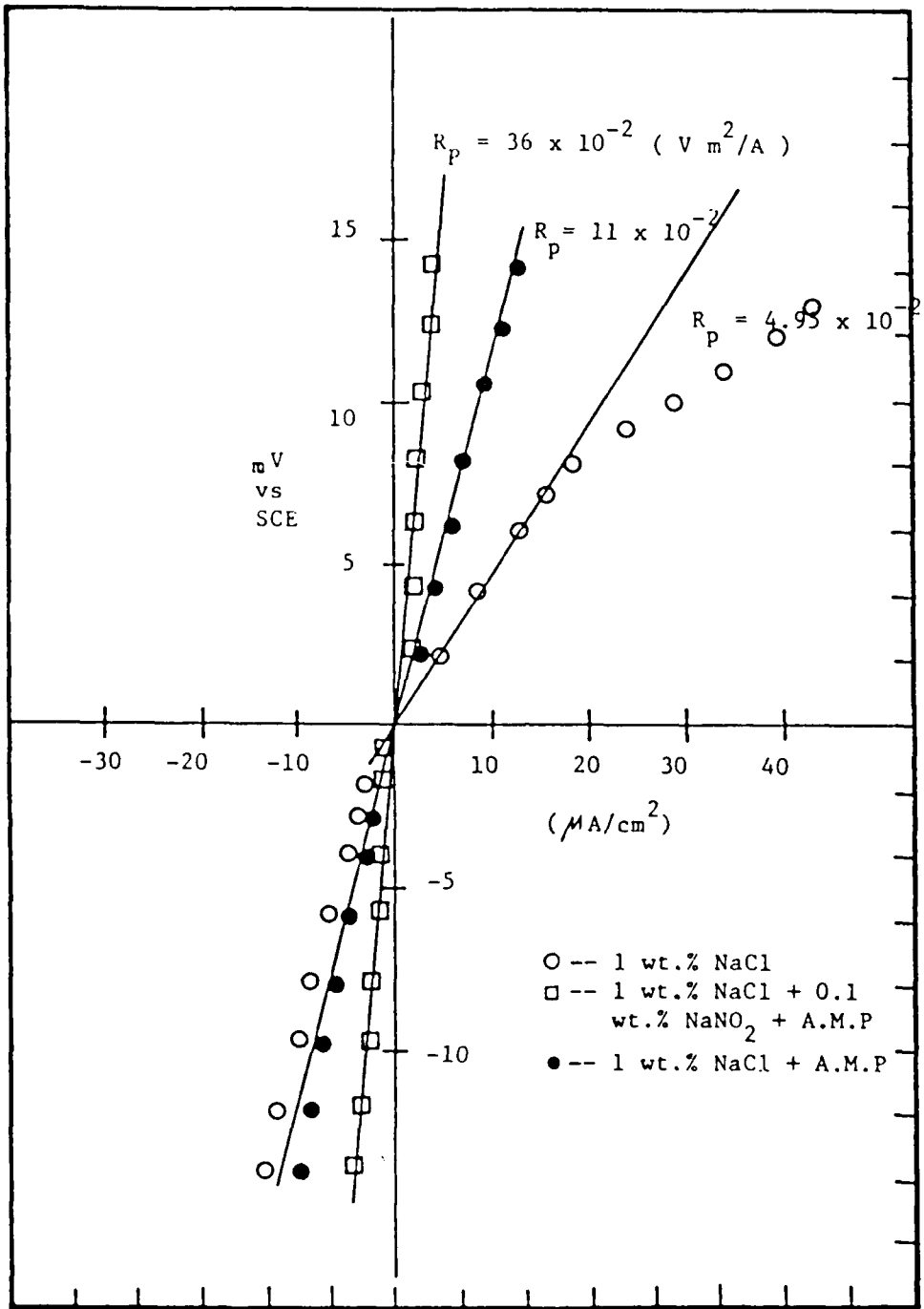


FIGURE 17. LINEAR POLARIZATION OF 7075 T6 AL ALLOY IN 1 wt.% NaCl UNDER VARIOUS CONDITIONS WITHOUT STIRRING AT $20^\circ\text{C} \pm 2^\circ\text{C}$

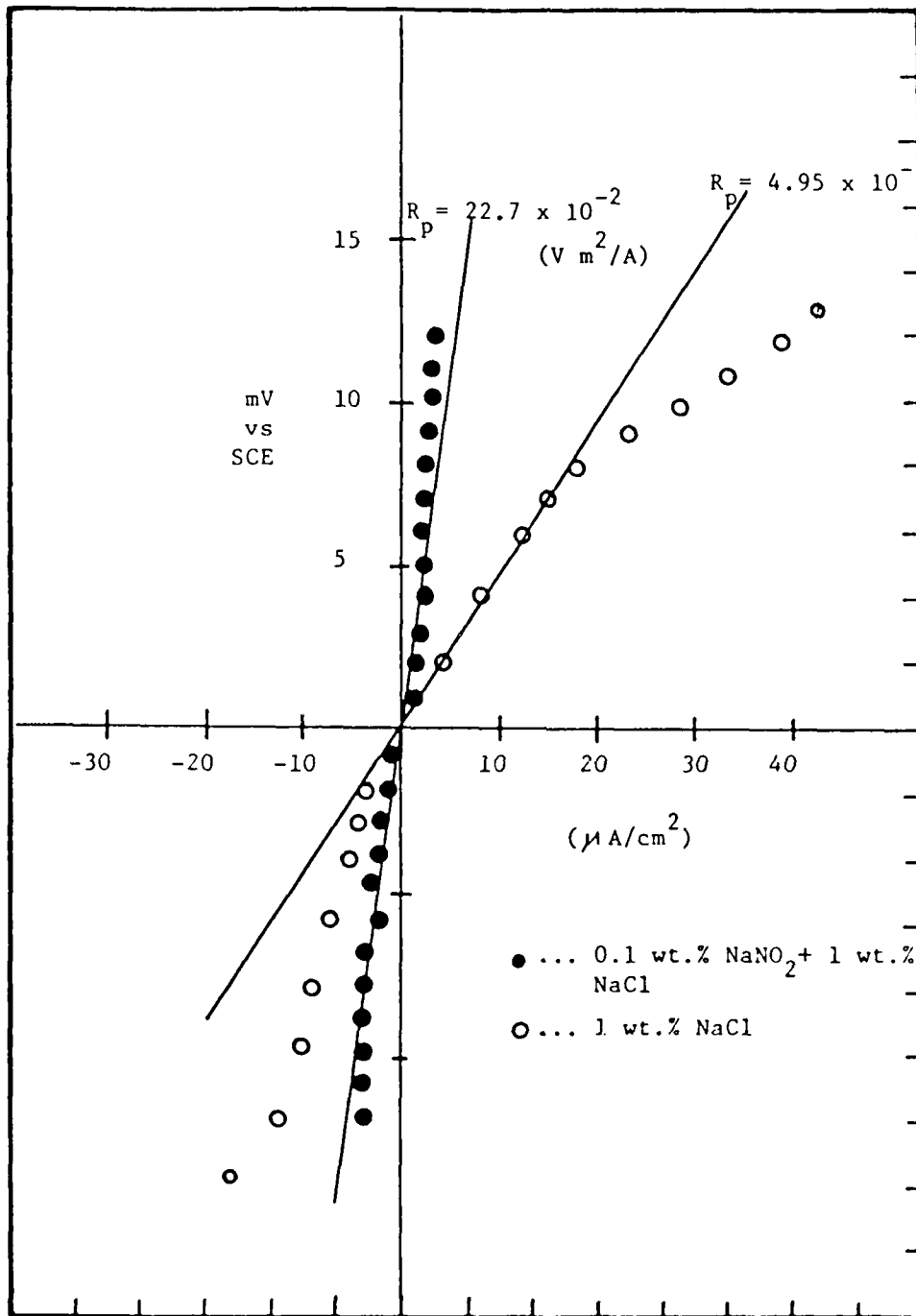


FIGURE 18. LINEAR POLARIZATION OF 7075 T6 AL ALLOY IN 1 wt.% NaCl WITHOUT STIRRING AT $20^\circ\text{C} \pm 2^\circ\text{C}$

In Figure 19, the anodic profile is shown for 1 wt.% NaCl at room temperature with stress. The corrosion potential is moved 15mV in the active direction as a result of applied stress, and current density is increased. Although the profile is continuous, it is not adaptable to Tafel analysis because of a short linear region. A thin white adherent film formed on the surface of the specimen, as potential is increased, a surface deposit continued to accumulate, while gas evolution was observed. Thus, applied stress affects the polarization behavior of 7075-T6 and raises the current density. Furthermore, stress affects the type of oxide film formed at the surface.

3.1.3.4. Crack Electrochemistry

Mechanisms proposed for corrosion inside a crack, contain three basic components, alone or in combination: differential aeration, localized acidification, and migration of chloride ions. Analyses have been made of NaCl solution without inhibitors for (1) an "isolated" crevice, where crevice metal was not coupled to the open external metal; and (2) a "coupled" crevice.

In Figure 20, anodic profiles are presented for 0.5, 1 and 3 wt.% NaCl concentrations at bare surfaces and in isolated cracks. Gas bubbles were observed at potentials between -0.850 V to 0.600 V, and negative current was observed. At higher potential, the curves are linear with smooth slopes. Anodic profiles for isolated crevices show that anodic dissolution inside the isolated crevice is independent of chloride concentration. Anodic dissolution inside the crevice, however, is much higher than at the bare surface. Our data show that, in this potential range, hydrogen evolution may take place because negative current under anodic condition and profuse

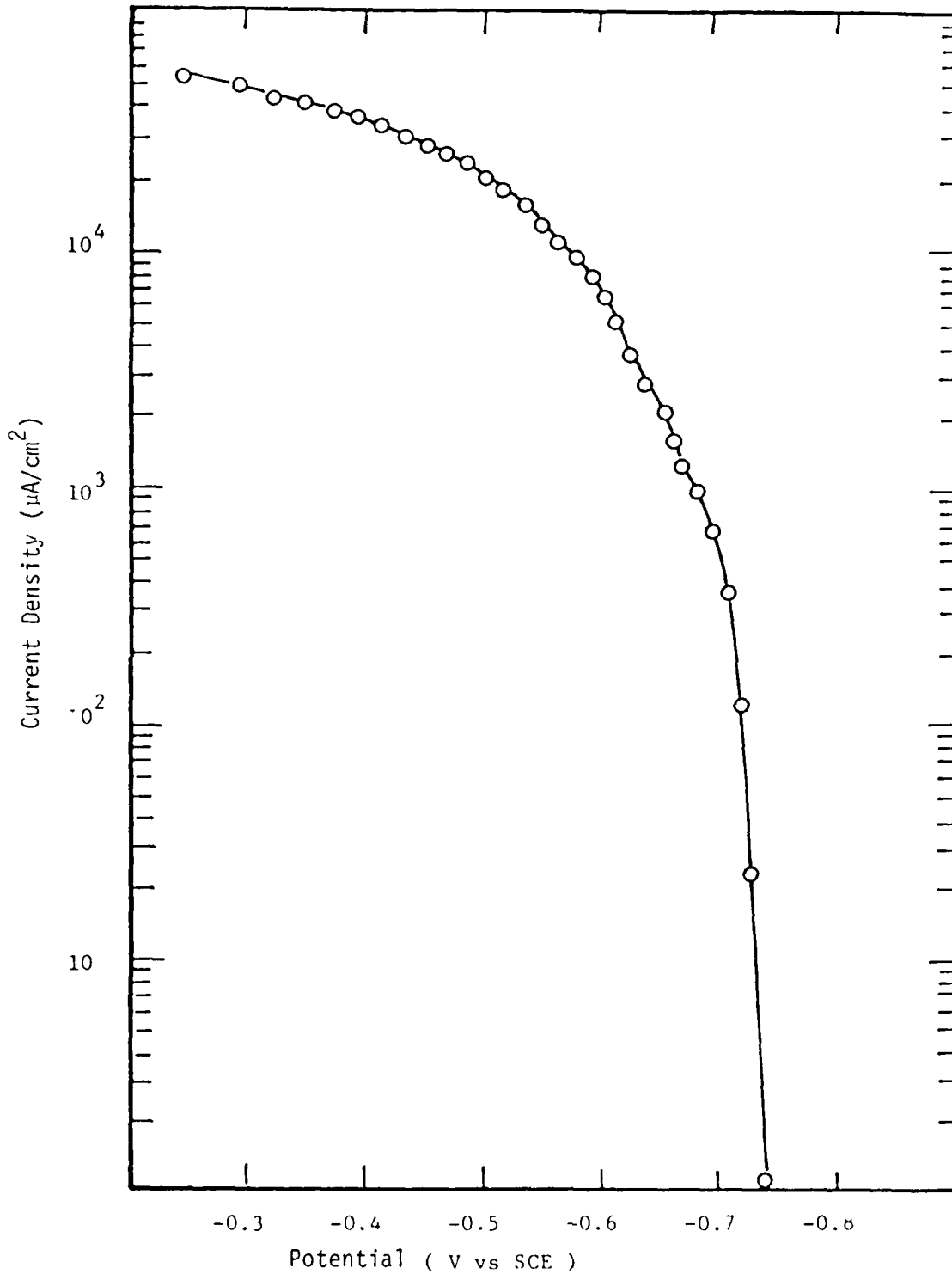


FIGURE 19. ANODIC POLARIZATION OF 7075 T6 AL ALLOY IN 1 wt.% NaCl UNDER STRESS WITHOUT STIRRING AT $20^{\circ}\text{C} \pm 2^{\circ}\text{C}$

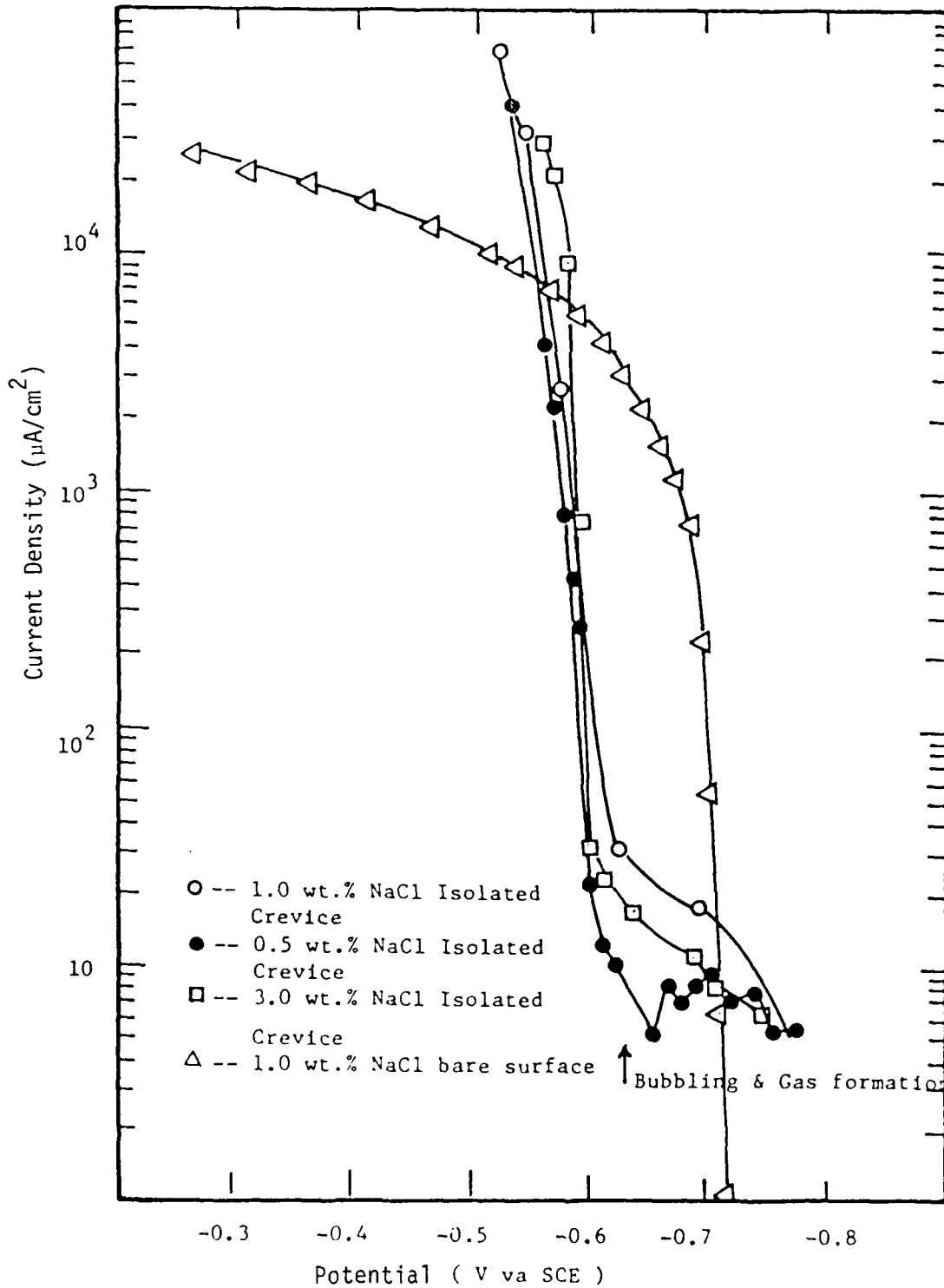


FIGURE 20. ANODIC POLARIZATION OF 7075 T6 AL ALLOY IN DILUTE NaCl SOLUTION

bubble formation were observed. The gas extracted was determined to be hydrogen. Within this potential range, hydrogen reduction is possible thermodynamically in aqueous media to pH 10 (77).

Under cathodic polarization for the isolated crack in 1 and 3 wt% NaCl Figures 21 and 22, gas bubbles were observed over the entire range of potentials. Cathodic profiles for isolated crevices show the limiting current; cathodic polarization is dependent of chloride concentration, but current density increased with increasing chloride concentration.

Time dependence of the open circuit corrosion potential was measured using an isolated artificial crack immersed in NaCl with and without inhibitors, Figure 23. Solutions (1.0 wt% NaCl with and without 0.1 wt% NaNO_2 + 0.1 wt% $\text{Na}_2\text{B}_4\text{O}_7$) were aerated without stirring. For the bare surface electrode (no connection to crack), after the electrode was placed in solution (1 wt% NaCl without inhibitor), there was a small increase in open circuit potential (-0.755 to -0.730 V vs SCE), and the electrode potential slightly increased.

After 3.5 hr. (the induction time), the potential remained at a constant value, ca -0.710 V vs SCE. But, when placed in inhibited solution (1 wt.% NaCl + 0.1 wt.% NaNO_2 + 0.1 wt. $\text{Na}_2\text{B}_4\text{O}_7$), a rapid increase in potential from -1.016 to -0.924 V occurred. After 2 hr, the potential remained at a constant value, ca. -0.710 V, approximately the same as at a bare surface. After an isolated crack electrode was put in chloride solution without inhibitor, the corrosion potential attained about -0.880 V; after 7 hr., the potential remained constant at ca. -0.810 V, much less than for the bare surface electrode.

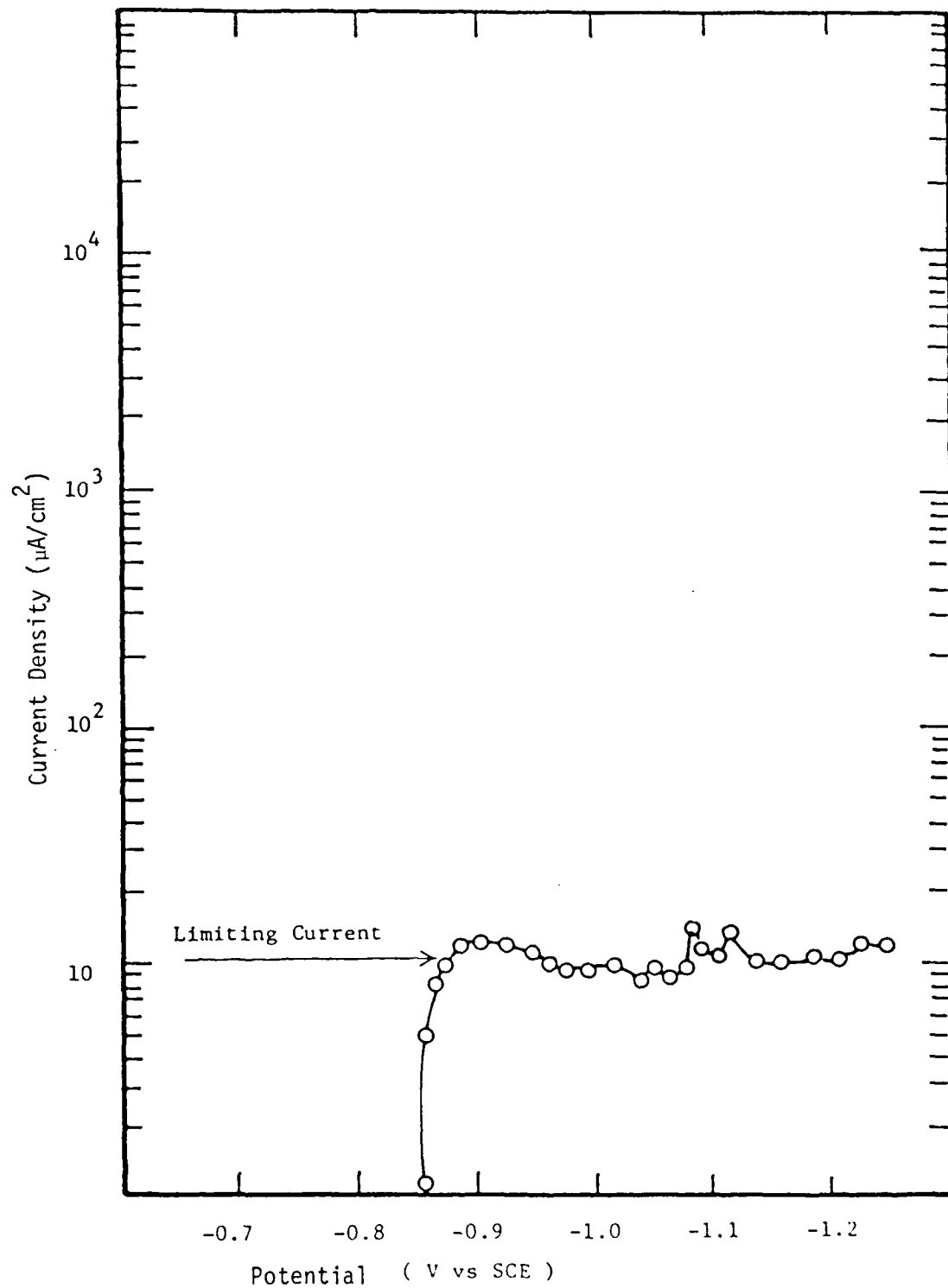


FIGURE 21. CATHODIC POLARIZATION OF 7075 T6 AL ALLOY IN 1 wt.% NaCl SOLUTION AND CREVICE WITHOUT STIRRING AT $20^{\circ}\text{C} \pm 2^{\circ}\text{C}$

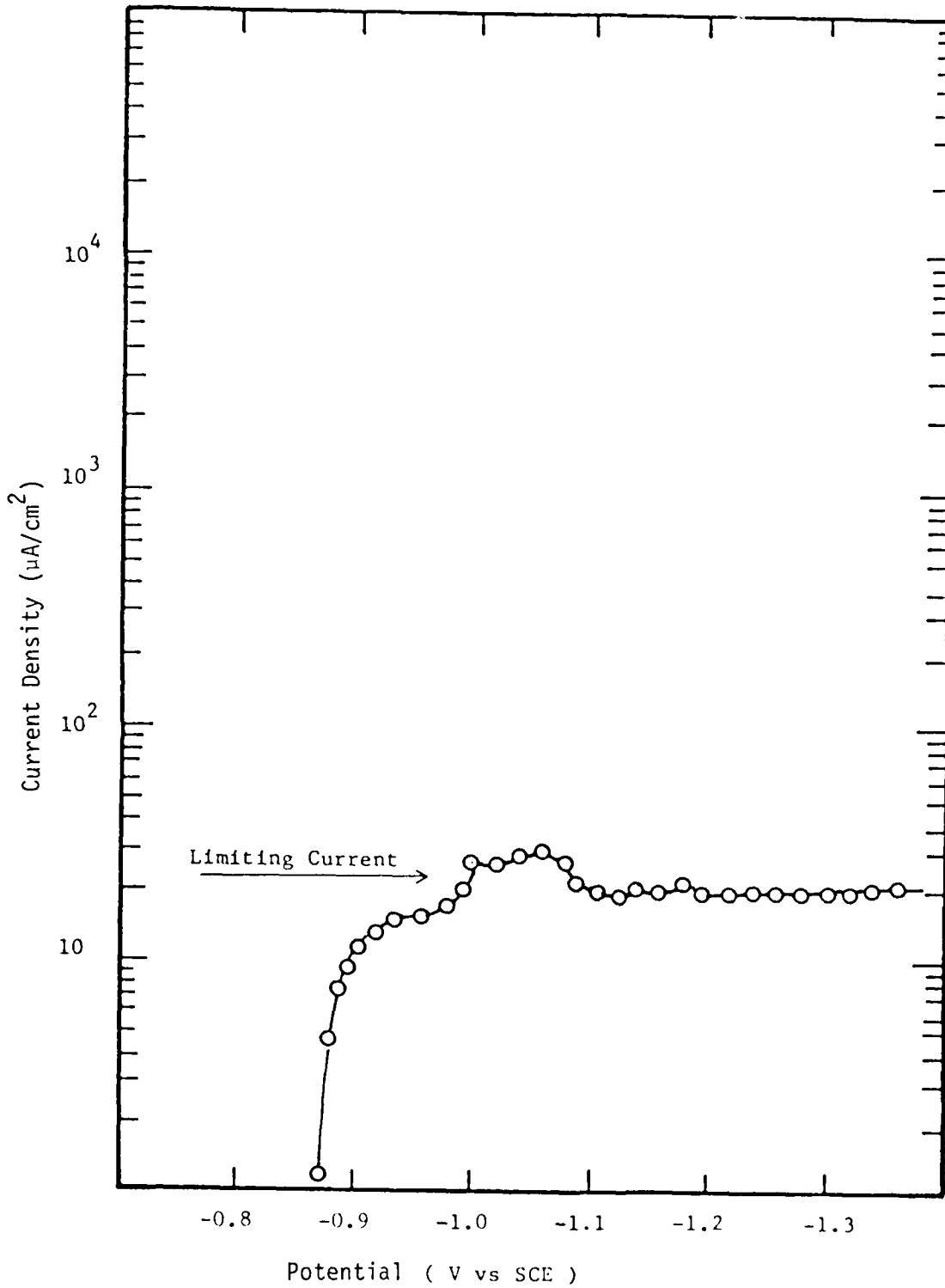


FIGURE 22. CATHODIC POLARIZATION OF 7075 T6 AL ALLOY IN 3 wt.% NaCl SOLUTION AND CREVICE WITHOUT STIRRING AT $20^{\circ}\text{C} \pm 2^{\circ}\text{C}$

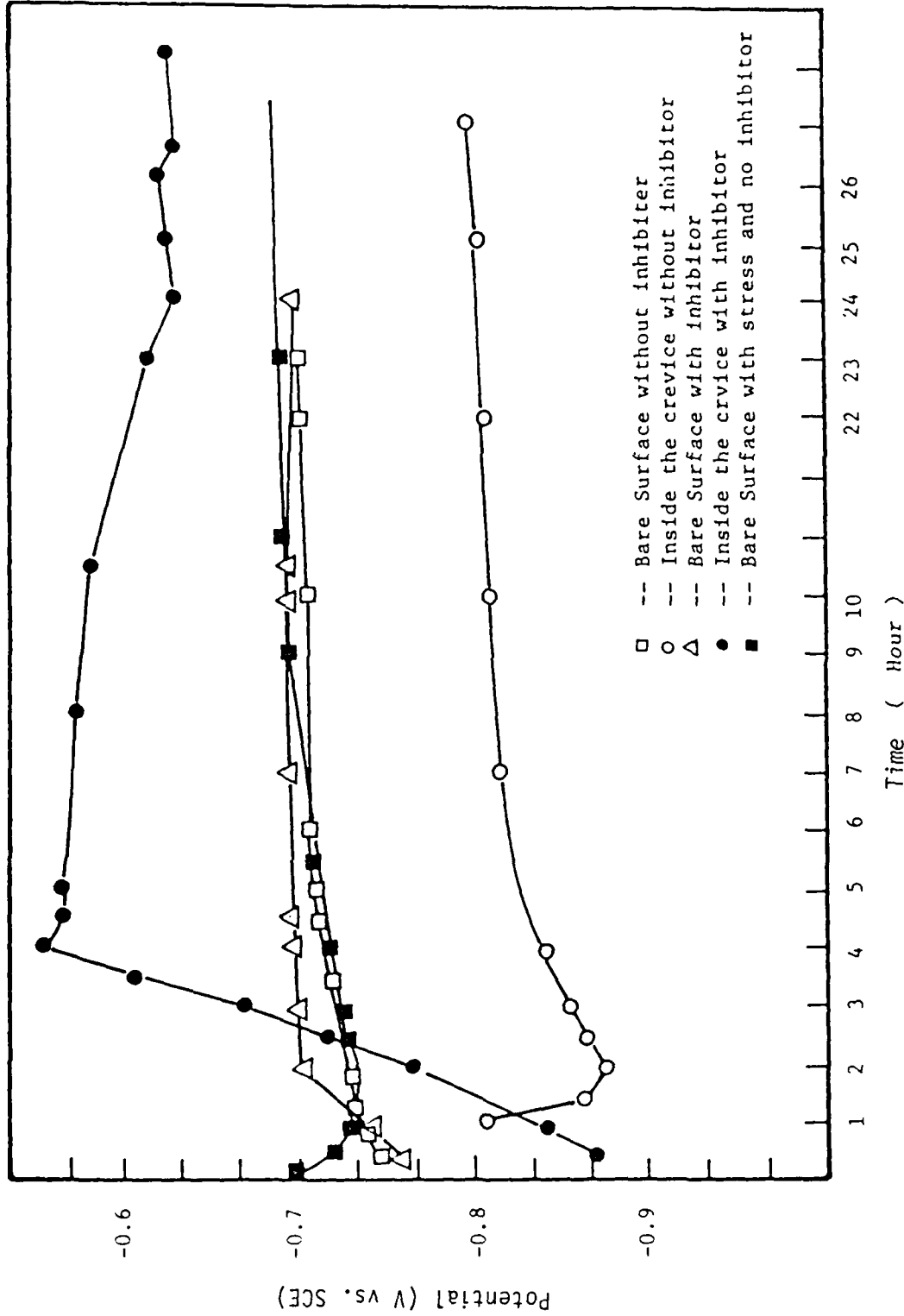


FIGURE 23. STEADY-STATE OPEN-CIRCUIT POTENTIALS FOR OPEN AND CREVICE 7075 T6 AL ALLOY IN DILUTE NaCl SOLUTION WITH AND WITHOUT INHIBITORS

When the artificial crevice electrode was placed in inhibited chloride solution (1 wt.% NaCl with 0.1 wt.% NaNO_2 + 0.1 wt.% $\text{Na}_2\text{B}_4\text{O}_7$), the corrosion potential moved rapidly in the noble direction from -0.890 to -0.820 V, and continued to increase, reaching a value after four hours of ca. -0.550 V. After 20 hr, the potential was ca. -0.630 V, higher than the bare surface electrode, with and without inhibitor, and the cracked electrode (isolated) without inhibitor. Figure 24 shows the open circuit corrosion potential time dependence at different positions inside the crack. The solution, 1.0 wt.% NaCl, was aerated with no stirring. A small potential drop was measured inside the crack (isolated crack).

3.1.3.4.2. Coupled Crack

While we have considered electrochemical conditions inside the uncoupled crack, a real crevice always is in contact with metal outside the crack, hence, we have studied the polarization behavior of a "coupled" crevice. Anodic profiles are shown in Figure 25 for 1 wt.% NaCl a bare uncoupled surface in 1 wt.% NaCl. Gas bubbles were observed between -0.850 V to -0.700 V, both on the bare surface and inside the crack, and current oscillation was observed, above these potentials, curves are linear with smooth slopes. Some references (67, 78) report that the cathodic reaction (oxygen reduction) continues outside the crack after the oxygen within the crack has been consumed, and anodic reaction is confined to the crack.

Current densities for the isolated (uncoupled) crack are compared with to that for Al alloy couples under various concentration in Figure 26 . In solutions (3 wt.% NaCl and 1 wt.% NaCl), Figure 26, gas evolution was observed between -0.800 V to -0.730 V on the bare surface as well as inside the crack, but the rate of gas formation inside the crack was less than at

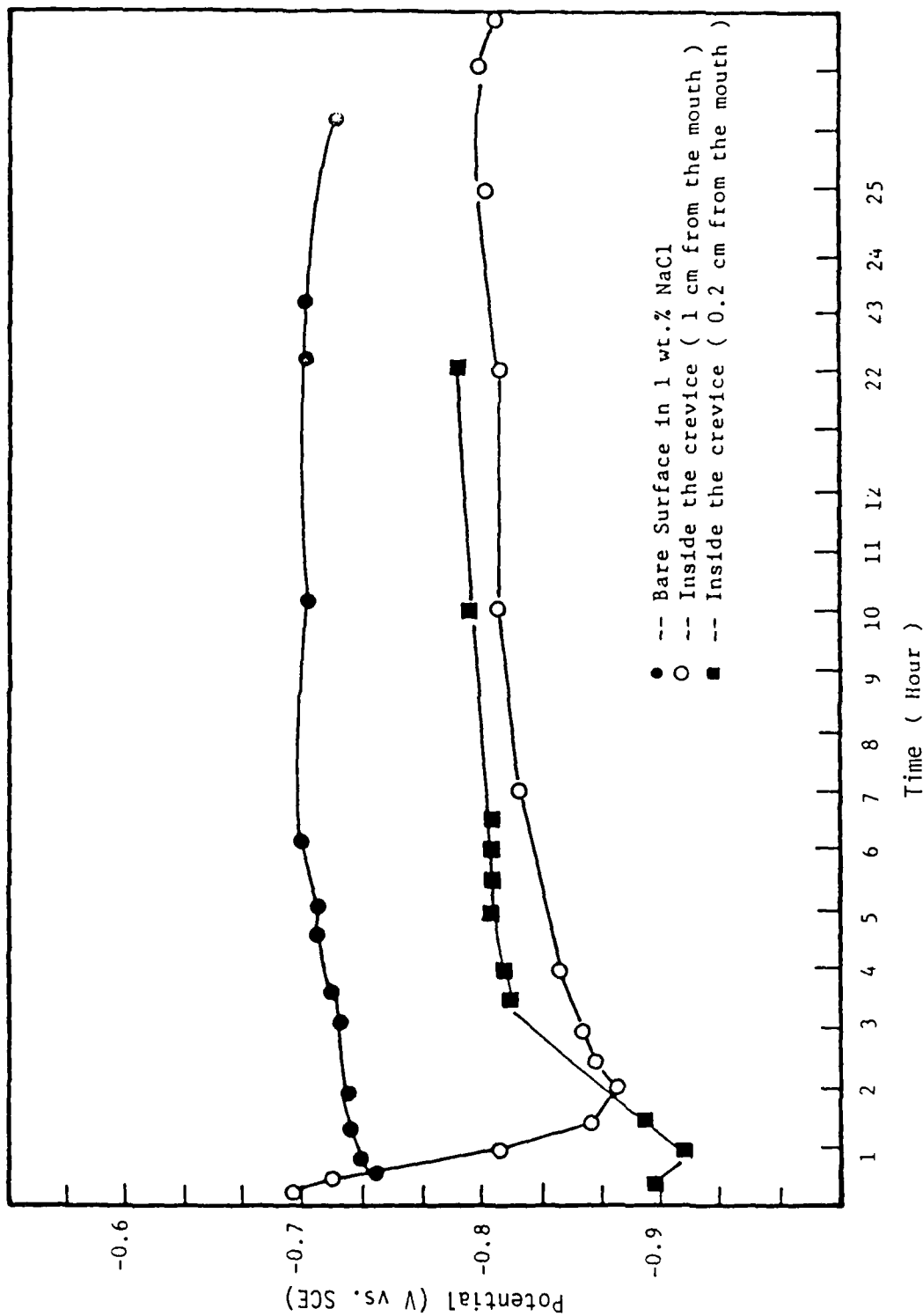


FIGURE 24. STEADY-STATE OPEN-CIRCUIT POTENTIALS FOR OPEN AND CREVICE 7075 T6 ALLOY IN DILUTE NaCl SOLUTION

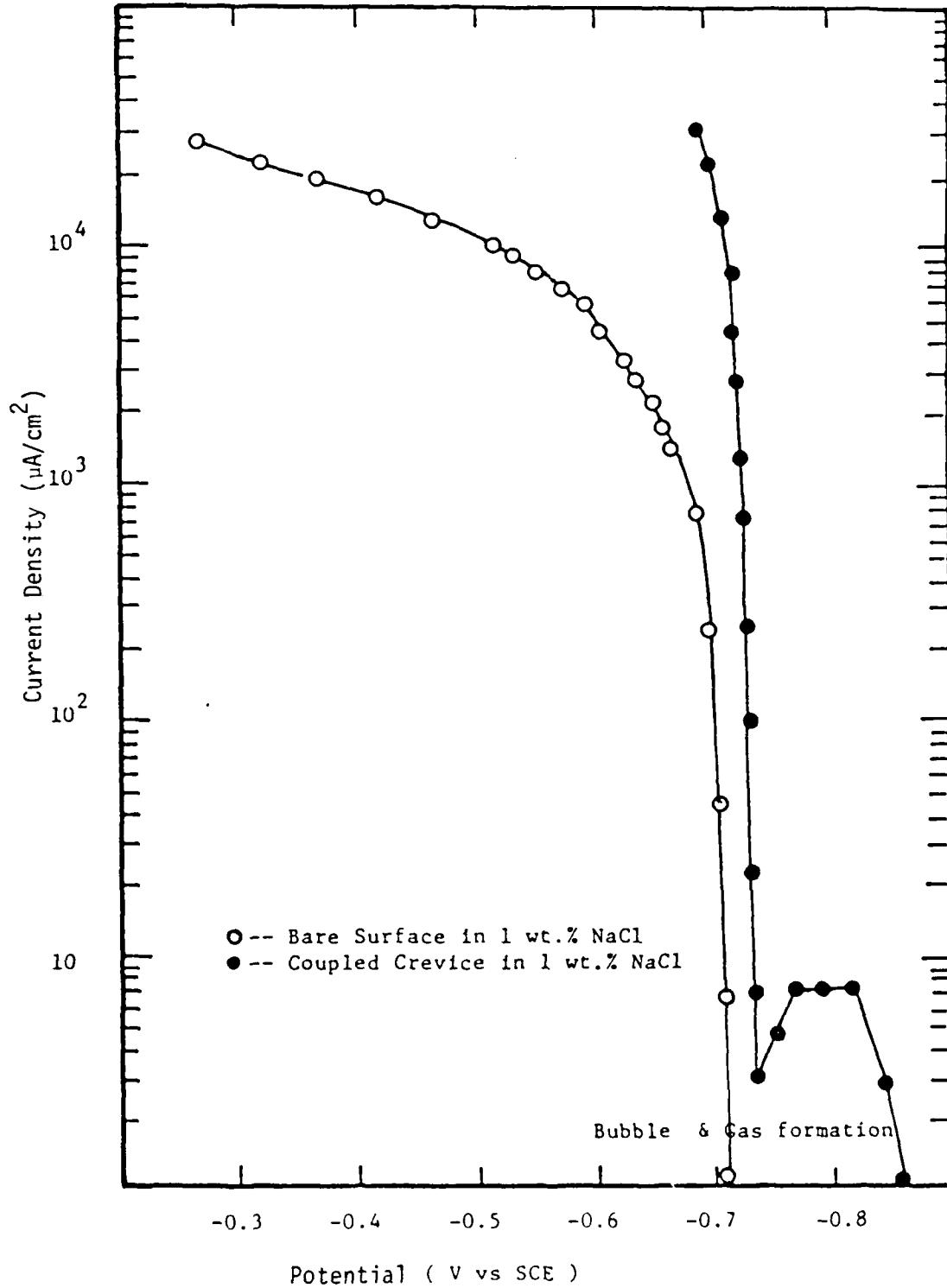


FIGURE 25. ANODIC POLARIZATION FOR OPEN AND CREVICE 7075 T6 AL ALLOY IN 1 wt.% NaCl SOLUTION WITHOUT STIRRING AT $20^{\circ}\text{C} \pm 2^{\circ}\text{C}$

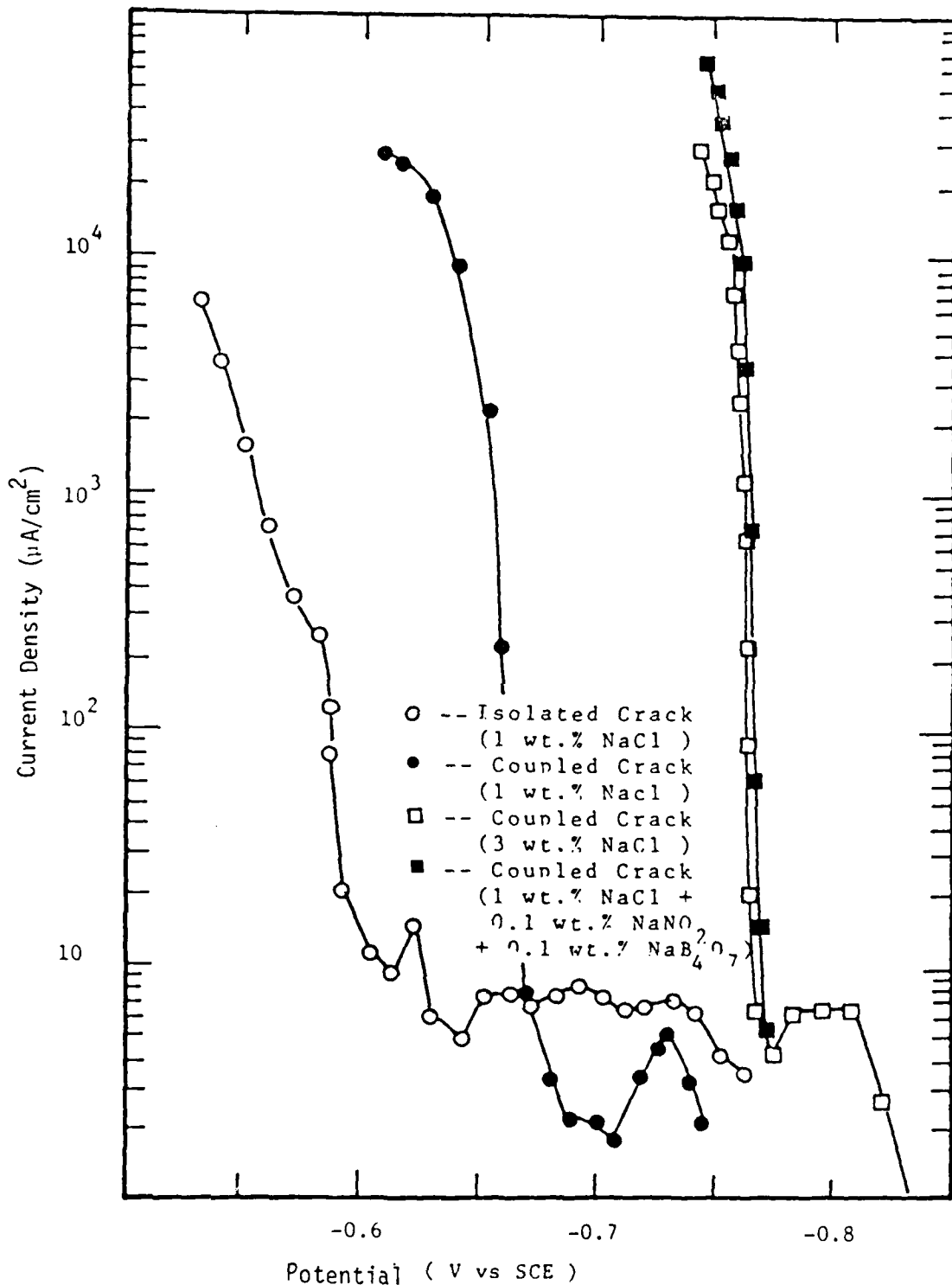
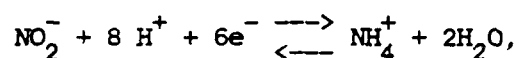


FIGURE 26. ANODIC POLARIZATION FOR VARIOUS CONDITION OF CREVICE
7075 T6 AL ALLOY IN DILUTE SOLUTION WITHOUT STIRRING
AT $20^\circ\text{C} \pm 2^\circ\text{C}$

the bare surface. Above this potential, the curves are linear with smooth slopes. The anodic profile for 3 wt.% NaCl solution shows that anodic dissolution inside the crack is higher than for 1 wt.% NaCl solution. At higher Cl^- ion concentration, gas formation and bubble formation are less than at the low Cl^- ion concentration inside the crack.

A thick adherent black film formed on the specimen surface. Figure 26, compares the anodic polarization curve for a coupled crack in the non-inhibitive solution with that for a coupled crack in an inhibitive solution. In the former case, the breakdown anodic dissolution potential is a little higher than that in the non-inhibitive solution. The nitrite ion effects a raising of the potential, that is,



$$E = + 0.90 \text{ V SHE.}$$

However, the current density is almost the same for both cases. From the experimental results, these concentrations of inhibitors may be a little more effective inside the crack, but, the inhibitive action is weak.

The time dependence of the open circuit corrosion potential of a coupled artificial crack immersed in aerated, unstirred 1 wt.% NaCl, was measured. The cracked 7075-T6 specimen and the external Al alloy were coupled for a few minutes, whereupon the corrosion potential of the external specimen shifted to the more noble direction compared with the bare surface specimen (uncoupled to other electrode), whereas the corrosion potential of the cracked specimen shifted to the more active direction compared with the

isolated specimen. After 6 hr, a steady-state condition was attained, at a potential difference of about 150 mV, which corresponds to Rosenfeld's data. Since this value is not small, an IR drop between the crack interior and outer electrode must be large.

Figure 27 shows the time dependence of potential difference between the crack interior and outer electrode, reaching steady-state condition after 6 hr. The electrode potential was measured as a function of time under the active state. After several hours, the potential differences were attained at a steady state condition of about 150 mV, i.e., the same value as that under the nonsteady-state conditions. Figure 28 shows the potential difference between the external specimen and the cracked specimen under the active state. According to Rosenfeld, the active state electrode potential of the crack was more negative than that of the open specimen because of a restricted oxygen supply to the crevices. This experimental data may show or prove Rosenfeld's experimental model.

McCafferty (79) and others (80), claim that a large potential difference exists between the crack interior and external metal, based on potential measurements of uncoupled, unpolarized components in solutions of differing oxygen content. Furthermore, the potential difference between the inner and outer surface is much larger before coupling than after. Our results do not agree: the potential difference between the inner and outer surface is larger after coupling than before, Figures 28, 29.

Thus, the potential difference changes slowly with distance from the crack tip, but to the mouth of the crack, the rate of change increases, i.e., inside the crack, the potential drop is very small. On the other hand, the potential drop between inside the crack and outside the crack is

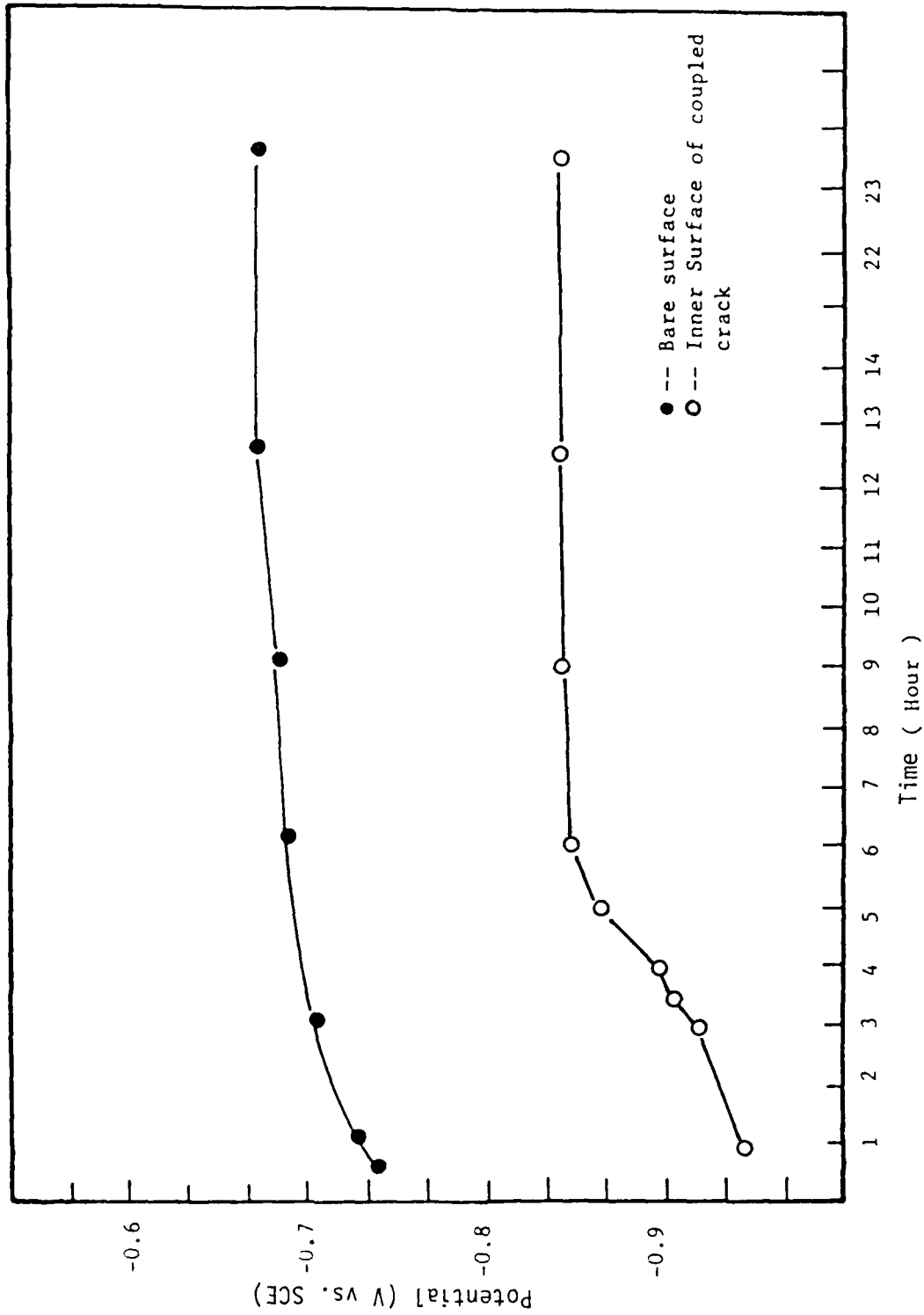


FIGURE 27. STEADY - STATE OPEN-CIRCUIT POTENTIAL FOR OPEN AND COUPLED CREVICE 7075 T6 ALLOY IN 1 wt.% NaCl SOLUTION WITHOUT STIRRING AT 20°C ± 2°C

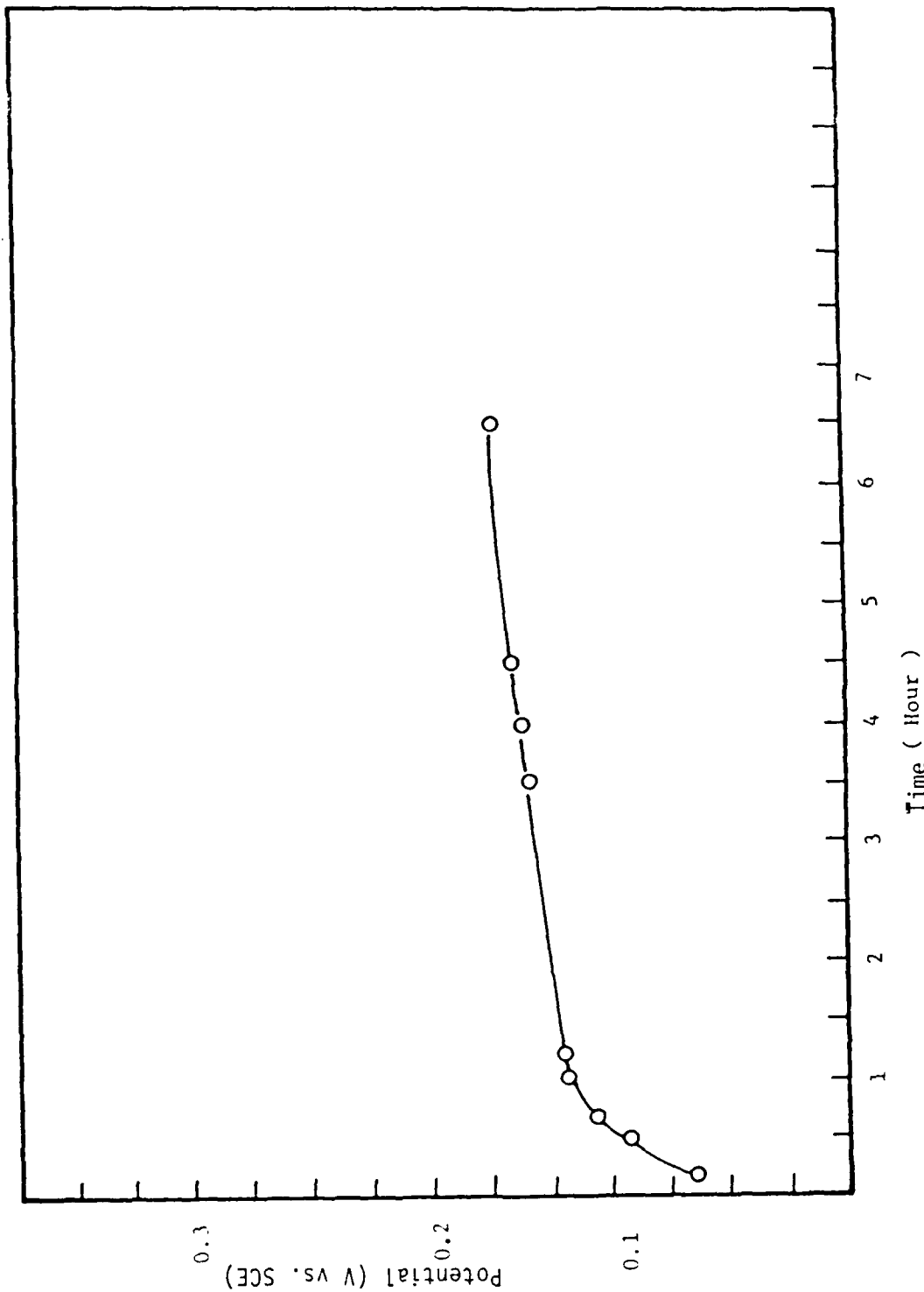


FIGURE 28. THE POTENTIAL DIFFERENCE FOR OPEN AND CREVICE T6 Al ALLOY UNDER ACTIVE STATE IN 1 wt.% NaCl SOLUTION.

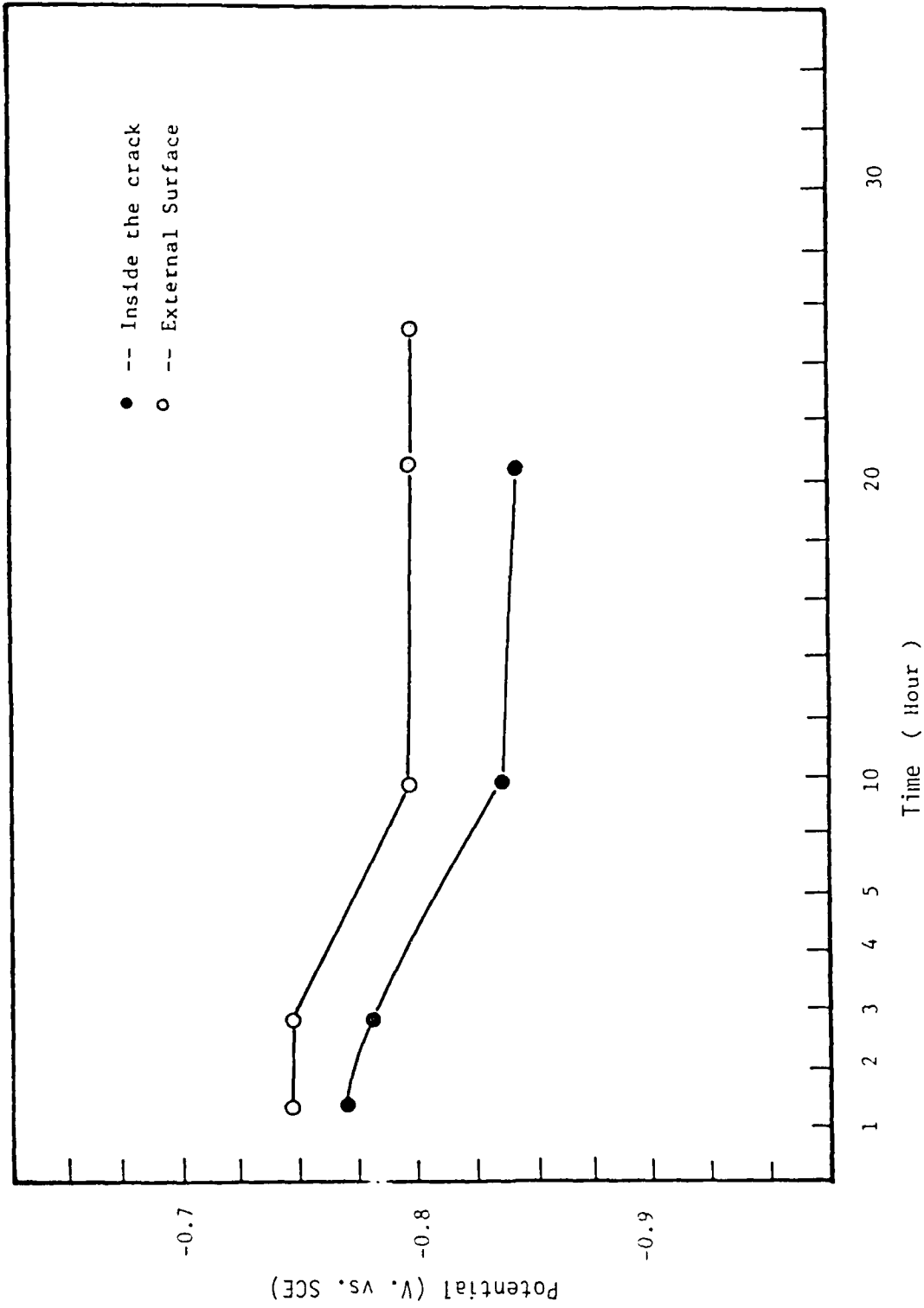


FIGURE 29. STEADY-STATE OPEN-CIRCUIT POTENTIAL UNDER STRESS IN 1 wt.% NaCl SOLUTION.

large, hence, the outside surface must support a cathodic reaction at a positive potential with respect to the anodic crack reaction, which suggests that metal inside the crack is isolated from the external surface reactions, i.e., the separation of the anodic and cathodic regions. According to this potential difference, the electrochemical driving force is not small and becomes more favorable for development of corrosion inside the crack. On the other hand, a small potential difference inside the crack may cause a large concentration change and a correspondingly large increase in current density at a given applied potential (81). In the open circuit condition, the outer surface cathodic reaction would occur if dissolved oxygen were the primary bulk oxidant. Coupled with a net anodic reaction inside the crack, for overall current balance would lead to steady state crevice corrosion. Applying a small positive or negative potential (under active state), bubble formation should occur both inside and on the outer surface of the sample, since it is thermodynamically possible.

3.1.3.4.3. Real Crack

Open circuit corrosion potential time dependence was measured for a real crack immersed in 1 wt.% NaCl aerated, unstirred solution with stress and without inhibitors. The potential inside the crack was measured using a special microcapillary tube; Fig. 30 shows the results. Corrosion potentials of both the external surface and inside the crack shifted to the more active direction under stress; a steady-state condition was attained after 20 hr. at a potential difference of about 35-45 mV. Because of this small value, the IR drop between the crack interior and outer surface must be small.

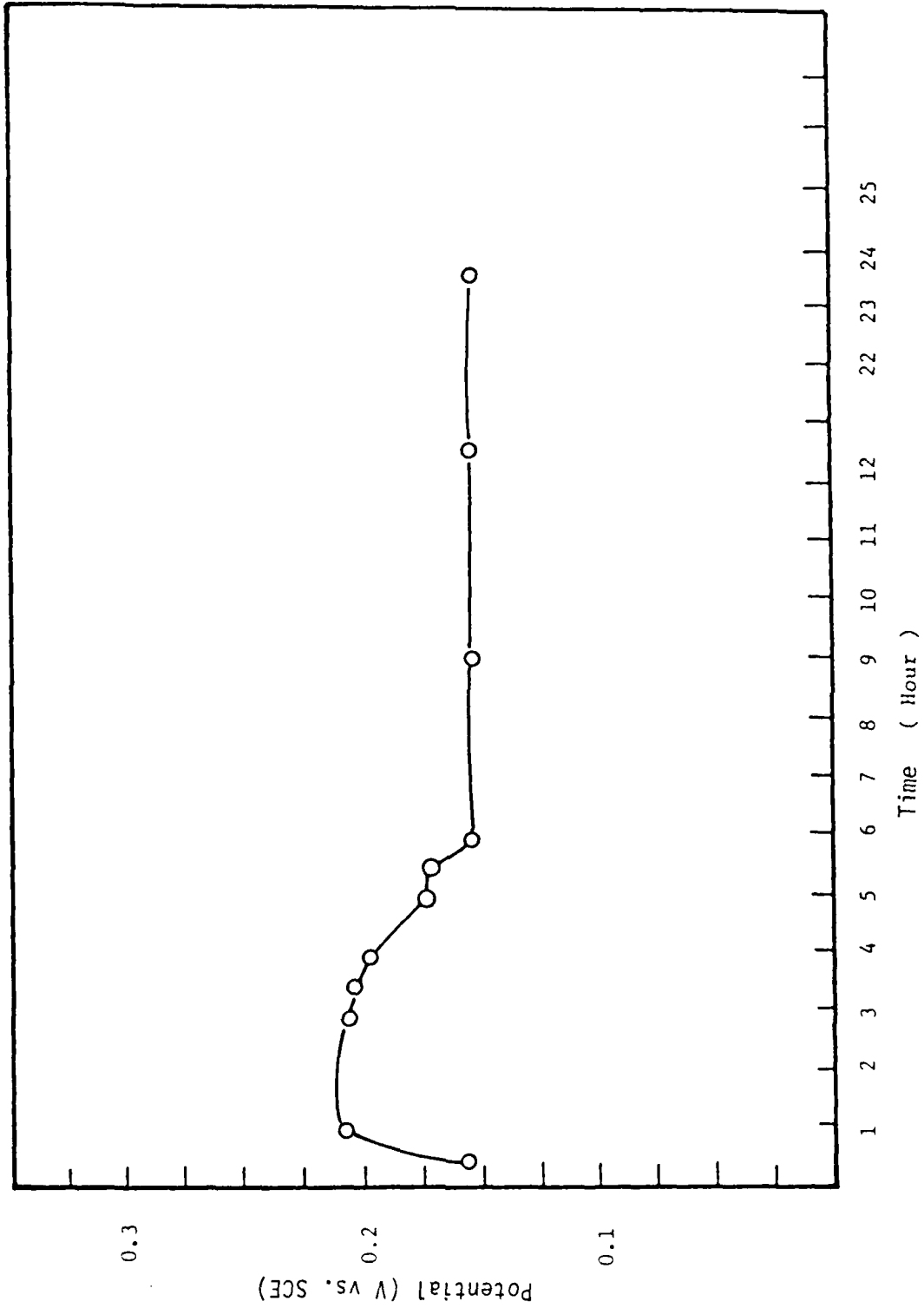


FIGURE 30. STEADY-STATE OPEN-CIRCUIT POTENTIAL DIFFERENCE FOR OPEN AND COUPLED CREVICE
7075 T6 AL ALLOY IN 1 wt.% NaCl SOLUTION

A schematic representation of crack velocities of aluminum alloys as a function of stress intensity typically yields a curve with three distinctive regions: Region I, where crack growth is initially observed and changes rapidly with stress intensity; Region II, the "plateau" region, which may be nearly parallel to the stress intensity axis; and a sharply increasing crack growth rate region (Region III) just prior to failure.

A stress intensity factor ($K_I = 12 \text{ Mpa}\sqrt{\text{m}}$), corresponding to Region II was used because in this region crack growth appears to be environmentally controlled and independent of K . Figure 31 shows the experimental result together with reference values. During crack propagation, the length of the crack can be measured in an optical microscope whenever necessary, then data for the da/dt vs. K_I plot can be obtained. The specimen was loaded using a torque wrench to a torque of 12.7 (N-m), with the equilibrium relationship expressed mathematically, (82)

$$T = G D P,$$

where, T is torque (N-m), D is the nominal bolt diameter (m), P is the induced force or clamp load (N), and is G an empirical constant, which takes into account friction and the variable diameter under the head and in the threads where friction is acting, yielding [Novak and Rolfe (83)]

$$K_I = 12 \text{ MPa}\sqrt{\text{m}}.$$

3.2 Stress/Strain Relations at a Corrosion Crack Tip.

Knowledge of the stress/strain relations at the tip of a corrosion (or fatigue) crack is necessary (but elusive) for a complete understanding of

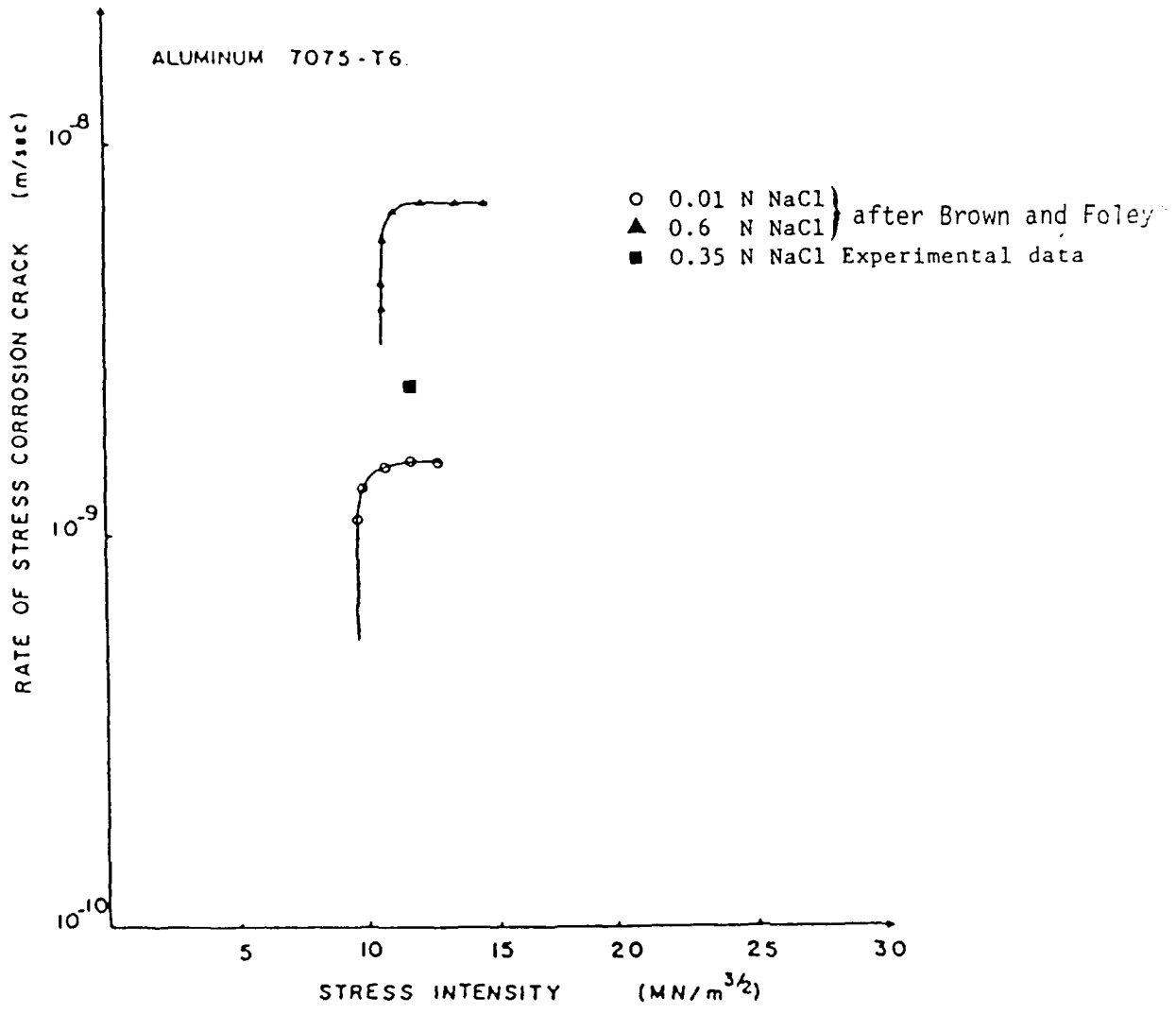


FIGURE 31. RATE OF CRACKING VERSUS STRESS INTENSITY FOR DILUTE NaCl SOLUTION

* B. F. Brown and R. T. Foley, CORROSION 36, 673 (1980)

SOC etc. Crack-tip corrosion rates and their relation to external chemistry and physical load configuration have been correlated, if not understood in terms of, the stress/strain relations at the crack tip, within a region of a few micrometers. (84-86)

Stress/strain relations within so small an area historically have eluded experimental measurement. Sharpe (87, 88), however, has developed an interferometric Strain Gage (ISG), at Michigan State University which, is capable of measuring specimen strain over a range as small as 25 micrometers (0.001 in.), and hence can determine biaxial strain within the critical zone of a crack tip. The actual gage consists of two shallow, pyramidal indentations impressed by a Vicker's microhardness machine into the specimen surface. The indentations are ca 25 μ m apart along a line normal to the crack propagation direction. Coherent radiation (from a He-Ne laser) reflected from the indentations produces two interference fringe patterns which move proportionally to the strain motion of the indentations. Movement of the interference fringes across photomultiplier tubes is measured and the relative displacement of the indentations, hence strain, is computed therefrom. Two photomultiplier tubes are used to remove rigid-body translations of the specimen in the strain direction.

3.3 Alternate Immersion Testing

A simple alternate immersion testing machine was constructed. This machine can provide variable, controlled immersion and drying time periods for as many as 100 specimens in up to 24 different liquid environments. A 10-minute immersion-50-minute drying cycle has been used in all tests to date, as recommended by ASTM G31-72.

Aluminum alloy 2024-T3 has been used for screening tests of various inhibitors and surfactant combinations. Test coupons were cut to 5.0 x 1.5 x 0.16 cm, polished and cleaned, weighed and suspended by glass hooks for the immersion testing. After exposure, coupons were cleaned, dried, reweighed, and evaluated for pitting damage. Weight-loss was converted to corrosion rate (ASTM G1-81).

The various inhibitor/surfactant materials used are listed in Table 4, and the results in Table 5. In general, these results agree with those of Khobaib (24, 25) and those listed elsewhere in this Report.

3.4 Corrosion Fatigue Inhibitor

Apparatus for studying CF inhibition using the methods described in Section 2.4. is available at MSU in Professor J. Martin's laboratory; it is heavily used, and would be available to this program only for limited time periods and for well-planned experiments. Preliminary experiments to develop appropriate test parameters must be performed on alternate equipment. The object of this phase, then, was the adaptation of equipment made available, but in a state of disrepair, and then to perform preliminary experiments along the line of, and to duplicate if possible, the work of Lynch and co-workers (26), cf. Fig. 31.

The apparatus currently consists of (Fig. 32)

MTS Model 206.11 - 11 kpsi hydraulic actuator

MTS Model 406 controller

MTS Model 436.11 control unit

Strain sert 25,000 lb. load cell

Table 4. Inhibitors used in Alternate Immersion Tests

<u>Substance</u>	<u>Chemical Formula</u>	<u>Source</u>
MacDill Formula	See Table 2.	Erny Supply Co. Tampa, FL
MBT	$C_7H_5NS_2$	Eastman Kodak Co. Rochester, NY
Boric Acid	H_3BO_3	Fisher Scientific Co. Fairlawn, NJ
Hamposyl L-30	$R-\overset{\overset{O}{\parallel}}{C}-\underset{\underset{CH_3}{ }}{N}-CH_2COOH$ R=fatty acid hydrocarbon chain	W.R. Grace & Co. Nashua, NH
Lathanol LAL	$CH_3(CH_2)_{10}CH_2-\overset{\overset{O}{\parallel}}{C}-SO_3Na$	Stepan Chemical Co. Northfield, IL
N-Ethylpiperidine	$C_7H_{15}N$	Reilly Chemical Co. Indianapolis, IN
1,3-(Di-4 Piperidyl) Propane	$C_{13}H_{26}N_2$	Reilly Chemical Co. Indianapolis, IN
Piperizine	$C_5H_{11}N$	Sigma Chemical Co. St. Louis, MO
Polystep B-12	$CH_3CH_2O(CH_2CH_2O)_3(CH_2)_{11}CH_2OS_3Na$	Stepan Chemical Co. Northfield, IL
Sodium Borate	$Na_2B_4O_7 \cdot 10H_2O$	Mallinckrodt, Inc. Paris, KY
Sodium Nitrite	$NaNO_2$	Mallinckrodt, Inc. Paris, KY
Stepantan A	$C_6H_{11}COOSO_3Na$	Stepan Chemical Co. Northfield, IL
Zonyl FSA	$RCH_2CH_2SCH_2CH_2CO_2Li$	E.I. Du Pont De Nemours & Co. Wilmington, DE
Zonyl FSC	$RCH_2CH_2SCH_2CH_2\overset{\oplus}{N}(CH_3)_3CH_3\overset{\ominus}{SO}_4$	E.I. Du Pont De Nemours & Co. Wilmington, DE
Zonyl FSP	$(RCH_2CH_2O)_{1,2}P(O)(ONH_4)_{2,1}$	E.I. Du Pont De Nemours & Co. Wilmington, DE

Table 5. Alternate Immersion Test Results

No.	Electrolyte	Surface Area (cm ²)	Surface Appearance	Weight Loss (gm)	Corrosion Rate (mpy)	Remarks
1	Distilled Water	16.823	Surface looks as original	<0.0001	<0.02	Negligible effect
2	0.1 Wt% NaCl	16.720	Entire surface attacked, several Pits	0.0022	0.49	Should be inhibited
3	0.1M NaCl	16.975	Entire surface attacked, covered with pits	0.0203	4.43	Should be inhibited
4	MacDill Formula (1.3 Wt%)	16.804	Surface looks as original	0.0001	0.02	Very good
5	1.3 Wt% MacDill 0.1 Wt% NaCl	16.808	Surface looks as original	0.0001	0.02	Very good
6	10 ppm MBT	16.736	Surface looks as original	<0.0001	<0.02	Very good
7	10 ppm MBT 0.1 Wt% NaCl	16.886	Surface looks as original	<0.0001	<0.02	Very good
8	100 ppm 1,1,1-trichloroethane	17.166	Surface looks as original	<0.0001	<0.02	Negligible effect

Table 5. (continued)

No.	Electrolyte	Surface Area (cm ²)	Surface Appearance	Weight Loss (gm)	Corrosion Rate (mpy)	Remarks
9	100 ppm 1,1,1-trichloroethane 0.1 Wt% NaCl	16.886	Entire surface attacked, several pits	0.0037	0.81	Should be inhibited
10	0.061 Wt% S. Nitrite 0.1 Wt% NaCl	15.706	Some light oxide patches, several pits	0.0012	0.28	Poor
11	0.198 Wt% S. Borate 0.061 Wt% S. Nitrite	16.517	Entire surface dark, several shallow pits	0.0015	0.34	Poor
12	0.198 Wt% S. Borate 0.061 Wt% S. Nitrite 0.01 Wt% NaCl	16.872	Entire surface dark, several shallow pits	0.0030	0.66	Very poor
13	0.198 Wt% S. Borate 0.061 Wt% S. Nitrite 10 ppm MBT 0.1 Wt% NaCl	15.953	Entire surface dark	0.0026	0.60	Very poor
14	0.198 Wt% S. Borate 0.061 Wt% S. Nitrite 100 ppm Lath-anol LAL	16.814	Oxide over entire surface, many shades	0.0015	0.33	Poor

Table 5. (continued)

No.	Electrolyte	Surface Area (cm ²)	Surface Appearance	Weight Loss (gm)	Corrosion Rate (mpy)	Remarks
15	0.198 Wt% S. Borate 0.061 Wt% S. Nitrite 100 ppm Lathanol LAL 0.1 Wt% NaCl	16.559	Entire surface dark, pits all over	0.0070	1.57	Very very poor
16	0.198 Wt% S. Borate 0.061 Wt% S. Nitrite 100 ppm Zonyl FSP	16.905	Light oxide over most of surface	< 0.0001	< 0.02	Good
17	0.198 Wt% S. Borate 0.061 Wt% S. Nitrite 100 ppm Zonyl FSP 0.1 Wt% NaCl	16.559	Some oxide patches	0.0003	0.07	Good
18	0.198 Wt% S. Borate 0.061 Wt% S. Nitrite 100 ppm Zonyl FSA 0.1 Wt% NaCl	16.808	Light oxide film entire surface,	0.0003	0.07	Good
19	0.198 Wt% Boric Acid 0.061 Wt% S. Nitrite	16.823	Surface looks as original	< 0.0001	< 0.02	Very Good
20	0.198 Wt% Boric Acid 0.061 Wt% S. Nitrite 0.1 Wt% NaCl	16.958	Scattered pits over surface, mostly at hole	0.0010	0.22	Poor
21	0.198 Wt% Boric Acid 0.061 Wt% S. Nitrite 10 ppm MBT 0.1 Wt% NaCl	16.475	Surface looks as original	0.0001	0.02	Very good

Table 5. (continued)

No.	Electrolyte	Surface Area (cm ²)	Surface Appearance	Weight Loss (gm)	Corrosion Rate (mpy)	Remarks
22	0.198 Wt% Boric Acid 0.061 Wt% S. Nitrite 100 ppm Lathanol LAL	16.911	Surface looks as original	< 0.0001	< 0.02	Very good
23	0.198 Wt% Boric Acid 0.061 Wt% S. Nitrite 100 ppm Lathanol LAL 0.1 Wt% NaCl	16.491	Entire surface attacked, several pit clusters	0.0028	0.63	Very poor
24	0.198 Wt% Boric Acid 0.061 Wt% S. Nitrite 100 ppm Zonyl FSP	16.703	Surface looks as original	0.0001	0.02	Very good
25	0.198 Wt% Boric Acid 0.061 Wt% S. Nitrite 100 ppm Zonyl FSP 0.1 Wt% NaCl	16.459	A few pits	0.0004	0.09	Good
26	100 ppm Zonyl FSC	16.720	Surface looks as original	0.0002	0.04	Good
27	100 ppm Zonyl FSC 0.1 Wt% NaCl	17.008	Entire surface attacked, pits all over running in streaks	0.0030	0.65	Very poor
28	100 ppm Zonyl FSC 50 ppm 1,1,1-Trichloroethane 0.1 Wt% NaCl	16.217	Entire surface attacked, pits all over running in streaks	0.0022	0.50	Poor to very poor

Table 5. (continued)

No.	Electrolyte	Surface Area (cm ²)	Surface Appearance	Weight Loss (gm)	Corrosion Rate (mpy)	Remarks
29	100 ppm Zonyl FSC 10 ppm MBT 0.1 wt% NaCl	16.446	Surface looks as original	0.0002	0.05	Good
30	100 ppm Stepantan A	17.043	Surface look as original	0.0002	0.04	Good
31	100 ppm Stepantan A 0.1 wt% NaCl	16.738	Entire surface attacked, small pits covering surface	0.0012	0.27	Poor
32	100 ppm Stepantan A 50 ppm 1,1,1-Tri-chloroethane 0.1 wt% NaCl	16.907	Entire surface attacked, small pits covering surface	0.0009	0.20	Poor
33	100 ppm Stepantan A 10 ppm MBT 0.1 wt% NaCl	16.543	Surface looks as original	0.0003	0.07	Good
34	100 ppm Hamposyl L-30	16.785	Surface looks as original	0.0003	0.07	Good
35	100 ppm Hamposyl L-30 0.1 wt% NaCl	16.649	Entire surface attacked, several small pits	0.0013	0.29	Poor

Table 5. (continued)

No.	Electrolyte	Surface Area (cm ²)	Surface Appearance	Weight Loss (gm)	Corrosion Rate (mpy)	Remarks
36	100 ppm Hamposyl L-30 50 ppm 1,1,1-Tri- chloroethane 0.1 Wt% NaCl	16.304	Entire surface attacked, several small pits	0.0013	0.30	Poor
37	100ppm Hamposyl L-30 10 ppm MBT 0.1 Wt% NaCl	16.495	Surface looks as original	0.0002	0.04	Good
38	100 ppm Polystep B-12	17.178	Surface looks as original	0.0002	0.04	Good
39	100 ppm Polystep B-12 0.1 Wt% NaCl	16.717	Entire surface attacked, several pits	0.0029	0.64	Very poor
40	100 ppm Polystep B-12 50 ppm 1,1,1-Tri- chloroethane 0.1 Wt% NaCl	17.215	Entire surface attacked, several pits	0.0027	0.58	Very poor
41	100 ppm Polystep B-12 10 ppm MBT 0.1 Wt% NaCl	16.511	Surface looks as original	0.0001	0.02	Very good
42	100 ppm Piperazine	17.062	Very light oxide tint	6.0001	0.02	Very good

AD-A166 317

INHIBITING CORROSION CRACKING: CRACK TIP CHEMISTRY AND
PHYSICS(U) MICHIGAN STATE UNIV EAST LANSING DEPT OF
METALLURGY MECHANICS AND MATERIALS SCIENCE R SUMMITT

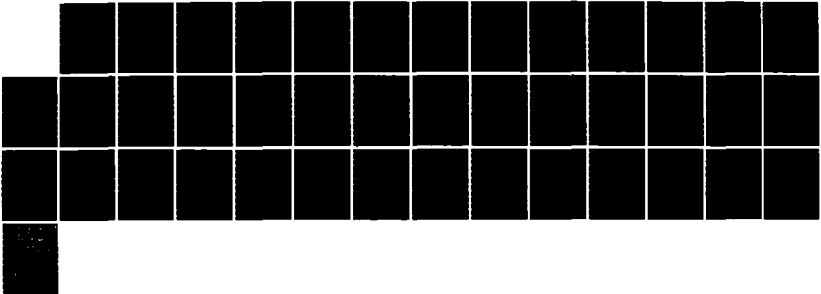
2/2

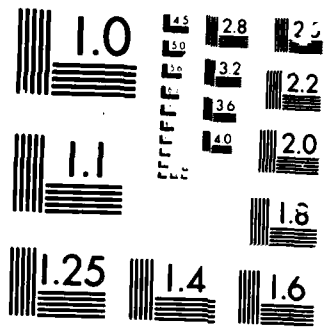
UNCLASSIFIED

14 MAR 86 N00014-84-K-0419

F/G 11/6

NL





MICROCOPY RESOLUTION TEST CHART

Table 5. (continued)

No.	Electrolyte	Surface Area (cm ²)	Surface Appearance	Weight Loss (gm)	Corrosion Rate (mpy)	Remarks
43	100 ppm Piperazine 0.1 wt% NaCl	16.804	Entire surface attacked, extreme pitting	0.0100	2.21	Very very poor
44	100 ppm Piperazine 50 ppm 1,1,1-Tri- chloroethane 0.1 wt% NaCl	16.940	Entire surface attacked, extreme pitting	0.0105	2.30	Very very poor
45	100 ppm Piperazine 10 ppm MBT 0.1 wt% NaCl	16.491	Light oxide tint	0.0006	0.13	Poor
46	100 ppm 1,3-(Di-4- Piperidyl) Propane	16.962	Entire surface dark	0.0012	0.26	Poor
47	100 ppm 1,3-(Di-4- Piperidyl) Propane 0.1 wt% NaCl	16.991	Entire surface dark and patchy	0.0060	1.31	Very poor
48	100 ppm 1,3-(Di-4- Piperidyl) Propane 50 ppm 1,1,1-Tri- chloroethane 0.1 wt% NaCl	17.008	Entire surface dark and patchy	0.0071	1.55	Very poor

Table 5. (continued)

<u>No.</u>	<u>Electrolyte</u>	<u>Surface Area (cm²)</u>	<u>Surface Appearance</u>	<u>Weight Loss (gm)</u>	<u>Corrosion Rate (mpy)</u>	<u>Remarks</u>
49	100 ppm 1,3-(Di-4-Piperidyl) Propane 10 ppm MBT 0.1 Wt% NaCl	16.520	Entire surface dark and patchy	0.0013	0.29	Poor
50	100 ppm N-Ethyl-piperidine 0.1 Wt% NaCl	17.010	Entire surface dark, many pits	0.0053	1.16	Very very poor
51	100 ppm N-Ethyl-piperidine 10 ppm MBT 0.1 Wt% NaCl	16.643	Entire surface dark and patchy	0.0011	0.25	Poor

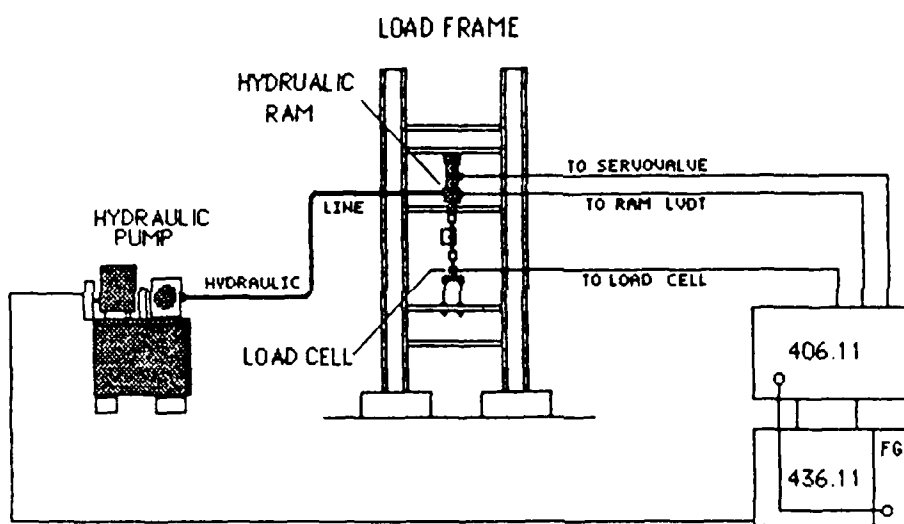


Figure 32. Electrohydraulic apparatus for corrosion fatigue.

MTS Hydraulic pump.

The system is operated under load control, with a 2 hz. sine waveform in tension-tension loading. Stainless steel grips for compact tension specimens were machined to fit the MTS equipment. Compact tension specimens were precracked in the machine, and crack propagation was measured with a converted cathetometer.

Aqueous solutions of corrosion accelerant/inhibitor were introduced into the crack from a 1.5-in length of 0.75-in polystyrene tube, cemented to the sample face, and closed at the other end with a cemented polystyrene sheet, using a silicone sealant. A side-tube covered with a silicone syringe port provided means for introducing solutions to the crack (Figure 33).

Specimens were cleaned, mounted in the apparatus, and then subjected to fatigue loading according to ASTM 399-A2.1 to produce the 0.1 in. precrack. Loading conditions then were changed to correspond to Region II (Figure 34), and distilled water introduced to the crack. When sufficient measurements had been made, inhibitor solution was added at double concentration, to allow for dilution. The inhibitor formula of Table 3 was used.

Only three experiments have been performed to date, with equivocal results (Figure 35). In each, reduction of crack growth rate is apparently observed, but the visual method of data recording and a small difference in specimen geometry may be the causes of substantial scatter in the data. Scanning electron microscopic examination of fractured surfaces, however, revealed distinct differences in the fatigue crack growth regions before and after the addition of inhibitor solution.

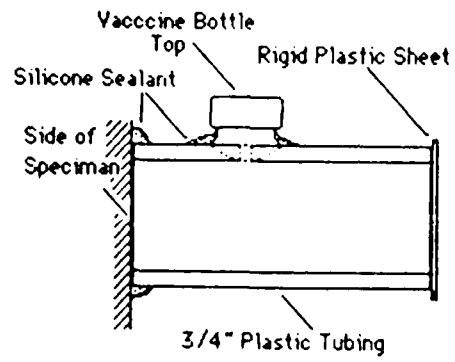


Figure 33. Method for introducing accelerant/inhibitor solutions to crack tip.

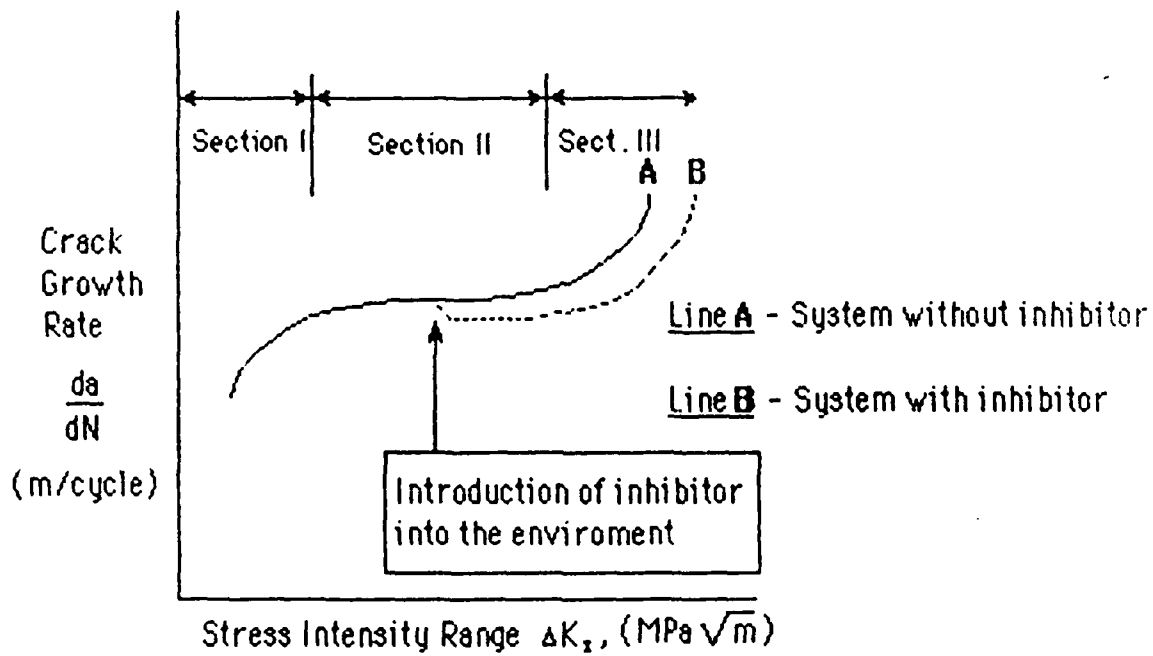


Figure 34. The effect on growth rate of adding inhibitor to a propagating corrosion fatigue crack, schematic (26).

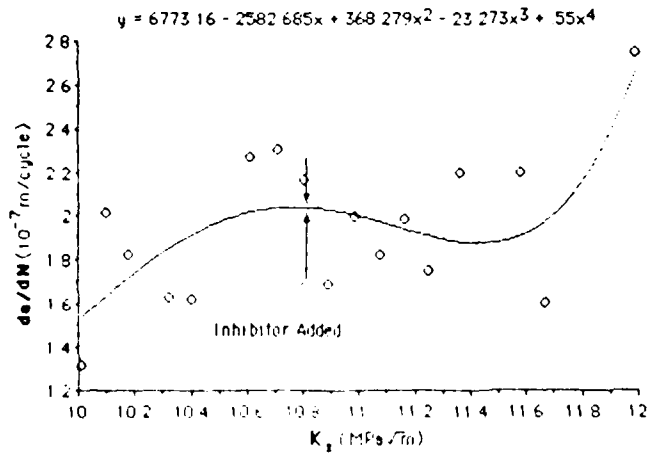
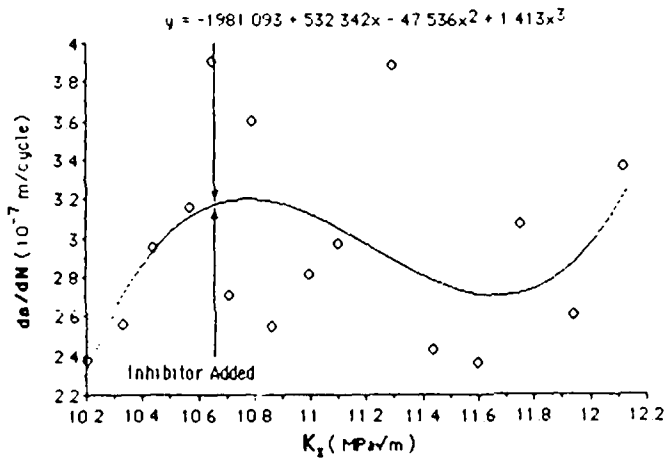
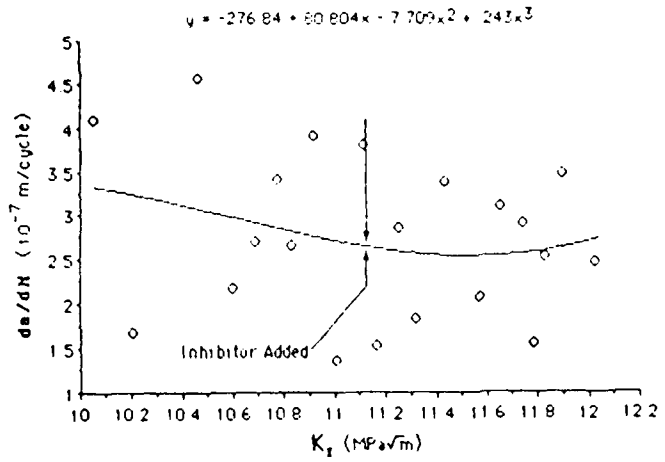


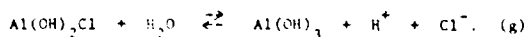
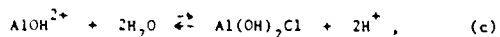
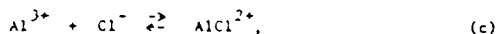
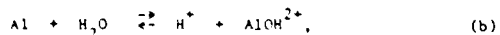
Figure 35. Corrosion fatigue crack growth rate of 7075-T651 Al alloy in 1 wt% NaCl solution; effect of inhibitor addition.

4. Discussion

4.1 Bare Surface Corrosion

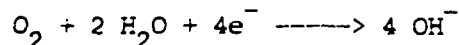
Polarization profiles in Figure 9 show that the bare surface dissolution rate is dependent on chloride content, hence the reaction involves chloride anion complexes. Corrosion of Al and 7075-T6 Al alloy at the bare surface in solutions containing dilute NaCl is accompanied by the consumption of hydrogen, oxide, chloride, and sodium ions.

The most probable reaction mechanism accompanying the initial stage of the corrosion process of 77075-T6 Al alloys in NaCl is (20);



It is believed (20, 89), that the hydrated aluminum ion, $\text{Al}(\text{H}_2\text{O})^{+3}$, is formed rapidly (about 1 sec), and then undergoes a very fast hydrolysis, (b). Later, both the Al^{3+} and Al(OH)^{2+} ion react with Cl^{-} ions, i.e., Eqs. (c) and (e); reaction (e) is faster, however, than (d). From our experimental results, it appears that both reactions (c) and (e) may take place as an anodic dissolution.

On the other hand, the overall cathodic reaction in near-neutral solutions, based the results, is oxygen reduction,



From Figs. 3 and 4, the limiting current density (i_L) is $10 \mu\text{A}/\text{cm}^2$ for both 1 wt.% and 3 wt.% NaCl. Oxygen is relatively insoluble in NaCl solution at room temperature, hence there is a small limiting current density for the cathodic reduction of oxygen.

In Fig. 21, the applied stress affects the polarization behavior of Al 7075-T6 and raises the current density. Stress corrosion cracking of the 7075-T6 aluminum alloys in chloride ion is because of the formation and growth of cracks of an almost brittle nature, which propagate along the grain boundaries. A number of mechanisms have been proposed (39, 90, 91) to account for the phenomenon; three of them have received wide attention, *viz.* film rupture (93, 94) pre-existing active, (94) and hydrogen embrittlement (90, 91).

In the pre-existing path model, emphasis is placed on the microstructural and electrochemical parameters. Chemical inhomogeneities in the material are considered to be the key factor. An example often quoted is the segregation of alloying elements in the form of precipitates at grain boundaries in 7075-T6, creating a precipitate-free zone in the adjacent material. In a corrosive environment, a localized electrochemical reaction can be established between the precipitates and adjacent material. Although this is an adequate explanation for intergranular corrosion, it does not account for the role of tensile stresses in producing SCC.

According to the film rupture model, tensile stress ruptures a passivating oxide film, exposing fresh metal with electrochemical potentials

quite different from the surrounding still protected areas. Thus corrosion is thought to occur at these sites until a new passivating oxide film can reform, which in turn will be ruptured, and the corrosion repassivation processes repeated, thereby generating an active path for SCC. In this mechanism, the rate of repassivation is the key factor; if rapid, insufficient corrosion will occur to promote SCC.

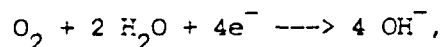
The mechanism of hydrogen embrittlement involves diffusion of water molecules or hydrogen ions down the crack, reduction to adsorbed hydrogen atoms at the crack-tip, surface diffusion of adsorbed atoms to a preferred surface site, absorption of the adatoms into the metal matrix, followed by diffusion of hydrogen atoms to a position in front of the crack-tip. If hydrogen indeed is the basis of embrittlement during SCC, the kinetics still may be influenced, if not controlled, by hydrogen permeation or stress induced rupture of an oxide film.

The possible crack-advancement mechanisms, i.e., dissolution and hydrogen ion reduction, will be controlled at a given potential by three subsidiary factors: oxide rupture rate, solution-renewal rate, and passivation rate, including repassivation rate. In these experiments, it appears that passivation rate at the stress concentration region, which is common to both mechanisms, i.e., film rupture (activation control) and hydrogen-embrittlement (diffusion control), is the rate-controlling reaction.

4.2. Crack Electrochemistry

As noted in our polarization curves (Figures 24, 26 and 27), hydrogen gas formation and bubbling occurred near the corrosion potential region.

Thus, two cathodic reactions may be considered, i.e., reduction of oxygen and hydrogen,



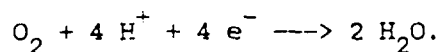
If both cathodic reactions take place, depolarization might occur, increasing the corrosion rate.

Figure 24 shows that polarization profiles inside an isolated crack differ from the bare surface. Furthermore, the pH inside the crack also is different from the external surface. In the case of the bare surface, no hydrogen gas bubbling was observed. These results confirm that the crack tip electrochemical environment is different from the bulk exterior environment, and alternative electrochemical reactions may occur there.

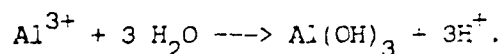
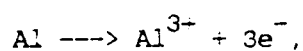
Figure 24 shows that 0.1 wt.% NaNO_2 + 0.1 wt.% $\text{Na}_2\text{B}_4\text{O}_7$ inhibitors may affect chloride attack inside the crack, although Figure 14 shows only a small effect by these inhibitors. This is because of the establishment of a special, more complex microchemical or electrochemical environment within the crack which is different from the bulk exterior environment. Although localized corrosion is complex and involves many simultaneous processes, there are several possible explanations. If because of migration, chloride accumulated within the crevice and hydrogen removal are significant factors, then the rate would be expected to depend on Cl^- and H^+ concentrations.

In the case of a coupled crack, Figures 30 and 31 show that the cathodic reaction (probably oxygen reduction and hydrogen reduction) takes place outside the crack, while a small anodic reaction and hydrogen reduction occur inside the crack. Figure 31 also shows that the anodic profile of an isolated crack is different from the profile of a coupled crack. The evidence of a different corrosion potential, the active potential and the anodic profiles probably result from the hydrogen evolution reaction. This cathodic reduction may control this corrosion mechanism or suppress the anodic dissolution.

According to Pourbaix (77), the surfaces which are outside the crack and are in direct contact with NaCl solution, are often passivated by oxygen, and are acting as aerated cathodes where oxygen is being reduced to water, for example,

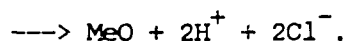
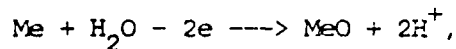


Surfaces inside the crack are active and behave as non-aerated anodes, where the metal undergoes corrosion and hydrolyzes with a decrease of pH, e.g.,



Experimentally, a decrease of pH inside the coupled crack is found, indicating weak acidity inside the crack.

Rosenfeld (96) shows a general mechanism for a real crack involving the effects of chloride ion and acidity,



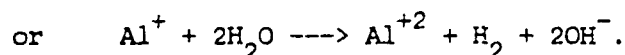
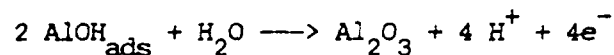
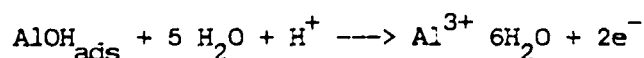
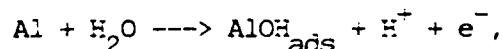
Our results show that hydrogen evolution and oxygen reduction (secondary) take place cathodically, and anodic dissolution may take place (anodic condition).

Pickering and Frankenthal (66) showed that large potential drops attributed to constrictions are caused by trapped hydrogen gas bubbles. The following two cathodic processes can be considered: (1) Hydrogen evolution, and (2) ionization of oxygen. These may proceed by independent parallel stages and are related to one another only as they provide an overall electrochemical potential on the corroding surface. Hydrogen evolution may have an important role, however, as the controlling cathodic process.

Hydrogen evolution possesses high diffusion mobility and a high rate of migration in an electric field. An increase in the hydrogen evolution rate and bubble formation will decrease the thickness of the diffusion layer of

liquid adjacent to the surface of the metal because of the additional mixing, hence, the limiting diffusion current for oxygen reduction also will increase (Eq. 34). Hydrogen bubbles on the surface may decrease oxygen diffusion, either as a result of smaller electrolyte cross section, or by entrapment removal of oxygen from the surface with hydrogen bubbles. In our experimental results, the principal effect of hydrogen evolution on the limiting diffusion current density for oxygen is thought to consist of a reduction of the diffusion layer thickness as a result of agitation by hydrogen evolution.

Uhlig (97) suggested the importance of hydrogen evolution in a different role as a controlling factor. When aluminum dissolves anodically, both Al^{+3} and Al^+ are formed, initially the univalent ion, which then reduces water to form the trivalent ion.



During formation of a surface oxide film, hydrogen evolution takes place simultaneously at the anode as well as at the cathode. In the anodic dissolution, hydrogen evolution is responsible for increased local corrosion action. Many actions of hydrogen as well as migration are probably

responsible for the potential drop as well as separation of the anodic and cathodic sites.

Another experimental result for an isolated crack, shows that current density is independent of Cl^- concentration, i.e., the corrosion rate inside the crack is controlled by a cathodic process.

4.3. Extending Mathematical Models

Numerous models have been proposed for crevice corrosion, corrosion cracking, etc., (73, 98, 99) which yield distributions of current, voltage, and composition in the crevice and nearby regions. The approach shows promise in predicting crevice gap/depth ratios that are critical for localized attack. Porous electrode theory (100) also can be used to predict the depth at which the anodic reaction may be driven by external cathodic current. Ohmic drop restricts current penetration into a small-gap, occluded region. At greater depths in the gap, the metal is isolated from the external surface reactions. Newman (101) calculated the depth to which a reaction may penetrate the walls of pipe. Turnbull (75) showed improved mathematical modelling of mass transport of oxygen in a crevice or crack for an estimation of the oxygen concentration. Diffusion and acid hydrolysis were included in a model for crevice corrosion by Galvele (102). A sophisticated model for stress corrosion cracking of titanium was developed by Beck (63); transport limitations, wall reactions and nonlinear kinetics were included in the model. Alkire and Hebert's (103) improved model for corrosion initiation of pure aluminum accounts for electrode reactions of aluminum, oxygen and hydronium ion, and for transport by unsteady state diffusion and migration.

We have found that hydrogen evolution occurs both cathodically and anodically, although the reaction is a cathodic process. The electrode potential of the metal inside the crack is lower than the hydrogen equilibrium potential in the relevant solution. The anodic corrosion reaction is not the only possible one; a cathodic evolution of hydrogen, $2\text{H}^+ + 2\text{e}^- \rightarrow \text{H}_2$, also may occur inside the crack under the anodic condition. Our results show that near the corrosion potential, only cathodic evolution of hydrogen takes place and hinders anodic dissolution so that Pickering and Ateya's (99) model may be useful to describe mass transfer in the electrolyte by molecular diffusion and ionic migration according to the Nerst-Einstein relation.

According to Pickering and Ateya,

$$J_{\text{H}^+} = -D_{\text{H}^+} \left(\frac{dC_{\text{H}^+}}{dx} + C_{\text{H}^+} \frac{F}{RT} \frac{d\phi}{dx} \right) = \frac{i}{F}, \quad (1)$$

$$J_{\text{Cl}^-} = -D_{\text{Cl}^-} \left(\frac{dC_{\text{Cl}^-}}{dx} - C_{\text{Cl}^-} \frac{F}{RT} \frac{d\phi}{dx} \right) = 0, \quad (2)$$

where D_{H^+} is H^+ diffusivity, D_{Cl^-} is Cl^- diffusivity, C_i are concentrations, ϕ is local electrical potential in the crack, and i is the local current density of the hydrogen evolution; T is absolute temperature, F is Faraday constant, and R is the gas constant. The equation of electroneutrality is

$$\sum z_i C_i = 0, \quad (3)$$

$$\text{i.e.,} \quad C_{\text{H}^+} = C_{\text{Cl}^-} = C. \quad (4)$$

Our results show, that after a few hours, the potential and current reach steady-steady values. According to Pickering,

$$C = C_o \exp \left(\frac{F \phi}{R T} \right). \quad (5)$$

Modifying Eq. (6), by Eq. (5) and substituting in Equation (4) gives

$$J_{h^+} = - 2 D_{H^+} C_o \frac{F}{R T} \frac{d \phi}{d x} \exp \left(\frac{F \phi}{R T} \right). \quad (6)$$

Pickering derived

$$\phi = \frac{R T}{F} \ln \frac{\cosh \left[\frac{(L - x) / X}{L / X} \right]}{\cosh \left[\frac{L / X}{L / X} \right]}, \quad (7)$$

where

$$X = (D_{H^+} C_o F a / i_s),$$

$$i_s = i_o \exp \left(\frac{\beta F}{R T} \phi \right), \text{ or } i - i_s \left(\frac{C}{C_o} \right) \exp \left(\frac{\beta F \phi}{R T} \right);$$

β is the transfer coefficient of hydrogen evolution, and ϕ is the local electrical potential in the crack and solution. In Fig. 29 are shown results of the open circuit corrosion potential vs time inside the real crack; the potential difference from the outer surface is about 40 mV. The potential difference ϕ within the crack can be calculated from

$$\phi = \frac{R T}{F} \ln \frac{\cosh \left[\frac{(L - x) / X}{L / X} \right]}{\cosh \left[\frac{L / X}{L / X} \right]}. \quad (8)$$

Values for the relevant parameters are: $X = (D_H + C_O F a / i_s)$, $D_H = 5 \times 10^{-5} \text{ cm}^2 \text{ sec}$, $\frac{RT}{F} = 25 \text{ mV}$. The crack length (L) is 1 cm, and crack width (a) is 0.01 cm. $C_O = 0.17 \text{ mole/l}$, $F = 96500 \text{ c/mole}$, i_s can be obtained from experimental results (Figs. 21 and 22). From Fig. 21,

$$i_s = 20 \text{ A/cm}^2 = 20 \times 10^{-6} \text{ A/cm}^2,$$

$$X = (D_H + C_O F a / i_s) = 0.64$$

Thus, the potential

$$\phi = \frac{RT}{F} \ln \frac{\cosh \left[\frac{(L-x)/X}{(L/x)} \right]}{\cosh \left[\frac{(L-x)/X}{(L/x)} \right]} = 18 \text{ mV},$$

in fair agreement with the experimental value.

Another model by Doig and Flewitt (61) and Melville (57, 58), shows that, when stress corrosion cracks grow by enhanced anodic dissolution and are subjected to external polarization, an electrode potential distribution is established within the crack. A crack diagram of width w , length x , and width y , is shown in Fig. 36. The width y is very much greater than width w , so the crack may be considered to be of infinite length.

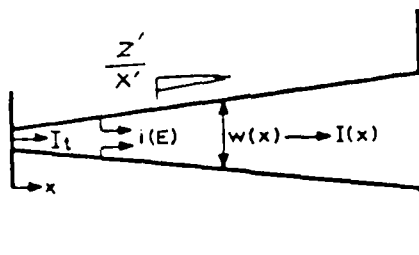


Fig 36 Schematic representation of the crack

However, $\frac{Z}{H} \ll 0$ so it may be assumed that the effect of crack width

variation may be neglected. Fig. 37 shows the Evans polarization diagram.

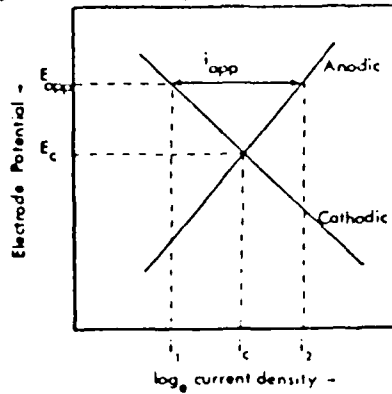


Figure 37. Schematic Polarization Diagram of the Electrochemical Reactions Occurring at the Specimen Surface Showing the Influence of Potentiostatic Polarization

E_c is the external surface corrosion potential, i is the corrosion current density at potential E_c , and E_x is the potential at position x within a crack (V). According to Doig and Flewitt (59), the net anodic i_{app} at E_{app} is given by

$$i_{app} = i_c \left[\exp \left(\frac{E_{app} - E_c}{\alpha} \right) - \exp \left(\frac{E_{app} - E_c}{-\beta} \right) \right]. \quad (9)$$

More generally, the net current density, i_x , at any potential E_x is given by

$$i_x = i_c \left[\exp \left(\frac{E_x - E_c}{\alpha} \right) - \exp \left(\frac{E_x - E_c}{-\beta} \right) \right]. \quad (10)$$

According to Doig and Flewitt, the net anodic current flow within the crack at a distance x from the free surface is the integrated sum of the net anodic current generated on the crack surface at distance greater than x ,

$$\frac{d i_f}{d x} = 2 i_x, \quad (11)$$

and

$$i_f = - w c \left(\frac{d E_x}{d x} \right). \quad (12)$$

Consequently, from Eq. (12) and the differential Eq. (13), we obtain

$$\frac{d^2 E_x}{d x^2} = \frac{- 2 i c}{X c} \left[\exp \left(\frac{E_x - E_c}{a} \right) - \exp \left(\frac{E_x - E_c}{-\beta} \right) \right] \quad (13)$$

In order to apply this model to real experimental conditions, it was modified, following Melville's (57, 58), reasoning. The potential variation is described under more general conditions: If $E(x)$ is the specimen potential relative to the solution at position X in the crack, there is a change dI in the current down the crack over length dx ,

$$dI = 2 t i (E) dx. \quad (14)$$

Ohm's law gives the potential change, dE , of the solution over a length dx as

$$dE = - \frac{I}{t W C} dx. \quad (15)$$

If $I(x)$ is the current down the crack, and C the conductivity of the solution,

$$\frac{dE}{dx} = - \frac{I}{T W C}, \quad (16)$$

then

$$\frac{d^2 E}{d x^2} = \frac{2 i(E)}{W C}, \quad (17)$$

and

$$\frac{d^2 E}{d x^2} = \frac{dE}{dx} \frac{d}{d E} \left(\frac{d E}{d x} \right). \quad (18)$$

If the potential remains close to the free corrosion potential for passivated crack sides, E_c , the function $i(E)$, describing the electrochemical reactions on the crack sides may be approximated by

$$i(U) = K U, \quad (19)$$

where $U = (E - E_c)$, and

$$K = \left. \frac{d i}{d E} \right|_{E=E_c} = \left. \frac{d i}{d U} \right|_{U=0}. \quad (20)$$

The second order differential Eq. (18), then is applied to Eq. (19),

$$\frac{d^2 U}{d x^2} = \eta^2 U,$$

where

$$\eta = (2 K/w). \quad (21)$$

Integration of Eq. (20) yields

$$\frac{dU}{dx} = (U^2 + b)^{1/2}, \quad (22)$$

where b is a constant to be determined from the boundary conditions,

$$x = \ln \left[\frac{U + (U^2 + b)^{1/2}}{U_0 + (U_0^2 + b)^{1/2}} \right], \quad (23)$$

and

$U = 0$, at $x = L$. Eq. (23) gives

$$U(x) = U_0 \frac{\sinh \eta (L - x)}{\sinh \eta L}. \quad (24)$$

From experimental data (Fig. 18),

$$K = \frac{1}{4.95 \times 10^{-2}} \text{ A m}^2/\text{V}.$$

The crack width (x) is $0.1 \text{ mm} = 0.1 \times 10^{-3}$, the total crack length (L) is 1

$\text{cm} = 1 \times 10^{-2} \text{ m}$ and $\eta = (2K/w)$ is 449.46 , hence

$$\frac{U(x)}{U_0} = \frac{\sinh \eta L (1 - x/L)}{\sinh \eta L} = 0.2587.$$

If we find the $U(x)$ value, U_0 can be calculated.

From Fig. 29, $U(x)$ is about -0.040 V, and U_0 (potential at crack tip) is about -0.155 V. It is impossible to obtain experimentally the potential at the tip of the crack; it can be calculated, however, if polarization curves for the materials are presented, and if it may be assumed that the sides of the crack behave similarly to the outside surfaces.

Melville (58) also developed an analytical method of solution for calculating potential variation potential with stress corrosion cracks where there is a simultaneous variation in current density with potential along the sides of the crack, and a variation in crack width along its length. According to Melville's modified model,

$$dI = 2 t i (E) dx, \quad (25)$$

where $E(x)$ is the specimen potential relative to the electrolyte, and $i(x)$ is the corrosion density. Then

$$dE = \frac{I(x)}{t C w(x)} dx, \quad (26)$$

where $I(x)$ is the current down the crack, and C is the conductivity of the electrolyte. Further

$$\frac{dI}{dx} = 2 t i(E) = t C w(x) \frac{d^2 E}{dx^2} + t C \frac{dw}{dx} \frac{dE}{dx}, \quad (27)$$

$$w = w_0 + bx, \quad (28)$$

$$i(E) = i_0 + a(E - E_0), \text{ and} \quad (29)$$

$$a = \frac{d i}{d E} E_0 \quad (30)$$

From these equations, we have

$$C (w_0 + bx) \frac{d^2 E}{d x^2} + C b \frac{dE}{dX} - 2 [i_0 + a(E - E_0)] = 0, \quad (31)$$

which on substitution for

$$V = E - E_0 + i_0/a, \quad (32)$$

$$y = x + w_0/b, \quad (33)$$

$$a = 8a/Cb, \quad (34)$$

reduces to

$$y^2 \frac{d^2 V}{dy^2} + y \frac{dV}{dy} - \frac{1}{4} a y V = 0. \quad (35)$$

By using the transformed Bessel function, Eq. (35) can be solved.

In general,

$$y^2 \frac{d^2 V}{d y^2} + (2p - 1) y \frac{dV}{d y} - (\alpha^2 y^2 + \beta^2) V = 0. \quad (36)$$

A general solution of this equation is

$$V = y^{-p} \left[C_1 J_{q/r} \left(\frac{a}{r} y^r \right) + C_2 Y_{q/r} \left(\frac{a}{r} y^r \right) \right] \quad (37)$$

with $p = 0$, $r = 1/2$, and $q = 0$. Therefore,

$$V = C_1 J_0 \left(a^{1/2} y^{1/2} \right) + C_2 K_0 \left(a^{1/2} y^{1/2} \right). \quad (38)$$

where $J_0 \left(a^{1/2} y^{1/2} \right)$ and $K_0 \left(a^{1/2} y^{1/2} \right)$ are zero order Bessel functions.

Under free corrosion conditions, the potential at the crack mouth is close to the free corrosion potential E_c , and the boundary conditions used are that

$$E = E_0 = E_c \quad \text{at } x = 1, \text{ and } I = I_t \text{ at } x = 0.$$

In the general case where both $w(x)$ and $i(E)$ vary, putting $i_0 = 0$ and with boundary conditions that $E = E_0 = E_c$ at $x = 1$ and

$$i = -t C w_1 \frac{dE}{dx} = I_t, \quad x = 0, \text{ we have}$$

$$E = E_c - \frac{I_t}{t C w_0} \frac{2y_0}{a^{1/2}} \left[\frac{J_0 \left(a^{1/2} y_1^{1/2} \right) K_0 \left(a^{1/2} y^{1/2} \right)}{J_1 \left(a^{1/2} y_1^{1/2} \right) K_0 \left(a^{1/2} y^{1/2} \right)} - \right]$$

$$\frac{K_0 \left(a^{1/2} y_1^{1/2} \right) I_0 \left(a^{1/2} y^{1/2} \right)}{K_1 \left(a^{1/2} y_0^{1/2} \right) I_0 \left(a^{1/2} y^{1/2} \right)} \quad (39)$$

where $y_0 = w_0/b$ and $y_1 = (1 + w_0/b)$. This may be evaluated at $y = y_0$ to give the potential at the crack tip as,

$$E = E_c - \frac{I_t}{t C w_0} g(\sqrt{\quad}, w_1), \quad (40)$$

where $w_1 = w_1/w_0$, and w_1 and w_0 are the crack widths at the mouth and crack tip respectively; then

$$g(\sqrt{\quad}, w_1) = \frac{2}{\sqrt{\quad}^{1/2} (w_1 - 1)} \cdot \frac{J_0(\sqrt{\quad}^{1/2} w_1^{1/2}) K_0(\sqrt{\quad}^{1/2})}{I_1(\sqrt{\quad}^{1/2}) K_0(\sqrt{\quad}^{1/2} w_1^{1/2})}$$

$$\frac{K_0(\sqrt{\quad}^{1/2} w_1^{1/2}) J_0(\sqrt{\quad}^{1/2})}{K_1(\sqrt{\quad}^{1/2}) J_0(\sqrt{\quad}^{1/2} w_1^{1/2})} = 1, \quad (41)$$

where $\sqrt{\quad} = y_0 = \frac{8 a w_0}{C b^2}$.

Values of the parameter, $\sqrt{\quad}$ can be obtained directly from Eq. (32) using $a = di/dE$ or from a logarithmic plot of current density against potential, from which a becomes

$$a = \frac{di}{dE} = \left[i(E) \ln(10) \frac{d(\log i)}{dE} \right].$$

According to our experiment,

$$C = 0.5 (\Omega \text{ m})^{-1}, \quad w_1 = 0.1 \text{ mm (the crack width at point x)}$$

$w_0 = 0.01$ mm (the width of crack tip)

$$a = \frac{di}{dE} = 10 \text{ A/Vm}^2.$$

Value of $g(\Gamma, w_1)$ which can be obtained from the calculation is

$$g(\Gamma, w_1) = 0.365.$$

The potential difference, that is, $E - E_c = 0$ can also be obtained using

$$\phi = \frac{I_t}{t C w_0} g(\Gamma, w_1). \text{ If } I_t \text{ is about } 320 \times 10^{-2} \text{ A/M}^2, \text{ then}$$

$$\frac{I_t}{t C w_0} = 64 \text{ mV.}$$

Therefore,

$$\phi = E - E_0 = - \frac{I_t}{t C w_0} g(\Gamma, w_1) = - 64 \times 0.365 = - 23.36 \text{ mV}$$

According to the calculation $\phi = 23.36$ mV, an experimental value was founded to be $\phi = 35 - 45$ mV. The real potential drop is larger than that calculated by Eq. (39) but the difference between experimental and calculated values is not large. One also might take account the conductivity variation of electrolyte in the crack by substituting, $Cw = C_0 W + PX$, where the term in PX takes into account the variation of the product

of conductivity. According to these calculations, the effect of the variation in crack width plays a significant role.

5. Summary

This Report is a brief discussion of a research program initially funded in 1984 by the Office of Naval Research. Although definitive answers to the many questions raised by SCC, CF, etc., remain unanswered, the experimental studies described here offer a fresh approach to these questions.

REFERENCES

1. "Stress Corrosion Cracking - A State of the Art, ASTM STP 518," American Society for Testing and Materials, Philadelphia, 1972.
2. M. G. Fontana, "Corrosion Cracking of Metallic Materials," AFML-TR-72-102 Part 1, Air Force Materials Laboratory, Wright-Patterson AFB, OH, 1972.
3. R. P. Wei and G. W. Simmons, "Recent progress in understanding environment assisted fatigue crack growth," Int. J. Fracture 17, 235-247 (1981).
4. J. C. Scully, "Mechanism of dissolution-controlled cracking," Metal Science, June, 290-300 (1978).
5. R. N. Parkins, "An overview - Prevention and control of stress corrosion cracking," Materials Performance 25, 9-20 (1985).
6. L. L. Schreir, "Corrosion," 2nd ed., Butterworths, London, 1976.
7. M. Cohen, "The breakdown and repair of inhibitive films in neutral solution," CORROSION 32, 461-465 (1976).
8. M. Cohen, "Thin oxide film on iron," J. Electrochem. Soc.: Reviews and News 121, 191C-197C (1974).
9. I. L. Rozenfeld, "Corrosion Inhibitors," R. and H. Hardin, transl., McGraw-Hill, New York, 1981.

10. I. L. Rozenfeld, "New data on the mechanism of metals protection with inhibitors," CORROSION-NACE 37, 371-377 (1981).
11. I. L. Rozenfeld and I. K. Marshakov, Corrosion 20, 115t (1964).
12. Yu. N. Mikhailovskii, V. M. Popova, and T. I. Sokolova, "Mechanism of Retardation of Corrosion of Iron by Oxygen-Containing Inhibitors of the Oxidizing Type: Chromates," Z. Metallov. 19, 707-716 (1983).
13. A. Marshall, "An investigation into the mechanism of inhibition of a synergistic dianodic corrosion inhibitor," CORROSION 37, 214-222 (1981).
14. V. M. Ledovskikh, "Synergistic inhibition of corrosion of steel in a neutral medium by mixtures of organic nitrogen compounds with sodium nitrite," Z. Metallov. 19, 84-91 (1983).
15. E. McCafferty, "Corrosion Control by Coatings," H. Leidheiser, Jr., ed., Science Press, Princeton, NJ, 1979.
16. E. McCafferty, "Inhibition of the crevice corrosion of iron in chloride solutions by chromate," J. Electrochem. Soc. 126, 385-390 (1979).
17. B. W. Samuels, K. Sotoudeh, and R. T. Foley, "Inhibition and acceleration of aluminum corrosion," CORROSION 37, 92-97 (1981).
18. D. R. Robitaille, "Sodium molybdate as a corrosion inhibitor in cooling tower water," Materials Performance 15, 40-44 (1976).

19. A. J. Le, B. F. Brown, and R. T. Foley, "The chemical nature of aluminum corrosion: IV. Some anion effects on SCC of AA 7075-T651," Corrosion-NACE 36, 673-679 (1980).
20. R. T. Foley and T. H. Nguyen, "The chemical nature of aluminum corrosion," J. Electrochem. Soc. 129, 464-467 (1982).
21. G. A. Berdzhnisvili, P. V. Strekalov, and Yu. N. Mikhailovskii, "Initial stages of the interaction of aluminum with aqueous solutions containing different oxo anions," Zashch. Met. 21, 37-42 (1985).
22. R. E. Stoltz and R. M. Pelloux, "Inhibition of corrosion fatigue in 7075 aluminum alloys," Corrosion-NACE 29, 13-17 (1973).
23. C. T. Lynch, K. J. Bhansali, and P. A. Parrish, "Inhibition of Crack Propagation of High-Strength Steels Through Single - and Multi-Functional Inhibitors, AFML-TR-76-120, AF Materials Laboratory, Wright-Patterson AFB, Ohio, 1976.
24. M. Khobaib, "Material Evaluation: Part II - Development of Corrosion Inhibitors," AFML-TR-79-4127, Part II, AF Materials Laboratory, Wright-Patterson AFB, Ohio, 1979.
25. M. Khobaib, L. Quackenbush, and C. T. Lynch, "Effect of surfactants upon corrosion inhibition of high-strength steels and aluminum alloys," NACE 39, 253-257 (1983).
26. C. T. Lynch, F. W. Vahldiek, K. J. Bhansali, and R. Summitt, "Inhibition of environmentally enhanced crack growth rates in high

strength steels," in "Environment - Sensitive Fracture of Engineering Materials," Z. A. Foroulis, ed., Proceedings Fall Meeting TMS - AIME, Chicago, IL 1977.

27. M. Khobaib, "Bilge Inhibitors," AFWAL-TR-81-4186, Materials Laboratory, Wright-Patterson AFB, Ohio, 1982.
28. P. A. Parriah, C. M. Chen, and E. D. Verink, Jr., "Retardation of crack propagation of D6AC high strength low-alloy steel in aqueous media by addition of oxidizing inhibitors," Stress Corrosion-New Approaches ASTM STP 610, 281-219 (1969).
29. E. D. Verink, Jr., and K. B. Das, "Research on Inhibition for Corrosion Fatigue of High Strength Alloys," AFML-TR-78-178, AF Materials Laboratory, Wright-Patterson AFB, Ohio, 1978.
30. J. Green and D. B. Boies, "Corrosion inhibitor composition for aqueous liquids," U. S. Patent No. 2,815,328, 3 December 1957.
31. T. Moeller, "Inorganic Chemistry An Advanced Text Book," John Wiley, New York, 1952.
32. E. Zintl and O. Kohn, "On radical-like alkali salts of a new oxyacid of nitrogen," Ber. Deut. Chem. Gesell. 61, 189-199 (1928).
33. P. W. Schenk, "Handbook of Preparative Inorganic Chemistry," 2nd ed., G. Brauer, ed., Academic Press, New York, 1963, p. 496.

34. L. F. Audricth, "Inorganic Syntheses," Vol 1, H. S. Booth, ed., McGraw-Hill, New York, 1939, p.5.
35. "Procedures for Water and Wastewater Analysis," Hach Company, Loveland, CO, 1984.
36. C. C. Addison, G. A. Gamlen, and R. Thomson, "The ultraviolet absorption spectra of sodium hyponitrite, and sodium alpha-oxyhyponitrite: The analysis of mixtures with sodium nitrite and sodium nitrate," J. Chem. Soc. London 103, 338-345 (1952).
37. R. P. Buck, S. Singhadeja, and L. B. Rogers, "Ultraviolet absorption spectra of some inorganic ions in aqueous solutions," Anal. Chem. 26, 1240-1242 (1954).
38. J. C. MacDonald and L. Haddad, "Ultraviolet spectrophotometric determination of nitrite-nitrate in KOH," Environ. Science Techn. 4, 676-678 (1970).
39. J. A. Smith, M. H. Peterson, and B. F. Brown, "Electrochemical conditions at the tip of an advancing stress corrosion crack in AISI 4340 steel," CORROSION-NACE 26, 539-542 (1970).
40. L. V. Ratych, I. N. Dmytrakh, S. A. Pusyak, and O. V. Kurov, "Conditions at the Tip of a Crack During Tests of Materials in a Corrosion Medium," Zashchita Metallov 20, 85-90 (1984).
41. I. L. Rosenfeld and I. K. Marshakov, "Mechanism of crevice corrosion," CORROSION-NACE 20, 115t-125t (1964).

42. T. H. Nguyen, B. F. Brown, and R. T. Foley, "On the nature of the occluded cell in the stress corrosion cracking of AA-7075-T651--Effect of potential, composition, morphology," CORROSION-NACE 38, 319-326 (1982).
43. K. Frank and M. G. F. Fuortes, "Potentials recorded from the spinal cord with microelectrodes," J. Physiol. 130, 625-654 (1955).
44. F. C. Rector, Jr., N. W. Carter, P. W. Seldin, and A. C. Nunn, "The mechanism of bicarbonate reabsorption in the proximal and distal tubes of the kidney," J. Clinical Investigation 44, 278-290 (1965).
45. F. L. Vieira and G. Malnic, "Hydrogen ion secretion by rat renal cortical tubules as studied by an antimony microelectrode," Am. J. Physiol. 214, 710-718 (1968).
46. N. W. Carter, "The production and testing of double-barreled pH glass microelectrodes for measurement of intratubular pH," J. Biol. and Med. 45, 347-355 (1972).
- 47a. L. R. Pucacco and N. W. Carter, "A glass-membrane pH microelectrode," Analyt. Biochem. 73, 501-512 (1976).
- 47b. N. W. Carter and L. R. Pucacco, "Measurements of pH by glass microelectrodes," in "Methods in Pharmacology Volume 4B Renal Pharmacology," M. Martinez-Maldonado, ed., Plenum Press, New York (1976-1978).

48. R. C. Thomas, "Ion-sensitive Intracellular Microelectrodes How To Make and Use Them," Academic Press, New York, 1978.
49. J. van der Spiegel, I. Lauks, P. Chan, and D. Babic, "The extended gate chemically sensitive field effect transistor as multi-species microprobe," Sensors and Actuators 4, 291-298 (1983).
50. T. Katsube, I. Lauks, and J. N. Zemel, "pH-Sensitive sputtered iridium oxide films," Sensors and Actuators 2, 399-410 (1982).
51. I. Lauks, "Multi-element thin film chemical microsensors," Proceedings SPIE 387, "Technology of Stratified Media," R. F. Potter, ed., 138-149 (1983).
52. S. L. Yankell, C. Ram, and I. R. Lauks, "Invitro testing of a new system for monitoring pH at multiple sites," Caries res. 17, 439-443 (1983).
53. J. O. M. Bockris and A. K. N. Reddy, "Modern Electrochemistry," Vol. 2, Plenum Press, New York, 1970.
54. J. Newman, "Electrochemical Systems," Prentice-Hall, Englewood Cliffs, NJ, 1973.
55. J. Newman, "Transport processes in electrolytic solutions," in "Advances in Electrochemistry and Electrochemical Engineering," Vol. 5, C. W. Tobias, Ed., Interscience, New York, 1967.

56. G. P. Cherapanov, L. V. Ershov, and G. G. Kuzmin, "On the growth of corrosion cracks," CORROSION-NACE 29, 100-104 (1973).
57. P. H. Melville, "Variation of potential in stress corrosion cracks," Br. Corros. J. 14, 15-19 (1979).
58. P. H. Melville, "Effect of variation of crack width on the distribution of potential in a stress corrosion crack," Br. Corros. J. 15, 26-30 (1980).
59. P. Doig and P. E. J. Flewitt, "The significance of external polarization on stress corrosion crack growth by anodic dissolution," CORROSION-NACE 37, 378-383 (1981).
60. P. Doig and P. E. J. Flewitt, "The electrode potential within a growing stress corrosion crack," Proc. R. Soc. Lond. A 357, 439-452 (1977).
61. P. Doig and P. E. J. Flewitt, "Limitation of potentiostatic control in stress corrosion crack measurements," Met. Trans. 9A, 357-362 (1978).
62. J. Newman, D. N. Hanson, and K. Vetter, "Potential distribution in a corroding pit," Electrochem. Acta 22, 829-831 (1977).
63. T. R. Beck and E. A. Grens, II, "An electrochemical mass transport-kinetic model for stress corrosion cracking in titanium," J. Electrochem. Soc. 116, 177-184 (1969).
64. R. N. Parkins, "Stress corrosion spectrum," Br. Corros. J. 7, 15-28 (1972).

65. R. N. Parkins, Metall. Rev. 9, 201 (1964).
66. H. W. Pickering and R. P. Frankenthal, "On the Mechanism of localized corrosion of iron stainless steel," J. Electrochem. Soc. 119, 1297-1303 (1972).
67. G. W. Simons, P. S. Rao, and R. P. Wei, "Fracture Mechanics and Surface Chemistry studies of subcritical crack growth in AISI 4340 steel," Met. Trans. 9A, 1147-1158 (1978).
68. J. W. Oldfield and W. H. Sutton, "Crevice corrosion of stainless steels I. A. Mathematical model," Brit. Corros. J. 13, 13-22 (1978).
69. M. J. Pryor, in "Localized Corrosion," R. W. Staehle et. al., Eds., P2, NACE, Houston, Tx (1974).
70. R. Alkire and D. Siitari, "The location of cathodic reaction during localized corrosion," J. Electrochem. Soc. 126, 15-22 (1979).
71. R. Alkire and D. Siitari, "Initiation of crevice corrosion II. Mathematical model for aluminum in sodium chloride solutions," J. Electrochem. Soc. 129, 488-496 (1982).
72. D. W. Siitari and R. C. Alkire, J. Electrochem. Soc. 129, 481 (1982).
73. K. Hebert and R. Alkire, "Dissolved metal species mechanism for initiation of crevice corrosion of aluminum," J. Electrochem. Soc. 130, 1007-1014 (1983).

74. K. R. Hebert and R. D. Alkire, J. Electrochem. Soc. 130, 1001 (1983).
75. A. Turnbull, "Theoretical evaluation of the dissolved oxygen concentration in a crevice or crack tip and in aqueous solution," Corros. J. 15, 162-171 (1980).
76. A. Turnbull and J. G. N. Thomas, "A model of crack electrochemistry for steels in the active state based on mass transport by diffusion and conigration." J. Electrochem. Soc. 129, 1412-1422 (1982).
77. M. Pourbaix, "Atlas of Electrochemical Equilibria in Aqueous Solutions," NACE, Houston, 1966.
79. E. McCafferty, J. Electrochem. Soc. 121, 1007 (1974).
80. W. D. France and N. D. Greene, Corrosion 24, 247 (1968).
81. D. A. Vermilyea and C. S. Tedmon, J. Electrochem. Soc. 117, 437 (1970).
82. G. S. Havilland, Mechanical Engineering, Oct. 17, (1983).
83. S. R. Novak and S. T. Rolfe, J. Material. 4,701, (1969).
84. D. J. Duquette, "Environmental effects I: General fatigue resistance and crack numleation in metals and alloys," in "Fatigue and Microstructure," M. Meshi, ed., American Society for Metals, Metals Park OH, 1979.

85. H. L. Marcus, "Environmental effects II: Fatigue-crack growth metals and alloys," ibid.
86. D. A. Verbitsky and R. B. Diegle, "Concerning strain-enhanced corrosion mechanisms of SCC," Corrosion-NACE 32, 26-29 (1976).
87. W. N. Sharpe, Jr., "The interferometric strain gage", Exp. Mech. 8, 164 (1968).
88. W. N. Sharpe, Jr., "The interferometric surface strain measurement," Int. J. Nondestruct. Test. 3, 59-76 (1971).
89. R. T. Foley and T. H. Nguyen, J. Electrochem. Soc. 120, 2563 (1980).
90. J. A. Davis, in "Localized Corrosion," R. W. Staehle et al., Ed., P168, NACE, Houston, TX (1974).
91. D. Davies, J. P. Dennison, and M. L. Mehta, Corrosion 27, 371 (1971).
92. D. J. Lees, F. P. Ford, and T. P. Hoar, "Some guidelines to the development of stress-corrosion-resistant alloys," Metals and Materials 7, 231-233 (1973).
93. E. N. Pugh, Trans. Am. Soc. Metals. 62, 238 (1967).
94. W. K. Boyd, Proc. Conf. "Fundamental Aspects of Stress Corrosion Cracking," NACE Houston (1969).
95. E. N. Pugh, Metallurgica 63, 3 (1961).

96. I. L. Rozenfeld, in "Localized Corrosion," R. W. Staehle et. al., Eds., P373, NACE, Houston, TX (1974).
97. H. K. Chang, "Corrosion and Corrosion Control," 2nd Ed., Journal, (1971).
98. F. D. Bogar and R. T. Foley, J. Electrochem. Soc. 119, 462 (1983).
99. H. W. Pickering and b. G. Ateya, J. Electrochem. Soc. 122, 1018 (1974).
100. J. Newman and W. Tieman, in "Advances in Electrochemistry and Electrochemical Engineering," Vol. II, H. Gerischer and C. W. Tobias, eds., Wiley Interscience, New York (1978).
101. J. Newman, in "Localized Corrosion," R. Staehle, ed., NACE, Houston, TX (1974).
102. J. R. Galvele, J. Electrochem. Soc. 123, 464 (1976).

END
FILMED

5-86

DTIC